FINAL REPORT

RECEIVED
APR 22 1994
OSTI

FRACTURE BEHAVIOR OF W BASED MATERIALS

Project # 9-X68-9104V
Los Alamos National Laboratory
Los Alamos, NM

Prepared by:

John E. Hack
Department of Mechanical Engineering
Yale University
P.O. Box 2157 Yale Station
New Haven, CT 06520

September 30, 1991

MASTER

DISTRIBUTION OF THIS DOCUMENT IS UNLIMITED

FRACTURE BEHAVIOR OF W BASED MATERIALS

Introduction

This report describes the results of a program to investigate the fracture properties of tungsten based materials. In particular, the role of crack velocity on crack instability was determined in a W-Fe-Ni-Co "heavy alloy" and pure polycrystalline tungsten. A considerable effort was expended on the development of an appropriate crack velocity gage for use on these materials. Having succeeded in that, the gage technology was employed to determine the crack velocity response to the applied level of stress intensity factor at the onset of crack instability in pre-cracked specimens. The results were also correlated to the failure mode observed in two material systems of interest. Major results include: 1) Unstable crack velocity measurements on metallic specimens which require high spatial resolution require the use of brittle, insulating substrates, as opposed to the ductile, polymer based substrates employed in low spatial resolution measurements; and 2) Brittle failure modes, such as cleavage, are characterized by relatively slow unstable crack velocities while evidence of high degrees of deformation are associated with failures which proceed at high unstable crack velocities. This latter behavior is consistent with the predictions of the modelling of Hack et al (1) and may have a significant impact on the interpretation of fractographs in general.

Velocity Gage Development

General

Accurate measurement of the position of the tip of a running crack is required when studying the dynamic fracture of materials in order to determine the crack velocity precisely. Existing methods for crack velocity measurement are divided into continuous and discrete techniques. In the former, one monitors a specific property (e.g. electrical resistance) of the specimen continuously during the fracture process. Discrete techniques provide data points at specific times during the fracture process. Examples of discrete techniques include high speed photography and timing wires. Although crack velocity measurements using timing wires have been conducted since the late 1950's, the spatial resolution has been limited to approximately 2500 μm (2). Such gross dimensions, as compared to the microstructural scale, has hindered the correlation of crack velocity data with microscopic failure phenomena. The goal of the current effort was to develop a gage technology that could accurately measure crack velocity in the appropriate range for unstable fracture (100 - 2000 m/s) with a spatial resolution which approaches the scale of gross microstructural features, such as grain size.

The method developed on the current program is of the discrete type but allows for a spatial resolution on the order of 100 - 250 μm. The experimental set-up is comprised of a fracture gage made of an array of twenty wires of equal spacing (Figure 1). Each wire is connected to a separate high speed digital clock circuit operating at either 10 or 20 MHz. The

twenty channel counter was designed and built by V. D. Aaron of Southwest Research Institute. The gage is deposited on a pre-cracked fracture specimen in the vicinity of the crack tip. All channels of the counter are synchronized at zero time and the sequential breaking of each timing circuit as the crack runs turns off the respective clock. The result is a record of crack tip position as a function of time. The highest measurable crack velocity is given by the product of the wire spacing and the clock frequency. Utilizing microelectronics techniques for the production of the gage, wires with an overall increment of 250 μm, as used in this study, allow the measurement of crack velocities up to 5000 m/s. This is well above the Rayleigh wave velocity in most materials (3) and significantly above the maximum observed velocity in the materials of interest.

Gage Fabrication

The gage fabrication process chosen relies on standard microcircuit photolithographic techniques. As such, a reusable mask, consisting of a glass plate imprinted with the gage pattern was produced from an enlarged pattern cut into a rubylith sheet. The samples are metallographically prepared and coated with a thin layer of an insulating barrier (for conductive specimens). The insulating barrier proved to be the most difficult part of the process and its development will be described in detail later in a subsequent section. Once an insulating surface has been obtained, Cu or Cr is evaporated onto the surface (≈ 1200 Å thick), and a thin layer of positive photoresist is spun onto the metallic layer and soft-baked at 90° C. The mask is then pressed onto the specimen and both are exposed to UV light. After development of the photoresist pattern, the metallic film is etched in the appropriate solution and the remaining photoresist is stripped from the gage. Bondable strain gage terminals are then glued to the edges of the specimens. One side of the terminal is soldered to lead wires from the digital counter while the connection to the gage is made by a combination of conductive tape and paint. A typical sample is shown in Figure 2.

Insulating Barrier

An insulating barrier is necessary on electrically conductive specimens to isolate the gage from the substrate. In addition to its high resistance, however, several other properties of the barrier are critical. The layer must be chemically inert with respect to all of the chemical exposures which occur during the gage fabrication process. These include contact with acetone, butyl acetate, sodium hydroxide, the acid etching solution for the metallic film and water. The layer must also be deposited at a temperature which does not alter the microstructure of the material being studied (< 200° C in this study). Finally, the mechanical properties and adhesion characteristics of the film must be such that the crack in the gage faithfully follows the crack in the specimen. On the basis of earlier work (4) and the aforementioned considerations, initial studies concentrated on compliant polymeric materials. The advantages to the polymer based materials is that they can be spun onto the insulating barrier and produce a pinhole free layer with a typical thickness of 5 μm. Dupont's Kapton polyimide as well as negative and positive photoresists were tested. The resists were exposed to either a light or heavy dose of UV light

to vary the extent of cross linking. Thus, mechanical behavior of the resist could be somewhat controlled to yield ductile or brittle behavior.

In addition, an extremely brittle, ceramic insulating barrier was devised. A layer of Si_3N_4 was deposited at room temperature by Jet Vapor Deposition (5). This technique is based on acceleration of gaseous reaction products in a hyper-velocity jet stream of an inert carrier gas. Adhesion to the substrate results from the high kinetic energy possessed by the accelerated molecules. Films of 1 - 3 μm thickness were deposited on fracture specimens by the JVD process. Processing parameters for all of the test films are given in Table 1.

Specimens and Materials

The aim of the crack velocity measurements was to develop a technique that can be applied to any material which exhibits unstable crack growth. The particular materials tested in this phase of the study included: borosilicate glass; pure, polycrystalline tungsten; and X21-C, a tungsten based "heavy alloy". The heavy alloy consists of 93 w/o tungsten (in the form of 40 μm diameter spheres) dispersed in a nickel - iron matrix containing 0.1 w/o cobalt. The tungsten was in the form of 7 mm plate that had been cross-rolled approximately 50%. The microstructure consisted of pancake grains with diameter and maximum thickness of approximately 100 μm and 40 μm, respectively. Fracture specimens were cut from these materials in the form of plane strain compact tension specimens (Ref. (6) and Table 2). More detail on specimen geometry will be given in the section of this report concerning fracture behavior.

Results

The results reported in this section are meant to convey only the success or failure of a given substrate. Details of the fracture response of the given materials will be given in the following section. Figure 3 shows the data of position vs. time for a sample of pure tungsten measured using the polyimide insulating layer. The results show a high degree of scatter. Examination of the sample in the Scanning Electron Microscope (SEM) showed evidence of local stretching of the layer in the vicinity of the fracture surface (Figure 4). Similar scatter and stretching on the scale of the wire timing wire increment was observed in all samples tested with the various polymeric insulating barriers. As a test of the ability of the polymeric materials to provide faithful correlation with the crack tip position in the sample, specimens of insulating borosilicate glass were tested with and without a polyimide layer. Figures 5 a) and b) show the recorded crack tip position as a function of time for the two specimens, respectively. Measurements on the specimen with the polyimide layer demonstrate the typical large degree of scatter. The results on the bare glass sample, on the other hand, exhibit a straight line with a correlation coefficient of 0.99 and allow for the positive determination of an average velocity. The calculated velocity of 477 m/s agrees well with independent observations (6). These results implied that the polymeric insulating materials often used on samples where the crack gage resolution was limited to several millimeters were not suitable for the spatial resolution required in the current work. Results on specimens of the heavy alloy and pure tungsten using the brittle

Si_3N_4 coating are presented in Figures 6 a) and b), respectively. As can be seen from the data, the degree of scatter is more typical of the bare glass sample and allows for the straightforward determination of an average crack velocity. In addition, SEM examination of the fracture along the surface crack line indicates that the ceramic coating fractured faithfully along the path of the crack in the sample (Figure 7). Although we have no direct means to calibrate the crack velocity independently, the quality of the curves obtained and the tracking of observed velocities with applied stress intensity factor obtained on several materials, as reported in the next section, give confidence in the accuracy of the measurements and the gage technology.

Correlation of Stress Intensity, Crack Velocity and Fractography

General

The classic experiments on brittle fracture performed from the late 1950's through the early 1970's showed that crack tip plasticity is only expected to play a role at low crack velocities where crack tip emission of dislocations can provide dissipation of the energy available to drive the crack (7 - 10). Thus, it has been firmly established in the minds of material scientists that plastic deformation in the region surrounding a crack tip is unimportant in the regime of velocities corresponding to unstable fracture (100 - 1000 m/s). Under such conditions, cracks that become unstable cannot arrest until their velocity is slowed below that necessary to allow the emission of dislocations from the running crack tip. However, all of those studies were conducted on materials whose deformation behaviors show a strong sensitivity to mobile dislocation density. In addition, the tests were carried out with the materials in a condition of low initial dislocation density. Thus, the elevated stresses at the loaded crack tip would be expected to make the crack tip the primary source for fresh dislocations. In addition, as pointed out by Ashby and Embury (11), if the dislocation spacing of the pre-existing mobile dislocations is larger than the extent of the zone surrounding the crack tip over which the flow stress of the dislocations is exceeded the crack responds as if the material is dislocation free and crack tip emission dominates the behavior. Thus, even if the overall dislocation density is large enough to promote homogeneous deformation under uniform loading conditions, the steep stress gradients near the crack tip can effectively nullify their presence. Conversely, a significant density of dislocations within this "zone of influence" leads to homogeneous deformation in the near crack tip region. This zone of influence will hereafter be referred to as the potential plastic zone.

It has been known for quite some time that plastic deformation ahead of a loaded crack tip in metals reduces the stress at the crack tip and moves the peak stress to a position a small distance ahead of the tip (12). Hack et al (1) recently proposed that a result of that action is to modify the criterion for the onset of crack instability. They argued that the existing crack tip would not accelerate smoothly from zero velocity because the stress at the tip is too low to induce propagation. Instead, a running microcrack would be injected in the region of peak stress at some finite distance ahead of the crack by the failure of a microstructural feature. While this process did not represent a new hypothesis, Hack et al (1) went on to propose that the injected microcrack would impart its velocity to the main crack when link-up occurred. Thus, the crack

The significance of this result is that there is a discrete relationship between the applied stress intensity at the onset of crack instability and the critical crack velocity. Unlike the behavior demonstrated by materials in which mobile dislocations are not accessible by the potential plastic zone, the capacity for continuum scale plastic deformation at the crack tip leads to an increasing crack growth resistance with increasing crack velocity. Such behavior is common in dynamic fracture experiments on structural steels (13) and has been confirmed by Hack et al (1) on independent data in 7075 Al (14). A corollary to this result is that, for materials where dislocation activity remote from the crack tip dominates the behavior, fractures which initiate at low values of stored energy (low CTOD) should be associated with low crack velocities. This is precisely the opposite of the behavior observed in the experiments on materials whose behavior can be characterized as dislocation density limited. The purpose of this portion of the program was to gather data on dynamic fracture behavior on two tungsten based alloys as well as test the predictions of the model of Hack et al (1). Correlations of K_o vs v behavior were made with fractography.

Specimens and Materials

The two tungsten based alloys tested on this phase of the project were the same as those used for the gage development reported above: X-21C heavy alloy and warm rolled pure polycrystalline tungsten. The polycrystalline W material was tested in the as-received condition as well as after a slight recovery anneal in which the samples were heated to 800°C in vacuum and immediately furnace cooled. The extent of the heat treatment should have been enough to cause a measurable upward shift in the ductile-to-brittle transition temperature. Compact tension specimens were cut out of the bar of X-21C in the R-C and R-L orientations and labelled as series R and S, respectively. The R samples were 28.6 mm in diameter x 11.4 mm thick while the S specimens measured 31.8 mm x 30.48 mm x 11.4 mm thick. In both cases the crack plane normal was perpendicular to the bar axis but the cracks propagated at 90° to one another in the two specimens (see Figure 9). In addition three specimens were cut in the same orientation as the S but with the crack plane normal parallel to the bar axis (L-R orientation). This specimen series was labelled P. The samples contained either a sharp fatigue pre-crack, a blunt notch of 0.2 mm radius or a blunt notch of 0.4 mm radius. Compact tension specimens were cut from the pure polycrystalline tungsten plate with the specimen edges parallel to the plate edges. Dimensions of the W specimens was the same as that for the S and P series heavy alloy specimens except the thickness was 7 mm. Specimens of the W plate material which were annealed are identified by the designation T. All samples were metallographically polished on one side and coated with approximately 1 μm of Si_3N_4 by the JVD process described earlier. Crack velocity gages were developed on the ceramic substrate by the process described in the first section of this report. Testing was carried out under displacement control in a servo-hydraulic testing machine at various loading rates. The load at the onset of crack instability and crack position as a function of time were recorded. Only samples for which the crack position as a function of time showed a correlation coefficient in excess of 97 % by a linear regression analysis are included in this summary. The test data for which the confident determination of a crack velocity could not be performed because of scatter are included in the Appendix to this final report for completeness.

would be instantaneously endowed with a finite velocity. This means that the energy balance which applies to the onset of instability must contain a kinetic energy term even in cases of quasi-static loading. The critical question then becomes whether or not the crack is moving at a sufficient velocity to sustain itself with whatever energy was stored in the body at the onset of propagation by the applied stress intensity. A unique relationship between the miminum velocity for instability, v, and the applied stress intensity factor, K_o, was obtained by Hack et al (1) and is given by:

$$v = C_R \left(1 - \frac{K_G}{K_o^2} - \frac{\gamma_p E}{K_o^2 (1 - \nu^2)} \right) \tag{1}$$

where

C_R = Rayleigh Wave Speed
ν = Poisson's Ratio
E = Young's Modulus
γ_p = Plastic Work per Unit Area Crack Advance

and K_g, the Griffith value of the stress intensity factor (that required to overcome the surface energy produced during crack extension, γ_s) is defined by:

$$K_g = \left(\frac{2 \gamma_s E}{K_o^2 (1 - \nu^2)} \right) \tag{2}$$

K_o is equal to K_{Ic} for a sharp crack and generally somewhat higher than that for specimens containing a blunt notch.

Application of the model to dynamic and quasi-static fracture data on 4340 steel and 7075 Al showed that a minimum velocity existed for crack instability, associated with K_{Ic}, while the critical velocity for instability increases from that value with increasing applied stress intensity factor. A schematic of the resultant criterion line is shown in Figure 8. Here, the crack tip opening displacement (CTOD) is plotted as a function of crack velocity. The CTOD is related to the applied stress intensity factor by the following expression:

$$CTOD = \frac{K_o^2}{\overline{\sigma}_y E} (1 - \nu^2) \tag{3}$$

where $\overline{\sigma}_y$ is the tensile yield stress. The figure demonstrates that at $CTOD_{min}$ (where $K = K_{Ic}$) a microcrack must be provided by the material moving at least as fast as velocity v_{min} for the main crack to go unstable after link-up. For samples containing blunt notches as crack starters, loading to $CTOD_c$ increases the required velocity for instability to v_c. A complete description of the reasons for this can be found in Reference (1) but for the purposes of this report, it is sufficient to note that crack velocities below v_c result in the dissipation of too much energy in plastic deformation for the energy balance to be satisfied for cracks loaded to $CTOD_c$ and, thus, results in crack arrest or stable tearing. If the crack is running at a velocity at least as high as v_c, the energy balance for crack propagation can be satisfied and the crack will become unstable.

Results

Table 3 presents the experimental conditions and results for all of the samples tested which yielded valid crack velocities. It was found that loading rate gave better control over resultant crack velocity than did notch root geometry for these materials. Figures 10 and 11 show plots of $K^2/(\bar{\sigma}_y E)$ vs crack velocity for the S series heavy alloy and K^2 vs v for the T series polycrystalline W, respectively. Most of the data for the respective materials was taken on specimens from these conditions. An obvious feature of the figures is a steady increase in crack growth resistance as a function of increasing crack velocity. Figures 12 and 13 present plots of the data in Figure 9 along with data points obtained from R and P series samples, respectively. Although the number of samples is small for the R and P series, the plots indicate little difference in dynamic behavior between S and R samples even though they propagate in different directions on the same plane. Any difference between the P and S series also is not very obvious. Figure 14 compares the response of the T series W specimens to those in the as-received condition. Although the curves have a similar slope, it does appear that the as-received data is shifted to slightly higher K values for any given velocity. When the yield strengths of both conditions are measured and used to normalize the data, this small shift may disappear.

Figures 15 a) and b) are low magnification fractographs of specimens S15 and S6, respectively. S15 fractured with a crack velocity of 131 m/s while S6 fractured with a crack velocity of 672 m/s. At the magnification used in these micrographs there is no apparent difference between the two samples with respect to failure mode. The same fracture surfaces are presented at higher magnification in Figures 15 c) and d). The higher magnification micrographs reveal a consistent, albeit difficult to quantify, distinction between the low and high crack velocities. At the higher velocity observed in specimen S6 (Figure 15 d)), the crack has run with a fairly flat trajectory which does not involve much interfacial failure between the matrix material and the W spheres. This is evidenced by the fact that only one binding neck per W sphere is exposed on the fracture surface. At the lower crack velocity observed in specimen S15 (Figure 15 c)) one can discern multiple binding necks per W sphere exposed on the fracture surface. Although not every sphere shows severe interfacial delamination, a great preponderence of the exposed spheres do. This mode of failure is observed much more infrequently on the higher velocity fractures in the S series samples. In the R series samples, which show a flatter CTOD vs v response, this type of delamination is observed in both samples tested. Fractographic examination of the P series samples has yet to be performed. Although the trend in the S series form interfacial delamination at low velocities to flat fracture at higher velocities is apparent across all of the specimens tested, attempts to be more quantitative have been thwarted by the small scale of the deviations in crack trajectory induced by delamination of the spheres from the matrix. Two-dimensional quantitative metallography does not distinguish the difference and three-dimensional quantitative metallography is not possible at the required magnifications using the technology available at Yale. Independent attempts to quantify the degree of delamination at the ball/matrix interface as a function of crack velocity and orientation will continue after the conclusion of the current program.

Figures 16 a) and b) show low magnification fractography of W samples T16 and T37, respectively. The crack velocity observed for sample T16 was 138 m/s while that for sample T37 was 965 m/s. As was the case with the heavy alloys, not much difference is evident between the

two conditions at this magnification. Once again, however, higher magnification views of the two fracture surfaces (Figures 16 c) and d)) reveals a significant difference between the failure modes in the two cases. As can be seen from the figures, the lower velocity fracture is characterized by almost 100% cleavage of the pancake grains while the higher velocity failure is distinguished by a high degree of surface roughness, indicating a significant amount of deformation was associated with the fracture process. In the case of the pure W material, both failure modes were relatively flat at the magnifications which allowed the resolution of the failure modes so that two-dimensional metallography was suitable for the determination of the percentage of cleavage on the fracture surface as a function of velocity in the T series samples. Such an analysis was performed using point counting on twenty micrographs each taken at random locations on the T series samples. The data are summarized in Figure 17. It is clear from the figure that the percentage cleavage fracture dramatically decreases with increasing velocity in this material. Similar behavior is observed for the as-received specimens (Figure 17).

Discussion

Velocity Gage Development

The results of the velocity gage development pretty much speak for themselves in that a gage technology was successfully developed and applied to the measurement of crack velocities in two alloy systems. One important result of the gage development process was that the use of compliant insulating barriers is not compatible with crack velocity measurements with a spatial resolution at or approaching the scale of most microstructural features of interest. Apparently, when the scale over which stretching and subsequent necking of the polymer approaches that of the measurement increment, the temporal (and, therefore, spatial) registry between the sample and the crack gage is lost. Therefore, brittle coatings, such as the Si_3N_4 used in this study are more appropriate when high spatial resolution is required. It may also be remarked that the JVD process does appear to be a viable way in which to apply a ceramic substrate at least when the deposition process must be performed at or very near to room temperature. One last comment concerns the choice of metal for the gage itself. Cu worked very nicely for the heavy alloy specimens, consistently yielding high quality data for crack position as a function of time. A side benefit of using Cu is that it is clearly visible against the metallic background of the sample and clear substrate. Some variability was noticed on the W specimens, in that there was very a great deal of scatter in some of the experiments. The dramatically lower fracture toughness and higher stiffness in the pure W specimens over those in the heavy alloys leads to a much smaller CTOD as a crack propagates in the tungsten. Therefore, it is believed that a more brittle wire material is also required when testing very brittle samples. The use of Cr as a conductor is currently being explored, but the similarity in color and reflectance between the Cr and the samples leads

to difficulties in the photographic development of the gage. The use of a Cu layer between the sample surface and the ceramic insulating barrier is being explored as a way to alleviate this problem.

Correlation of Stress Intensity, Crack Velocity and Fractography

All of the samples tested showed an increasing resistance to crack propagation with increasing crack velocity. This indicates that crack propagation in both of the materials, in all the orientations or conditions, is dominated by plastic deformation at the crack tip brought on by mobile dislocations which are accessed by the crack as it moves through the material. If the W plate were to be heavily recovered, or recrystallized, so that the initial mobile dislocation density were severly reduced, it may be expected to show behavior more typical of the results on single crystals (7). It should be noted that large unstable crack velocities were generated in the fracture toughness samples without employing high loading rates. Behavior under dynamic loading as well as dynamic propagation may yield different trends. The material which the crack passes through may be substantially altered from its initial condition by the dynamic loading process, particularly if the crack must initiate without the benefit of a pre-crack.

Perhaps the most interesting result of the study is the correlation between unstable crack velocity and failure mode. It is well known that interfacial delamination of W spheres is associated with low ductility behavior in heavy alloys (15,16). Conversely, if the fracture path avoids delamination of the spheres, high ductility is usually observed. Similarly, cleavage is a harbinger of brittle behavior while surface roughness indicates at least some deformation activity accompanied the fracture process. In the S series heavy alloy specimens and the T series W samples, the only two data sets with a sufficient number of specimens and state of analysis, it is clear that the low energy failure mode is associated with low crack velocities. One must recognize that even low unstable crack velocities are much higher than stable crack growth rates. However, the correlation holds over an order of magnitude variation in unstable crack velocity. Thus, it appears from the data that the prediction of Hack et al (1) is reasonable for materials where brittle fracture is not dominated by crack tip processes. This underscores the need for a good deal of caution in the extrapolation of ideas concerning brittle fracture derived from experiments on materials containing a low density of mobile dislocations that can be accessed by a crack to structural materials which have undergone extensive thermo-mechanical processing prior to use. It also raises doubt with regards to the interpretation of fractography on failed components when the failure conditions in service are not clear. There could be significant confusion between the identification of slow, stable cracking and high speed unstable cracking if the nature of the actual failure is not well established. Although it has not been demonstrated, this same type of behavior may also be expected in ceramic materials where microcracking or localized volume changes associated with stress induced phase transformations could take the place of plasticity as the energy dissipation mechanism which dominates the energy balance for crack propagation. This possibility is being explored in TiB_2 material supplied by Los Alamos. Work is also beginning on Ta-10W. In addition, quantification of predictions of the observed CTOD vs v behavior in both of these materials is currently underway using high rate constitutive law behavior supplied by Rusty Gray and Paul Follansbee of Los Alamos.

Summary

Several summary statements can be made based upon the material presented herein. These include:

A high resolution crack velocity gage has been developed which allows for the measurement of crack velocities in the unstable regime over distances approaching gross microstructural features, such as grain size

Unstable crack velocity in materials which have the capacity for crack tip deformation by dislocations from sources other than the crack tip is proportional to the CTOD or the elastic energy stored in the body at the onset of the instability

For such materials, low toughness behavior is characterized by a brittle fracture mechanism and a low crack velocity while increasing the unstable crack velocity acts to increase the plastic work per unit area crack advance and is typified by a more ductile failure mode

The opposite trend would be expected in the unstable fracture of materials whose crack propagation is dominated by the emission of dislocations from the crack tip prompting the need for care in the extrapolation of such data to the behavior of structural materials and caution in the interpretation of fractography when the failure conditions are unknown

Acknowledgements

The author would like to acknowledge the assistance of Dr. Dany Rittel and Mssr's J. G. Kosinski, R. Faust and E. J. Rothstein in the performance of the work described herein. He is also grateful for technical discussions with A. D. Rollett and G. T. Gray of Los Alamos as well as for financial support from Los Alamos under the auspices of A. D. Rollett.

References

1. J. E. Hack, S. P. Chen and D. J. Srolovitz, Acta Metall., 37, 1957 (1989).

2. J. J. Gilman, C. Knudsen and W. P. Walsh, J. Appl. Phys., 29, 601 (1958).

3. M. F. Kanninen and C. H. Popelar, Advanced Fracture Mechanics, Oxford University Press, NY, 199 (1985).

4. G. T. Hahn, R. G. Hoagland, M. F. Kanninen and A. R. Rosenfield, in Dynamic Crack Propagation, G. C. Sih (ed.), Noordhoff, Leyden, 649 (1973).

5. B. A. Chen, D. Wang, T. P. Ma, J. W. Golz, B. L. Halpern and J. J. Schmitt, in the Proceedings of the Eighth Symposium on Plasma Processing, The Electrochemical Society (1990).

6. ASTM Specification E399-83, ASTM Standards, 10, 519 (1983).

7. A. S. Tetelman and W. D. Robertson, Acta Metall., 11, 415 (1963).

8. J. J. Gilman, Trans. Am. Inst. Mining and Met. Engrs., 209, 449 (1957).

9. J. M. Liu and B. W. Shen, Metall. Trans. A, 15A, 1247 (1984).

10. S. J. Burns and W. W. Webb, J. Appl. Phys., 41, 2086 (1970).

11. M. F. Ashby and J. D. Embury, Scripta Metall., 19, 557 (1985).

12. J. R. Rice and M. A. Johnson, in Inelastic Behavior of Solids, Kanninen et al (eds.), McGraw - Hill, NY, 143 (1970).

13. S. J. Hudak, R. J. Dexter, J. H. Fitzgerald and M. F. Kanninen, Engrg. Fract. Mech., 23, 201 (1986).

14. C. Lin and R. G. Hoagland, in Fracture Mechanics: Sixteenth Symposium, ASTM STP 868, ASTM, Philadelphia, 467 (1985).

15. J. Lankford, C. E. Anderson, Jr. and S. R. Bodner, J. Mater. Sci. Letters, 7, 1355 (1988).

16. K. S. Churn and R. M. German, Metall. Trans. A, 15A, 331 (1984).

TABLE I - INSULATING LAYERS AND PROCESSING PARAMETERS STUDIED

Insulating Layer	Type	Deposition	Curing Conditions	UV Radiation
Kapton Polyimide	Compliant	Spin-on	150°C $t \geq 1$ hr	none
Positive Photoresist	Compliant	Spin-on	150°C $t \geq 3$ hr	$t \geq 3$ hr
Negative Photoresist	Compliant	Spin-on	150°C $t \geq 3$ hr	$t \geq 3$ hr
Silicon Nitride	Brittle	Jet Vapor Deposition	none	none

TABLE II - MATERIALS AND THICKNESS OF SAMPLES TESTED

Material	As-Received Form	Thickness
Glass	Plate	6.35 mm
Pure Tungsten	Cross-rolled Plate	7 mm
X-21C Heavy Alloy	Swaged Bar (15%)	28.6 mm (dia)

TABLE III A - DATA FOR ALL PURE TUNGSTEN SPECIMENS TESTED

Sample	Coating	Notch dia (mm)	Stroke Rate (mm/min)	K_o ($MPam^{1/2}$)	Velocity (m/s)	R (%)
7	Si_3N_4	0.76	---	13.3	344	97.4
10	Si_3N_4	0.76	0.225	23.5	679	96.5
25	Si_3N_4	0.76	1.5	10.9	229	96.7
27	Si_3N_4	0.41	0.375	12.0	170	90.4
28	Si_3N_4	0.41	0.375	18.9	312	88.5
29	Si_3N_4	0.41	0.45	18.2	375	97.8
30	Si_3N_4	0.41	0.3	---	---	---
T14	Neg. PR	?	?	?	---	---
T15	Si_3N_4	0.76	0.3	14.8	251	83.0
T16	Si_3N_4	0.76	?	10.5	138	98.5
T17	?	?	?	---	---	---
T18	Polyimide	?	?	---	---	---
T19	?	?	?	---	---	---
T32	Si_3N_4	0.76	0.26	15.0	328	98.3
T35	Si_3N_4	0.41	0.26	18.3	330	98.5
T36	Si_3N_4	0.41	0.24	33.5	517	96.0
T37	Si_3N_4	0.41	0.23	27.5	965	97.0
T38	Si_3N_4	0.41	0.3	10.57	71	97.7
T40	?	?	?	25.7	---	---
L1	?	Sawed	?	---	---	---
L3	Neg. PR	Sawed	?	---	---	---
L5	Si_3N_4	Sawed	0.3	31.2	560	---

TABLE III B - DATA FOR ALL HEAVY ALLOY SPECIMENS TESTED

Sample	Coating	Notch dia (mm)	Stroke Rate (mm/min)	K_o ($MPam^{1/2}$)	Velocity (m/s)	R (%)
R1	Si_3N_4	pre-crack	?	52.7	134	98.2
R2	Si_3N_4	?	3	171.3	975	99.4
R3	Si_3N_4	?	?	?	573	96.0
R4	Si_3N_4	0.41	?	95.8	675	98.4
R5	Si_3N_4	pre-crack	?	?	stable	---
S6	Si_3N_4	0.76	3	140.6	672	97.6
S7	Si_3N_4	0.76	2.25	109.3	555	98
S8	Si_3N_4	0.76	?	67.4	318	99
S9	Si_3N_4	0.41	3	95.9	522	99.1
S10	Si_3N_4	0.41	?	78.7	247	4 pts
S11	Si_3N_4	0.41	3	121.8	556	94.6
S12	Si_3N_4	pre-crack	3	80.1	174	7 pts
S13	Si_3N_4	0.41	3.45	63.8	256	97.9
S14	Si_3N_4	0.41	?	79.9	338	99.4
S15	Si_3N_4	pre-crack	3.23	35.1	131	97.2
P16	Si_3N_4	0.41	3.75	130.3	514	99.2
P17	Si_3N_4	0.41	3	93.5	492	98.0
P18	Si_3N_4	0.76	3	91.8	429	98.8

TABLE III C - DATA FOR ALL GLASS SPECIMENS TESTED

Sample	Coating	Notch dia (mm)	Stroke Rate (mm/min)	K_o ($MPam^{1/2}$)	Velocity (m/s)	R (%)
pglas	none	---	---	---	479	98.9
glas/po	polyimide	---	---	---	---	no corr
gl1	none	---	---	---	771	98.6
gl2	none	---	---	1.55	743	98.7

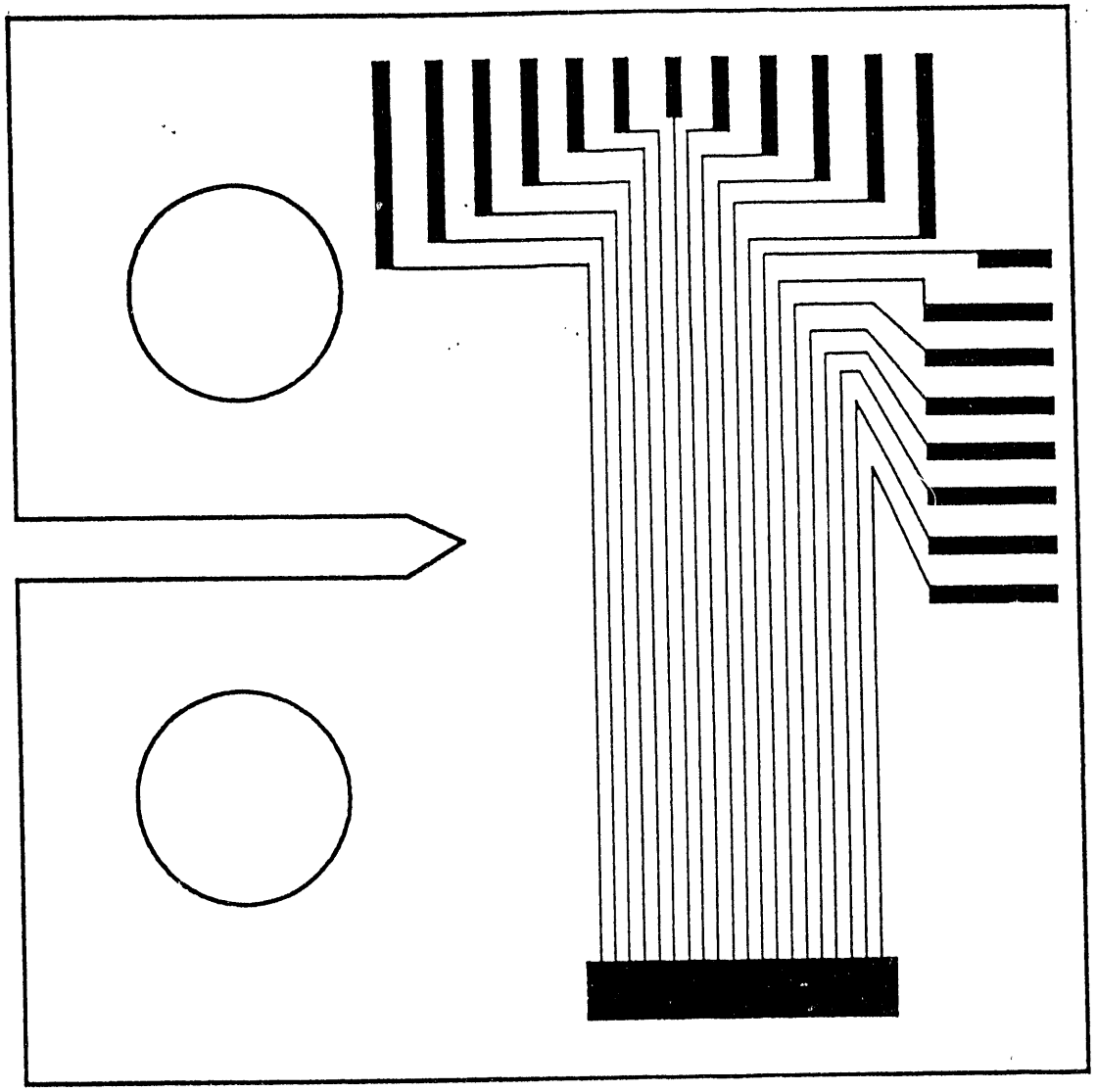

Figure 1 - Schematic of crack velocity sample and gage layout

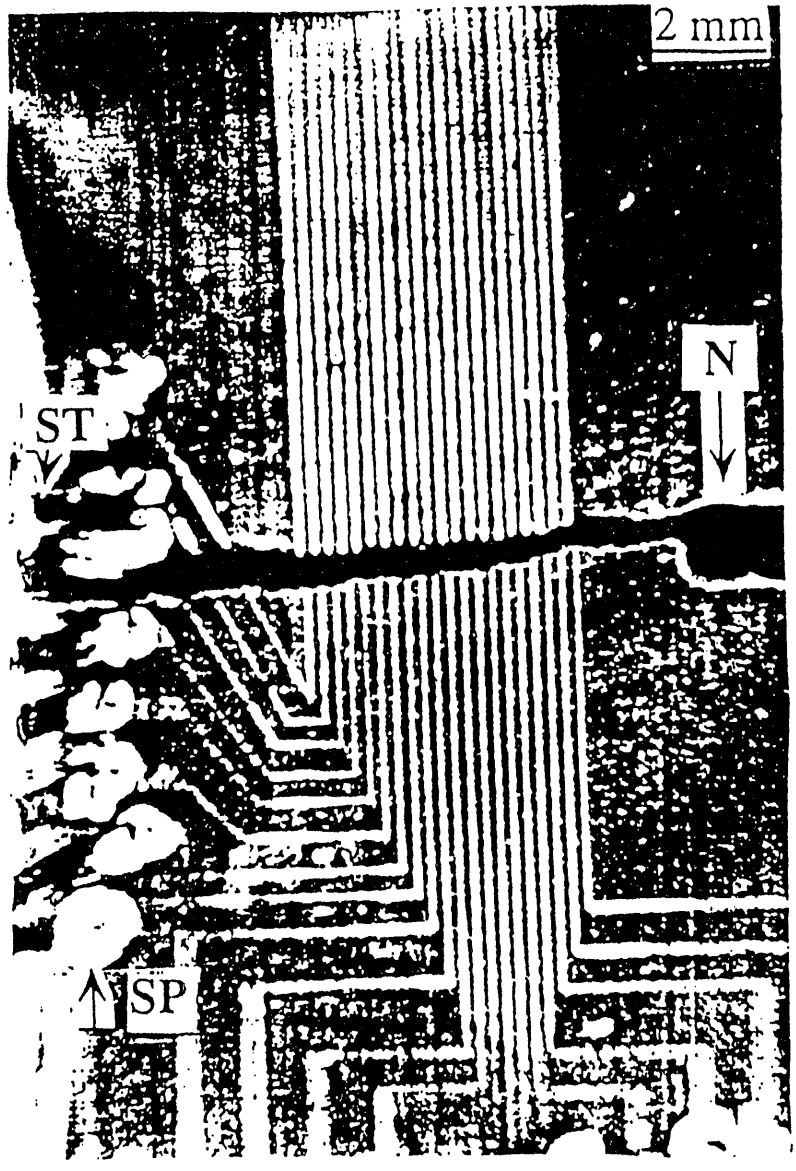

Figure 2 - Detail of gage and painted connections (SP); N indicates starter notch

Figure 3 - Crack position vs. time for a pure W specimen (T18) with a polyimide insulation layer

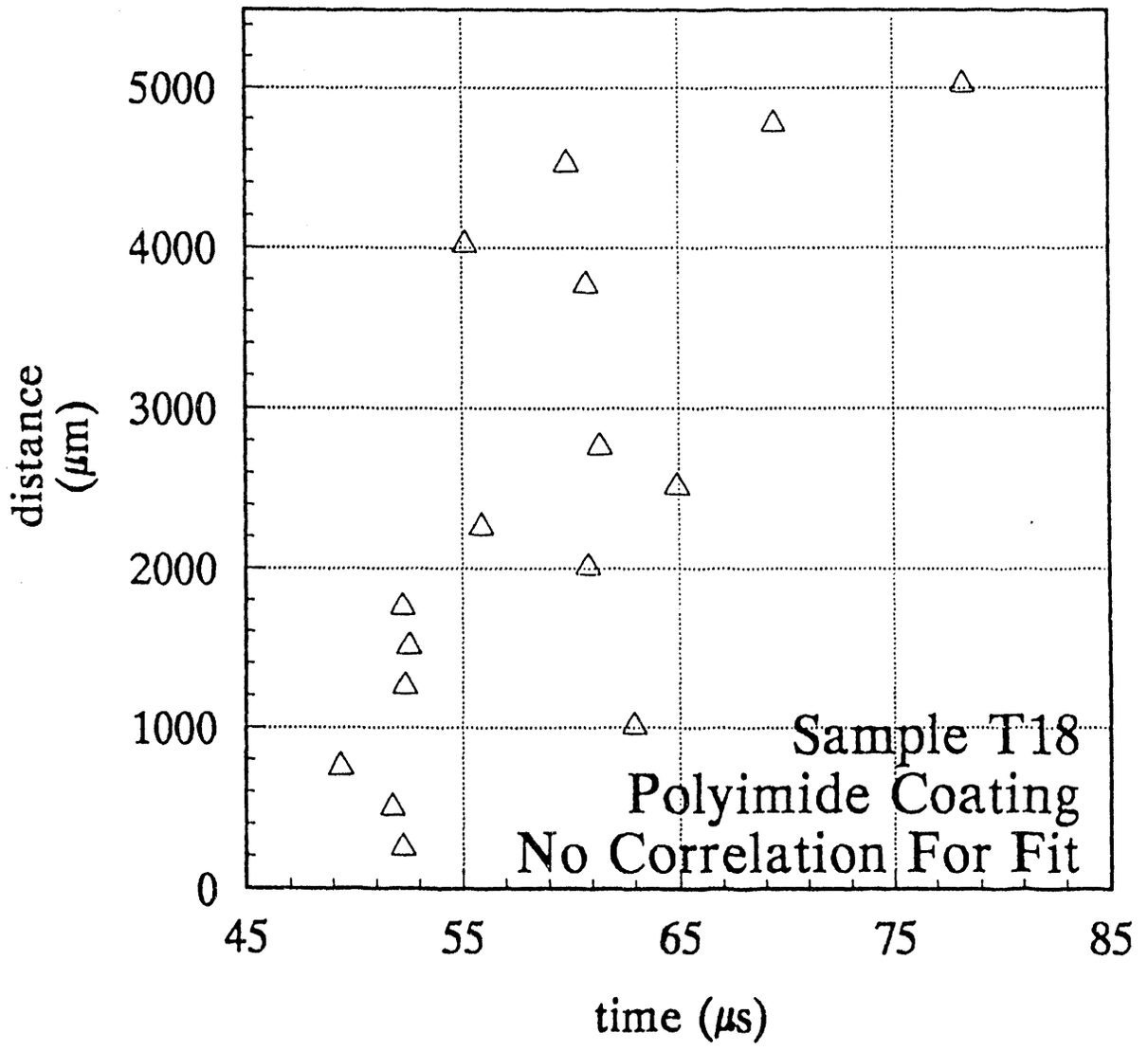

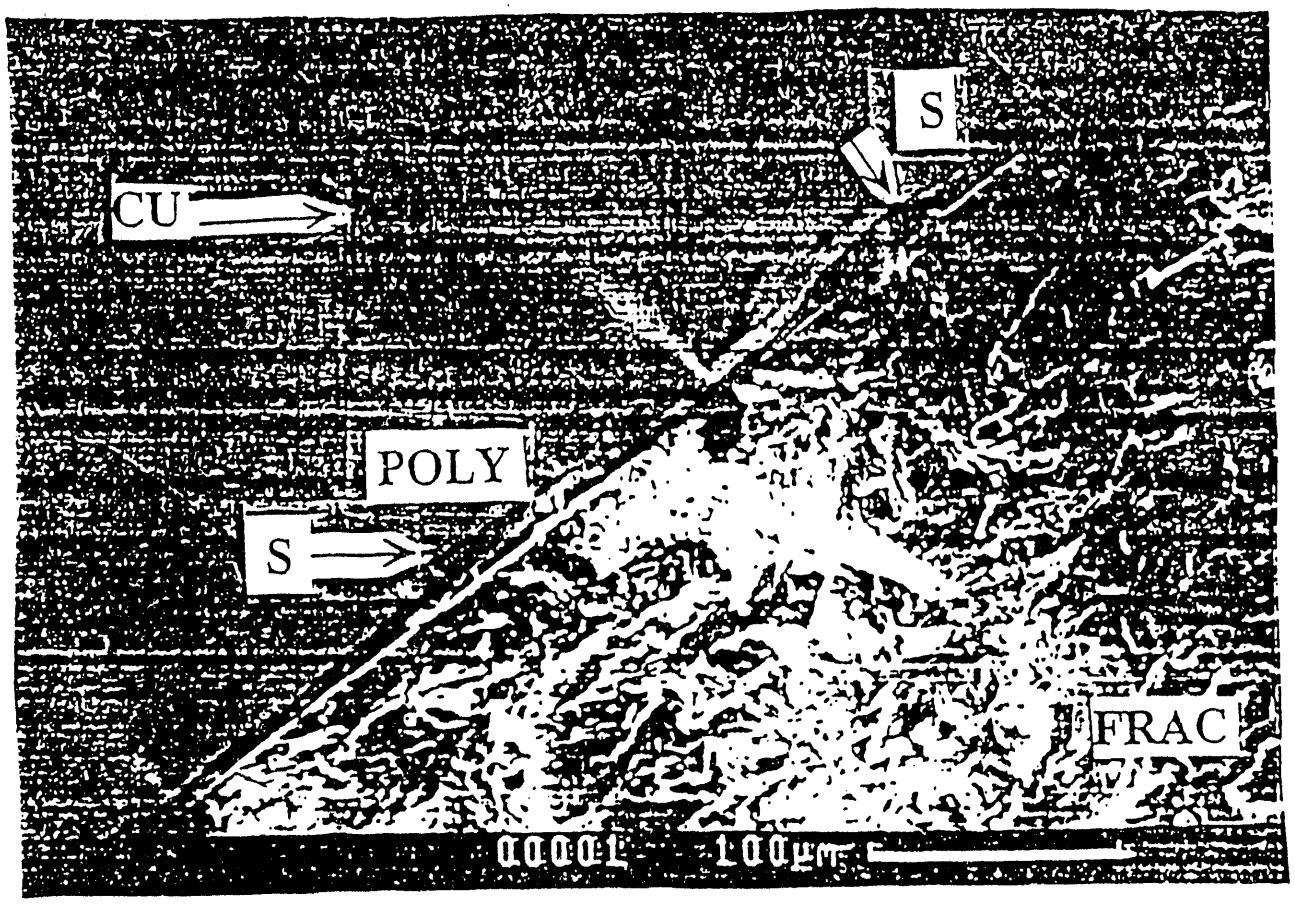

Figure 4 - Detail of crack edge in Sample T18 showing stretching of the polyimide layer (S)

Figure 5a - Crack position vs time for a borosilicate glass specimen (glas/po) with a polyimide insulation layer

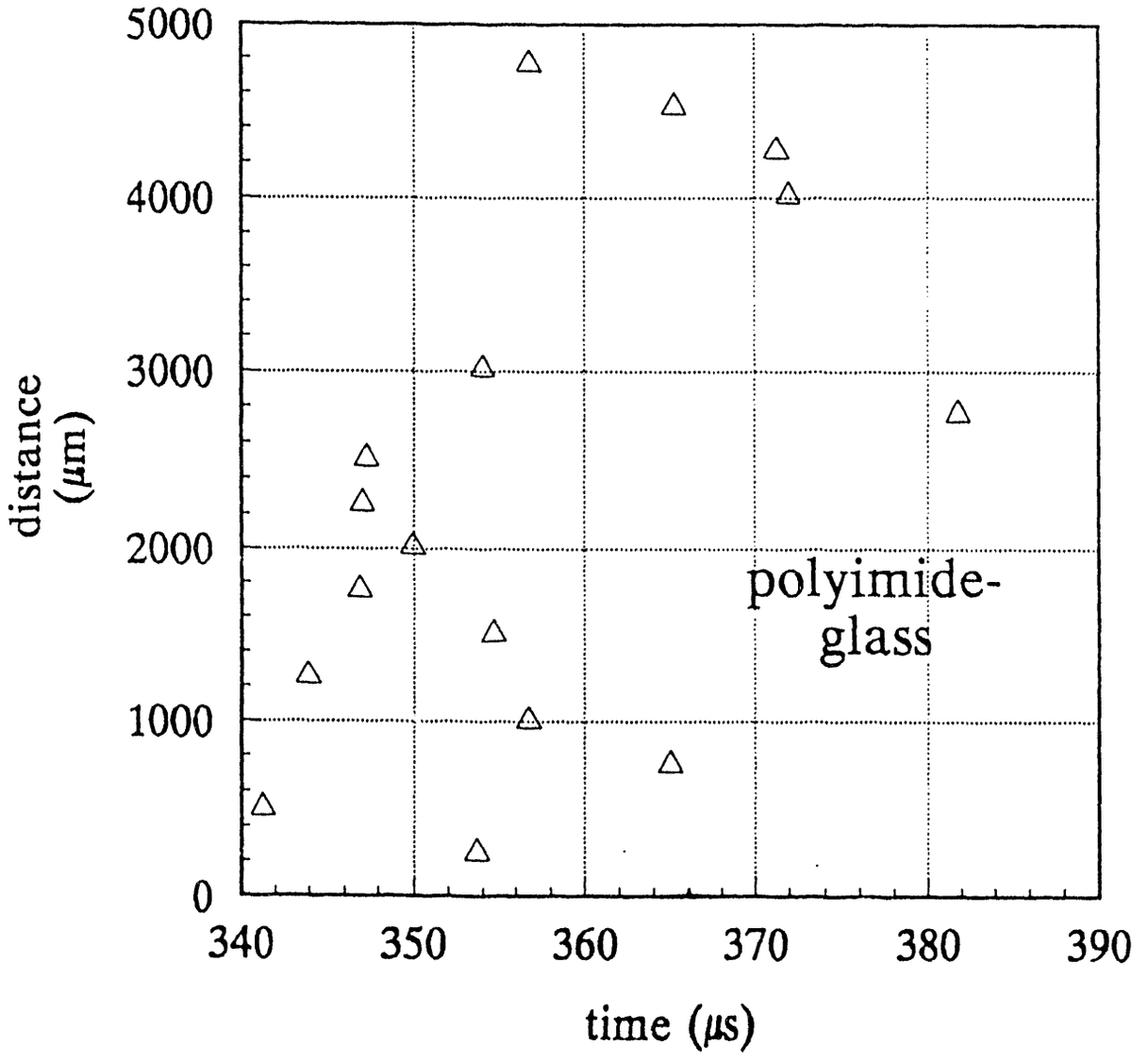

Figure 5b - Crack position vs time for a bare borosilicate glass specimen (pglas)

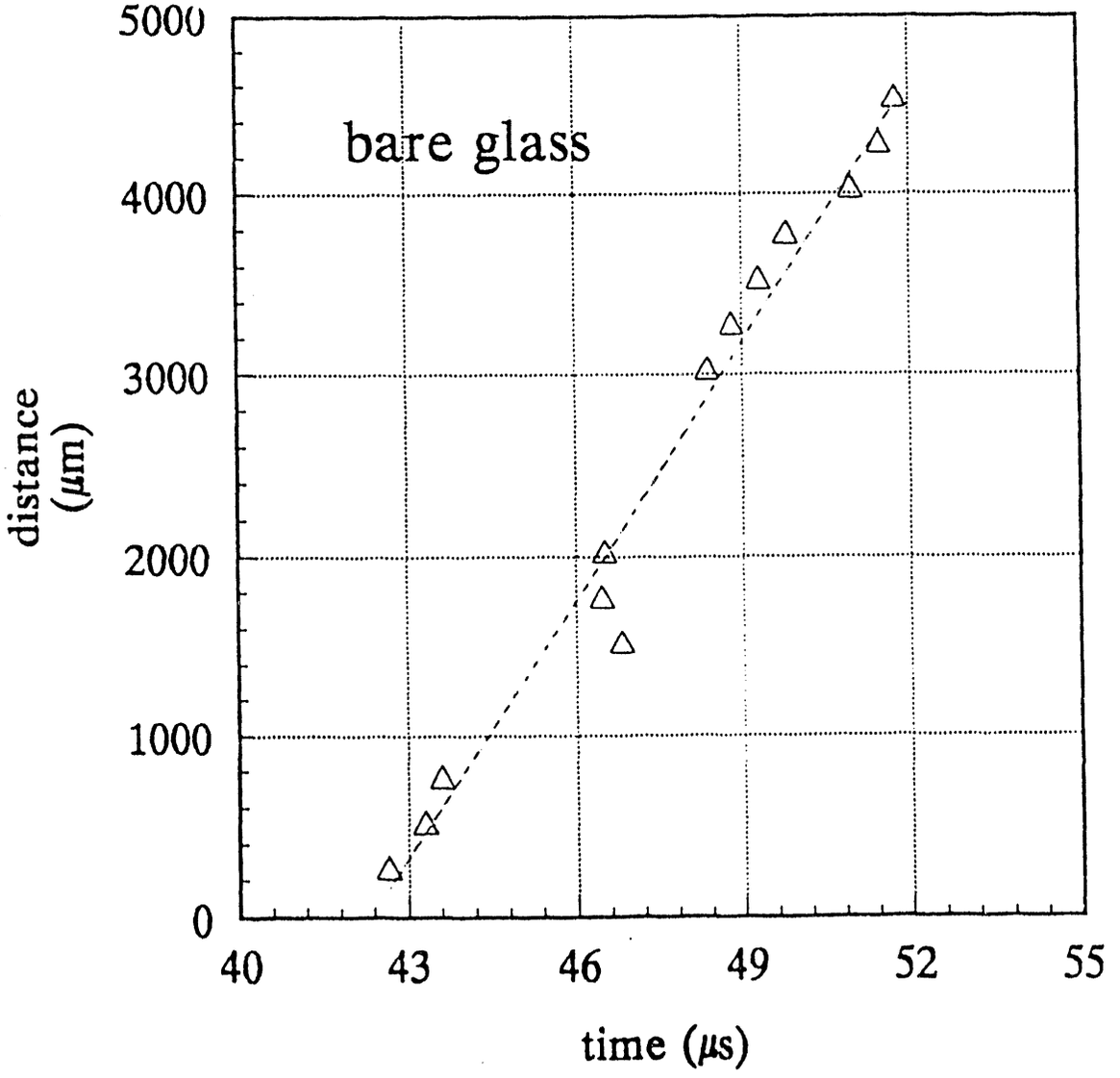

Figure 6a - Crack position vs time for a heavy alloy specimen (S13) with a Si_3N_4 insulation layer

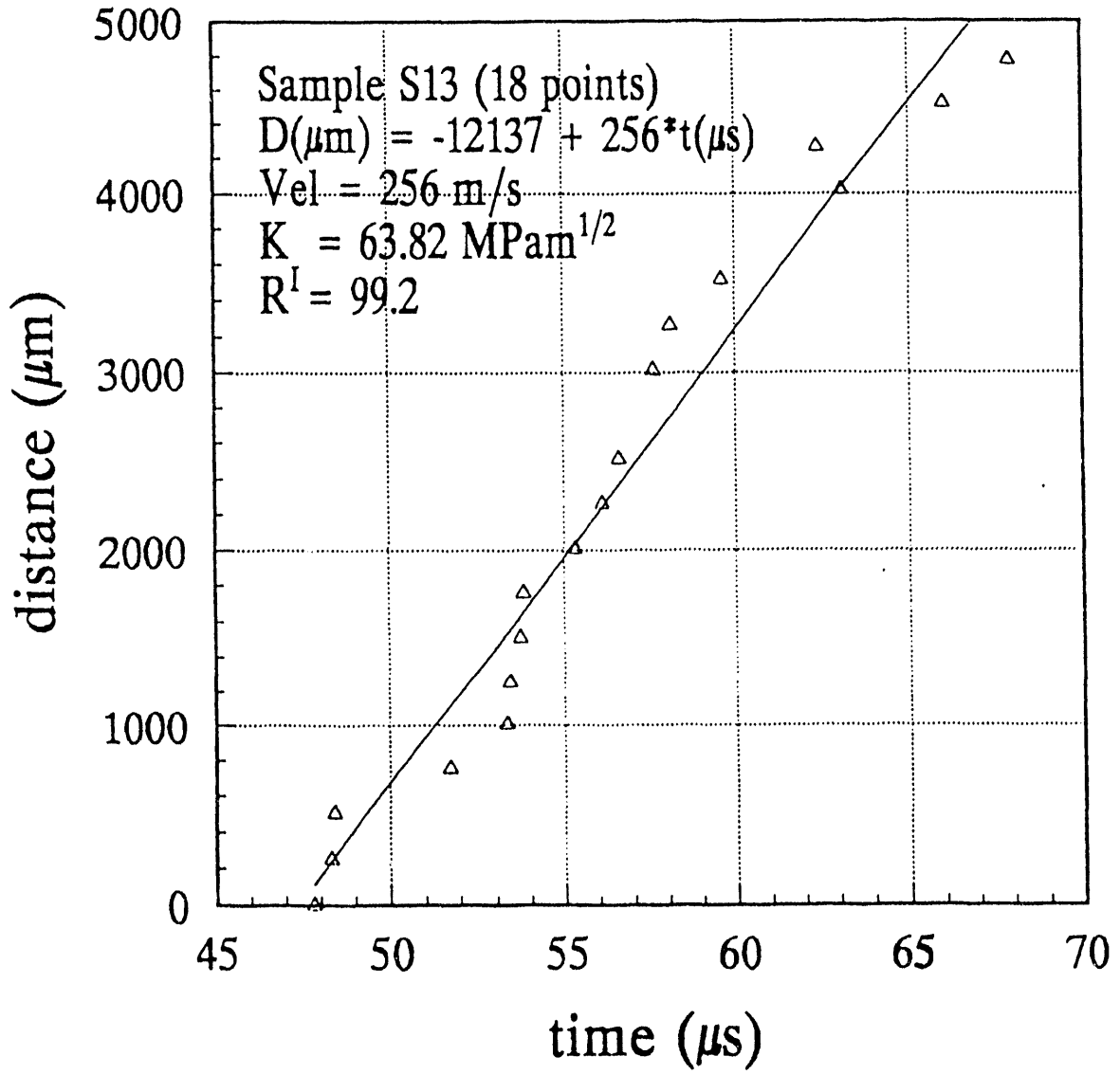

Figure 6b - Crack position vs time for a pure W specimen (T16) with a Si_3N_4 insulation layer

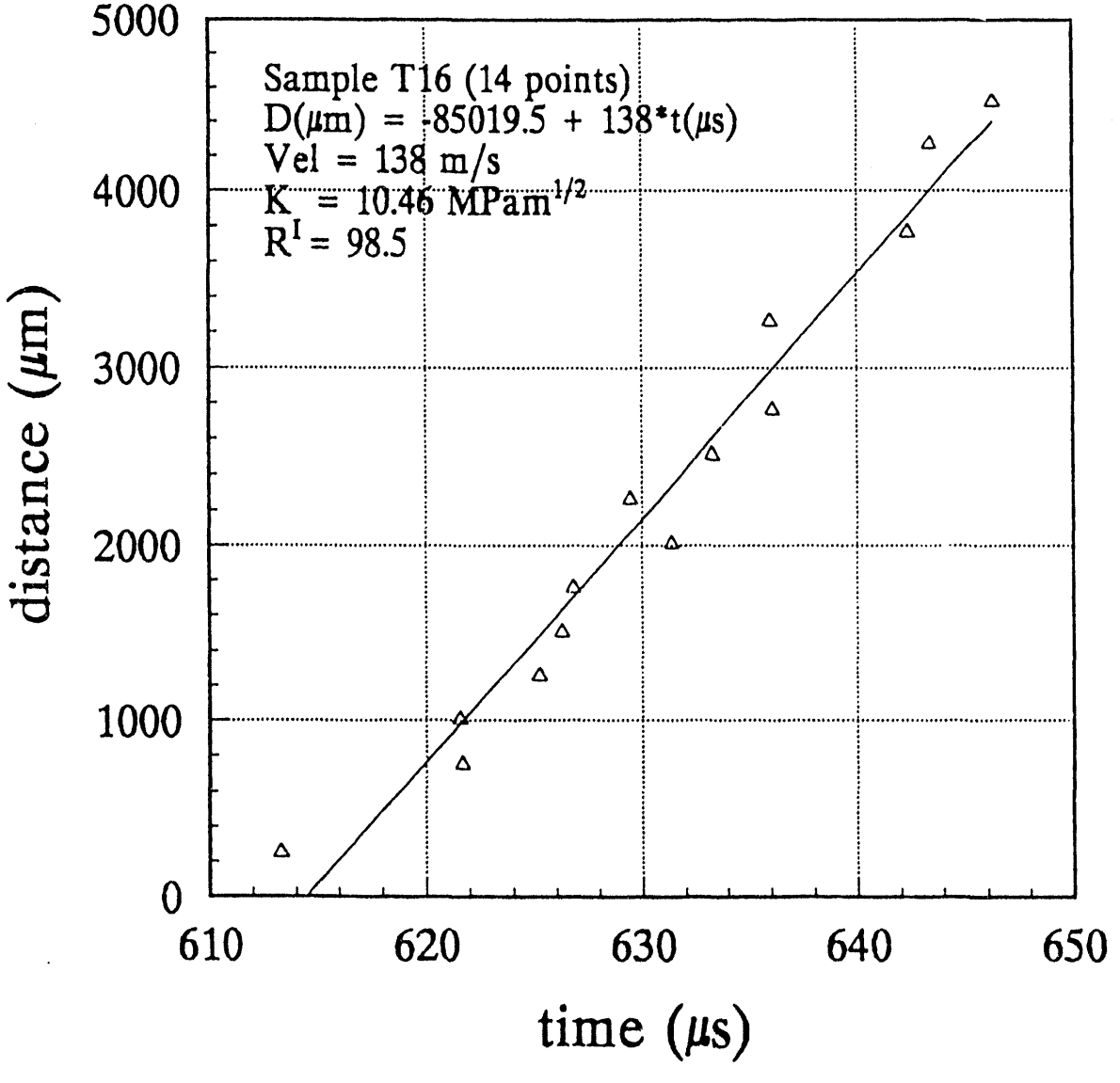

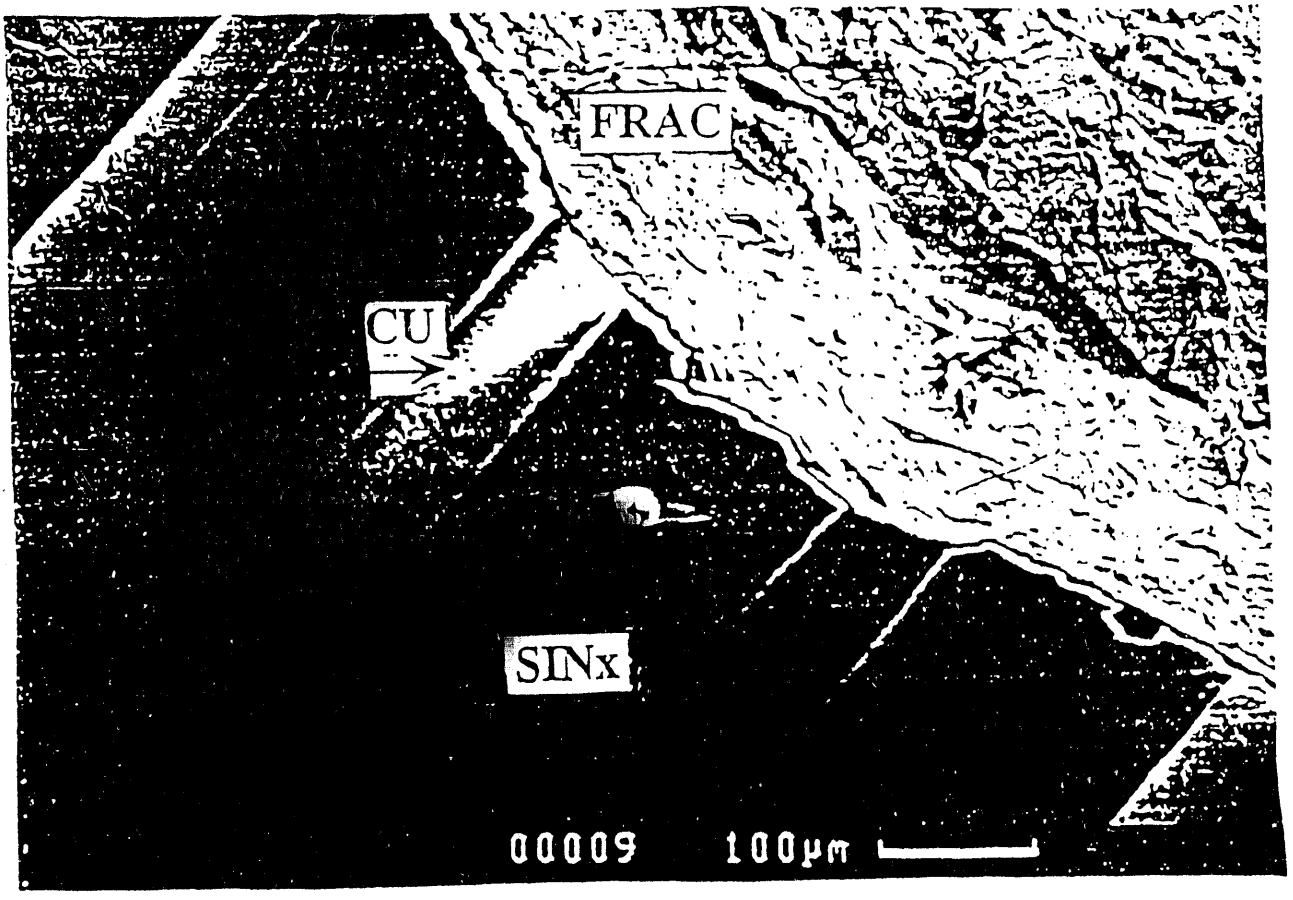

Figure 7 - Detail of crack edge in Sample T18 showing excellent bonding between the Si_3N_4 layer and the sample

Figure 8 - Schematic of the criterion line for crack stability from Hack et al (1)

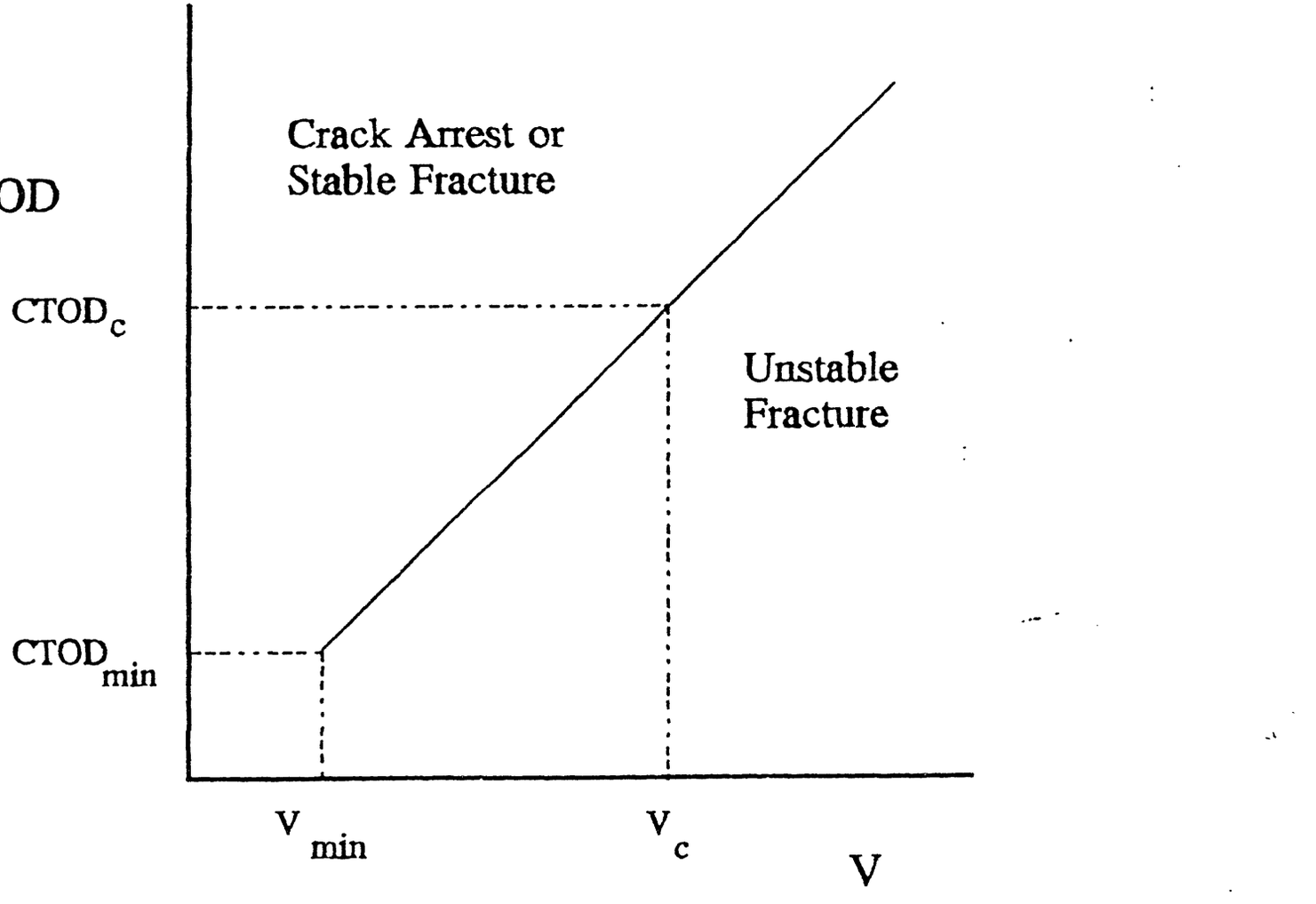

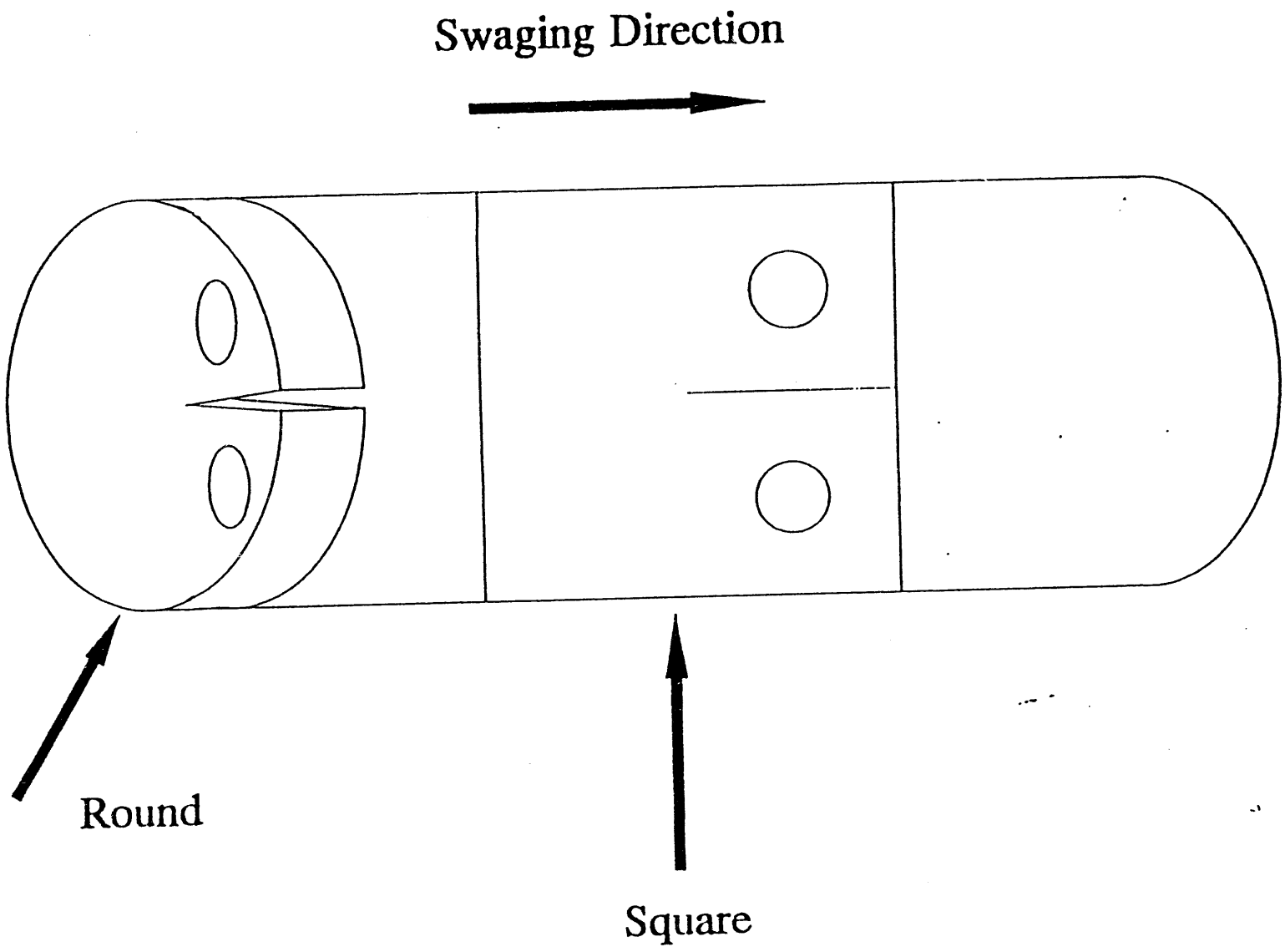

Figure 9 - Schematic of sample geometry for heavy alloy specimens

Figure 10 - Crack stability line for square heavy alloy specimens

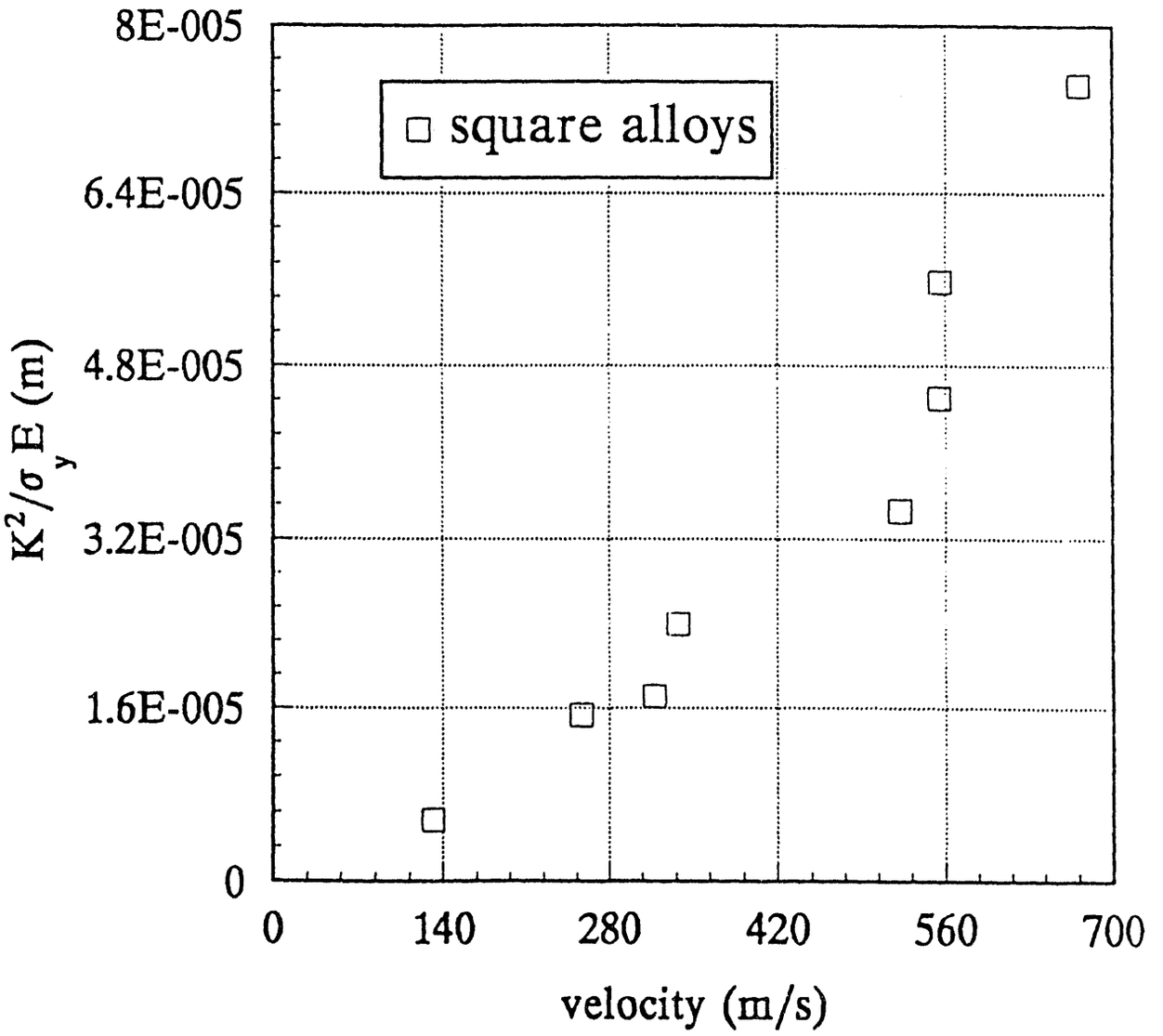

Figure 11 - Crack stability line for annealed pure W Specimens

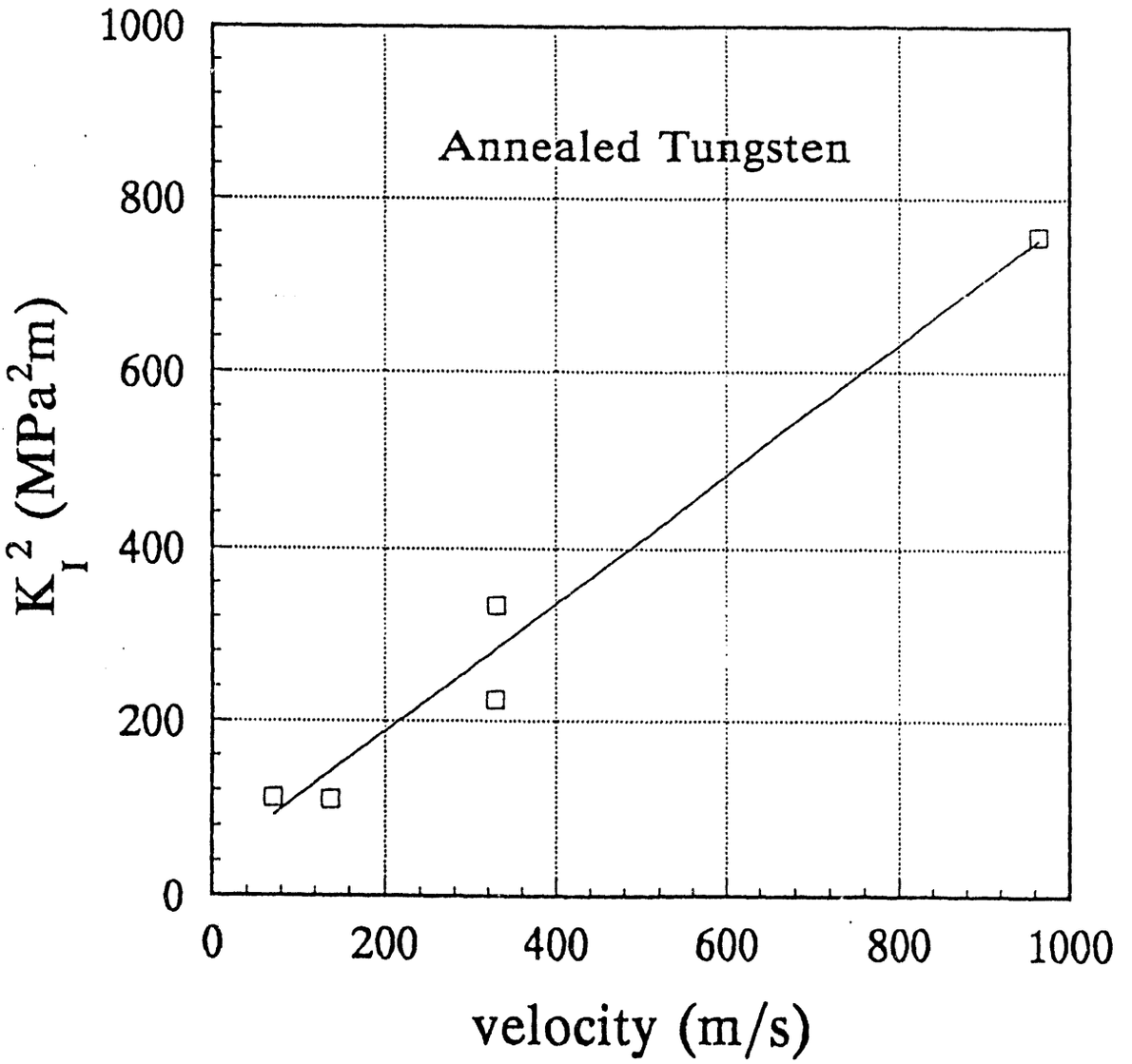

Figure 12 - Comparison of crack stability between round and square heavy alloy specimens

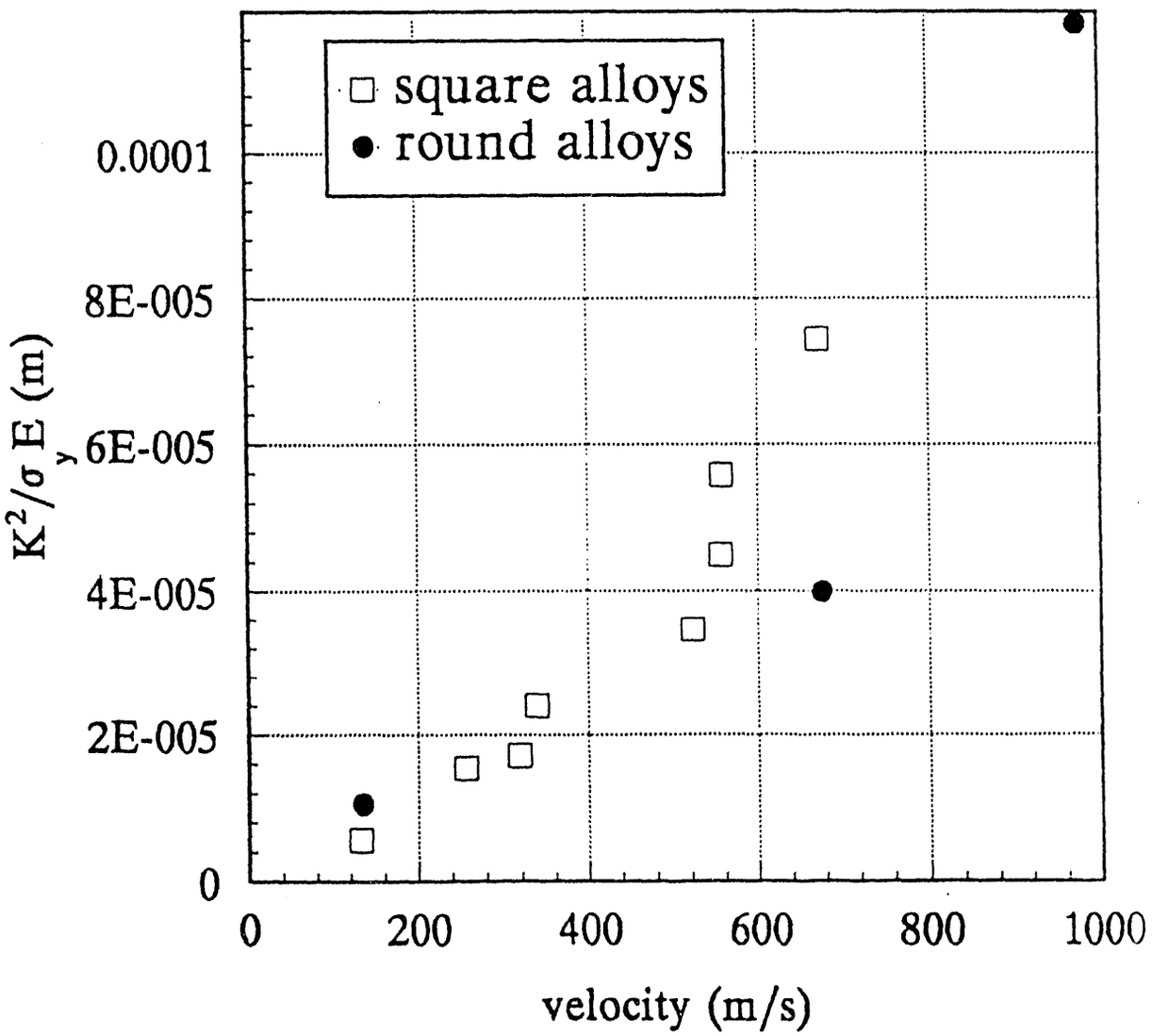

Figure 13 - Comparison of crack stability between p series and square heavy alloy specimens

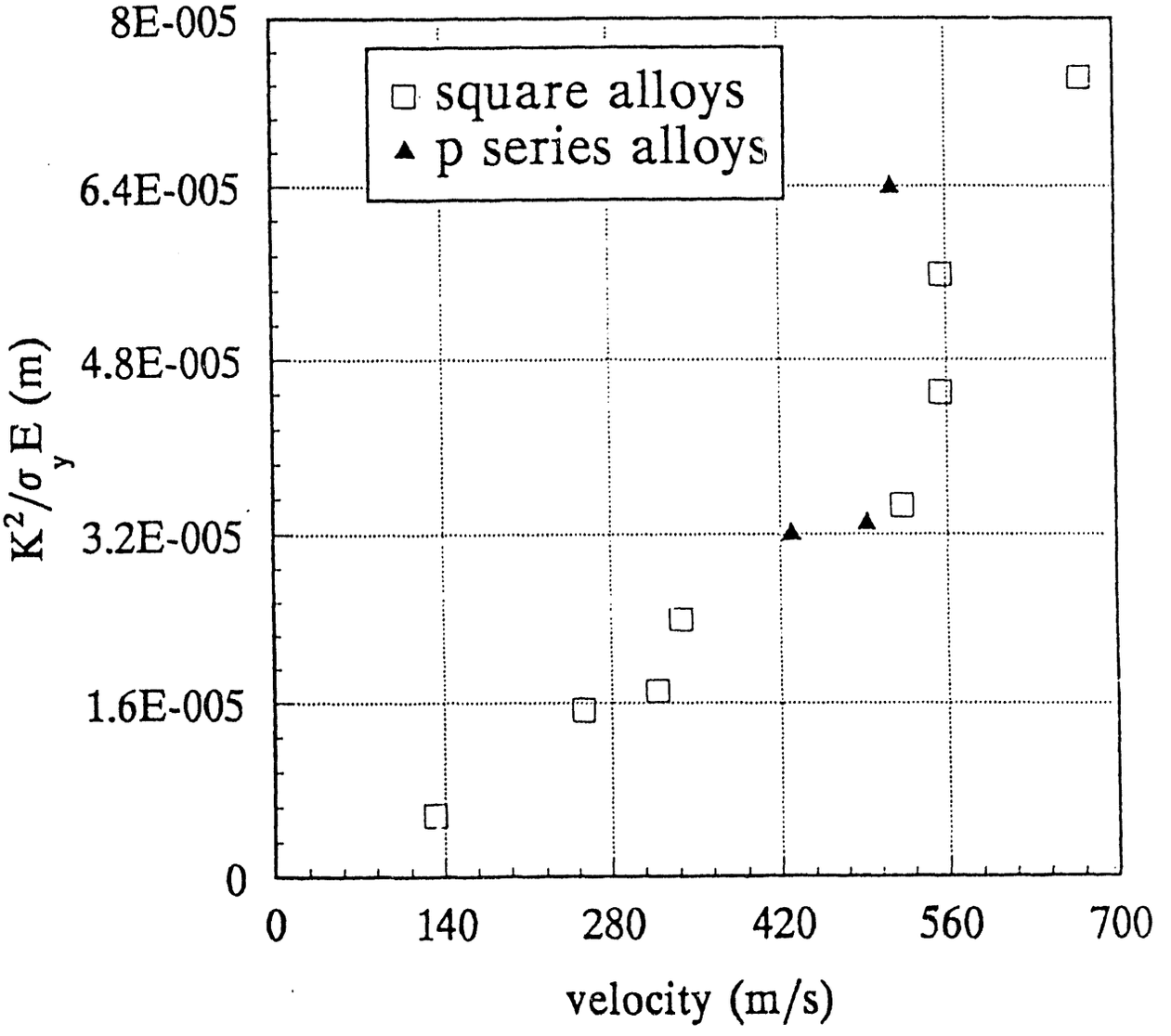

Figure 14 - Comparison of crack stability between as-received and annealed pure W specimens

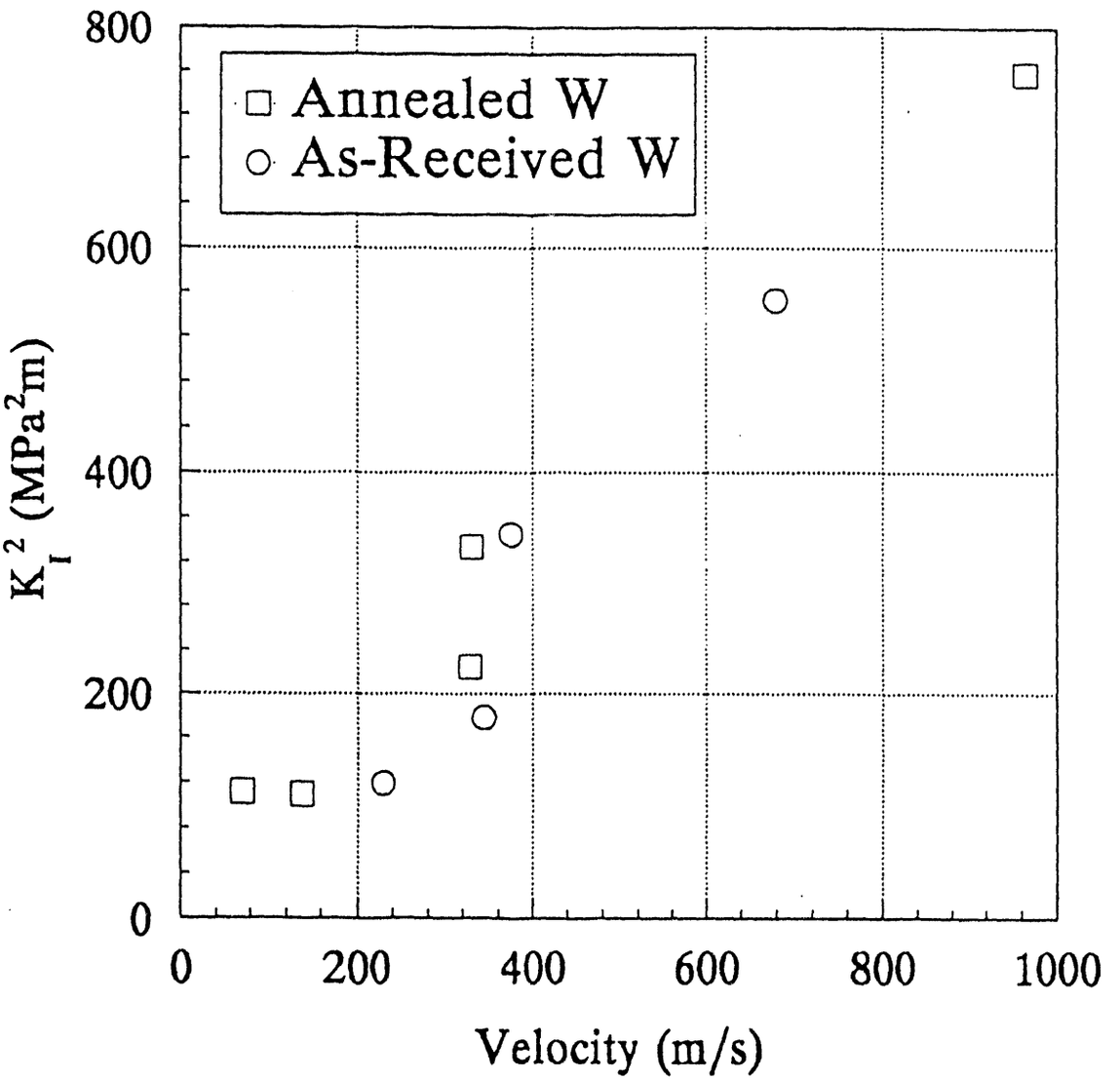

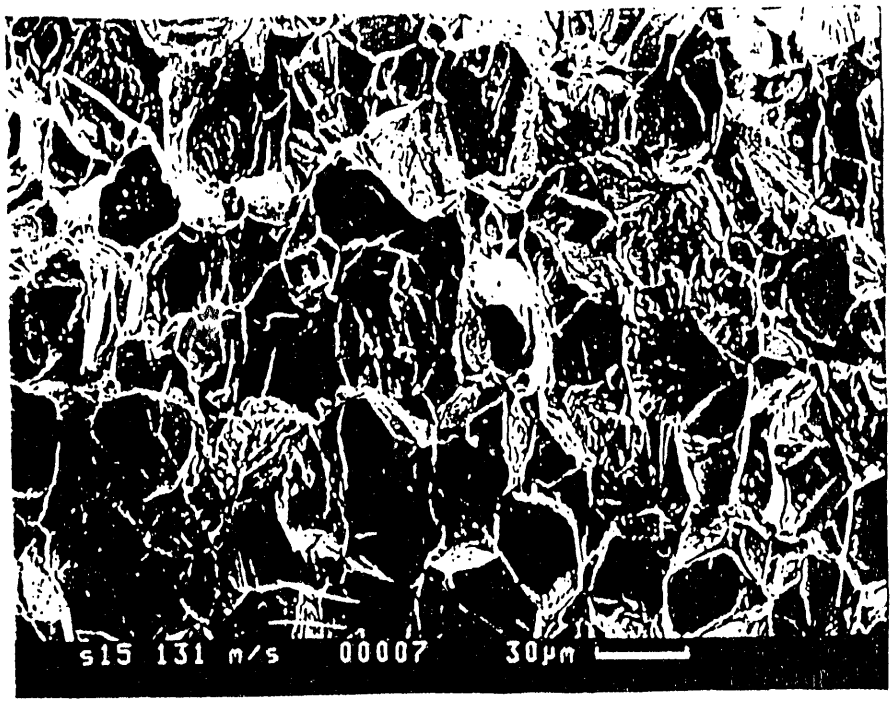

a) Sample S15 - 131 m/s

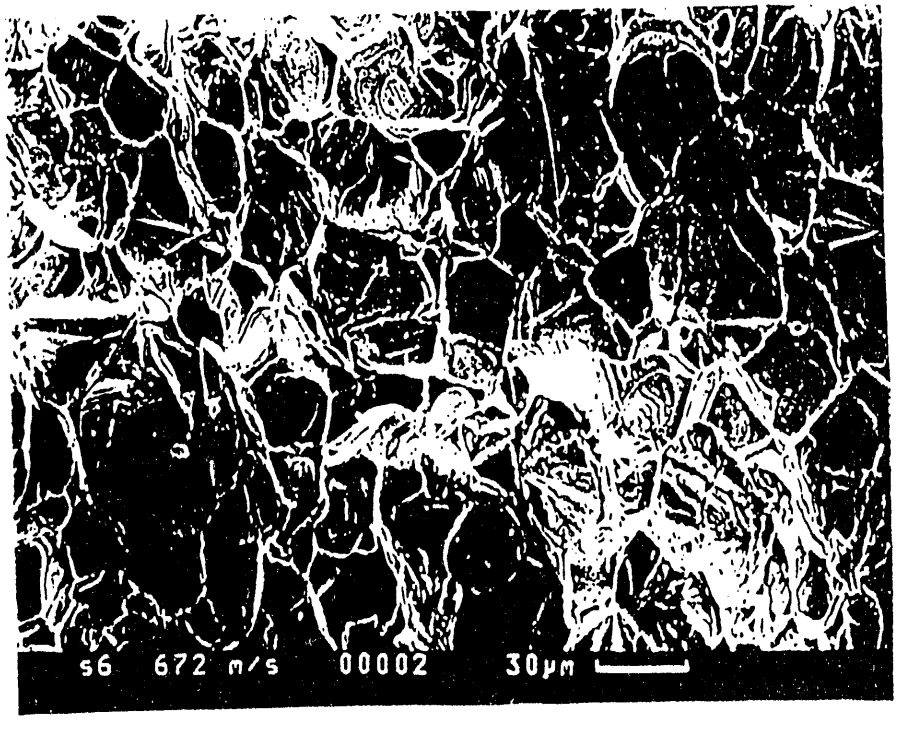

b) Sample S6 - 672 m/s

Figure 15 - Fractography of heavy alloy specimens

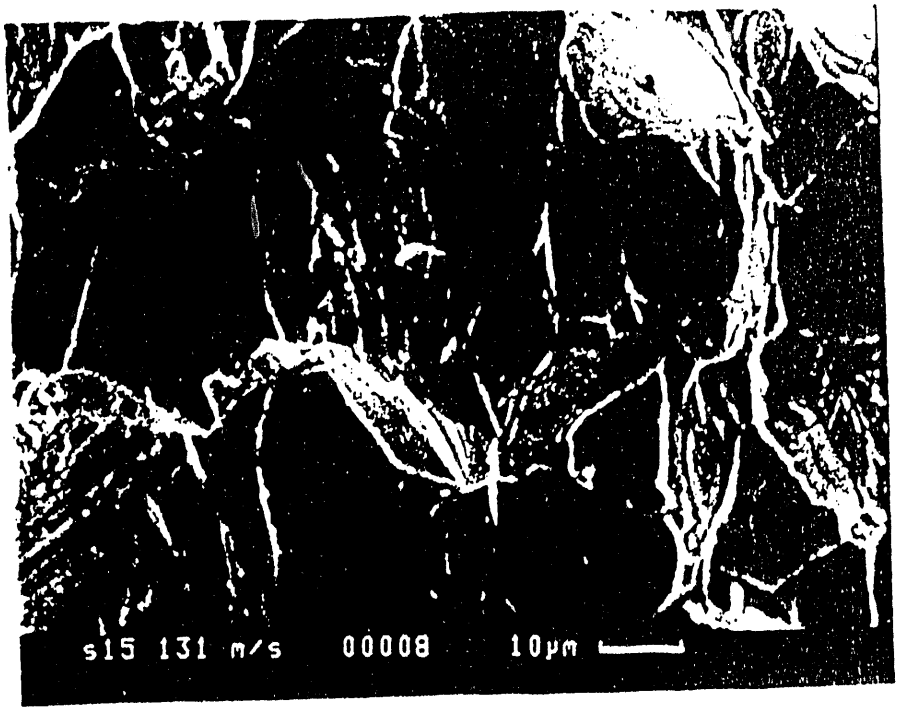

c) Sample S15 - 131 m/s

d) Sample S6 - 672 m/s

Figure 15 - (cont.)

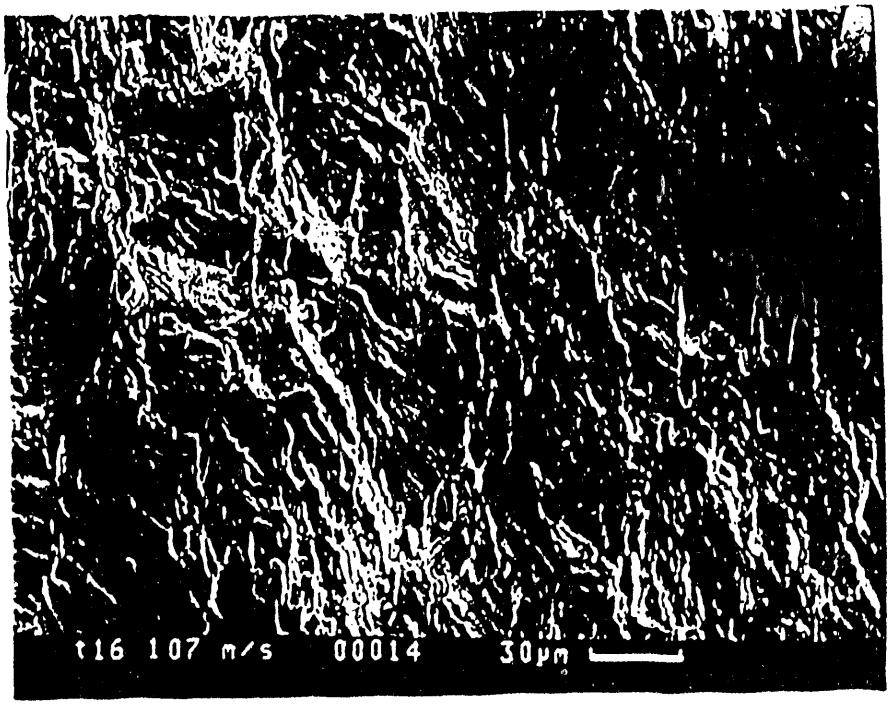

a) Sample T16 - 138 m/s

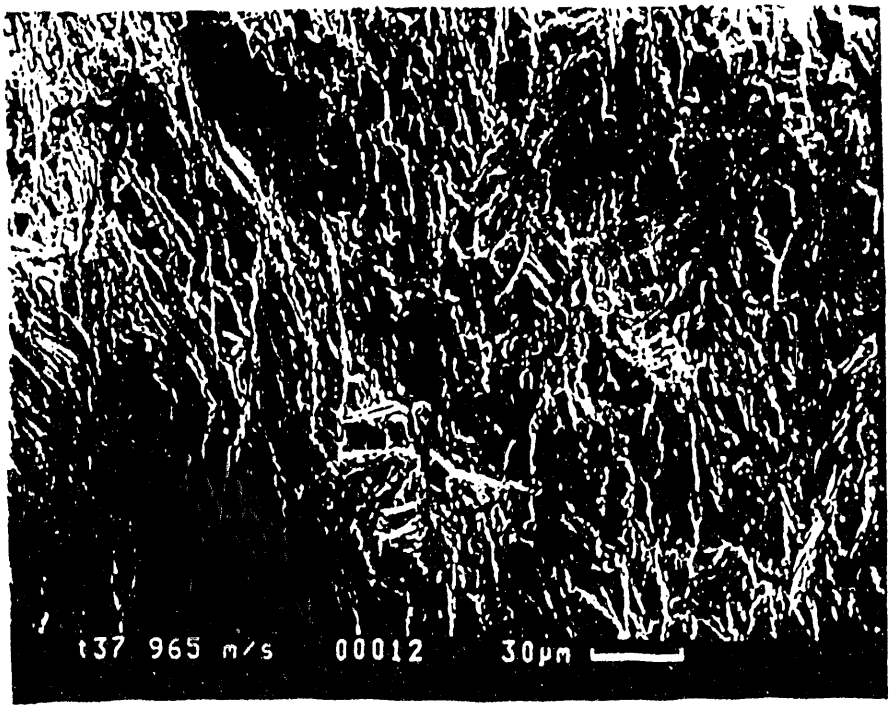

b) Sample T37 - 965 m/s

Figure 16 - Fractography of pure W specimens

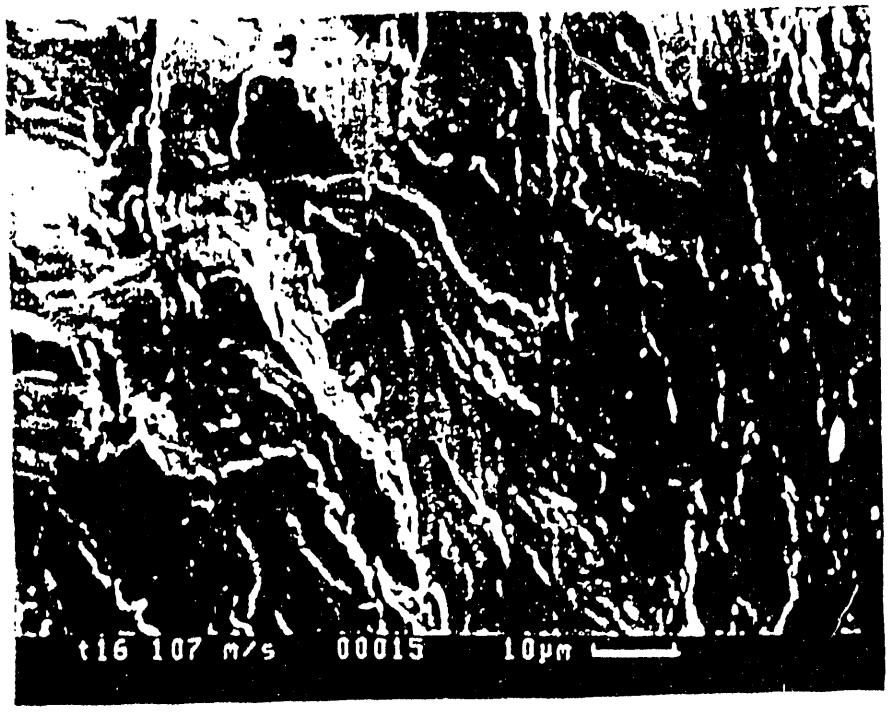

c) Sample T16 - 138 m/s

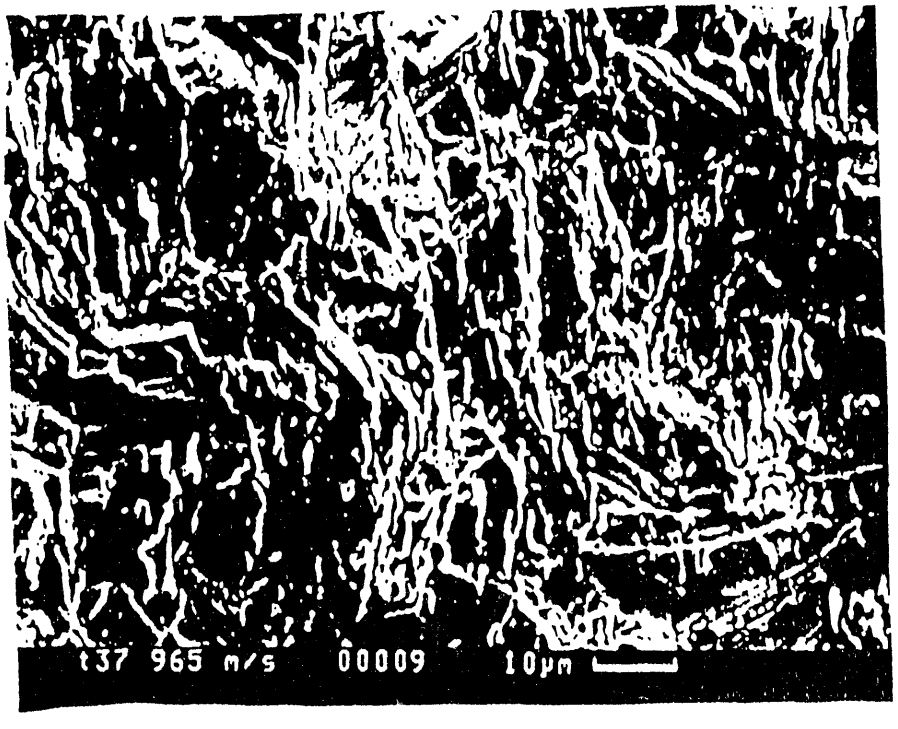

d) Sample T37 - 965 m/s

Figure 16 - (cont.)

Figure 17 - % Cleavage vs velocity for annealed W specimens

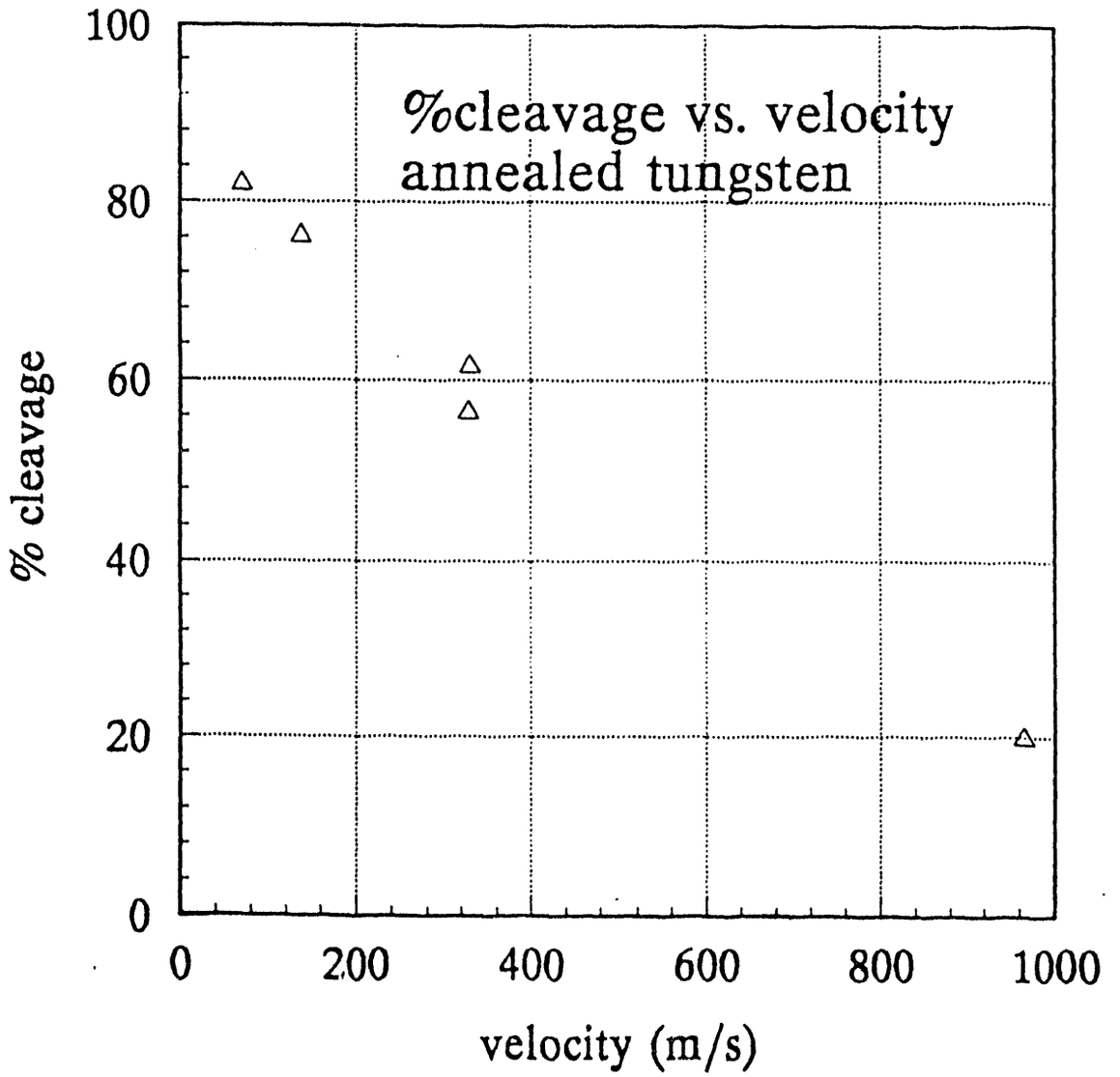

APPENDIX

K vs v DATA FOR ALL SPECIMENS TESTED

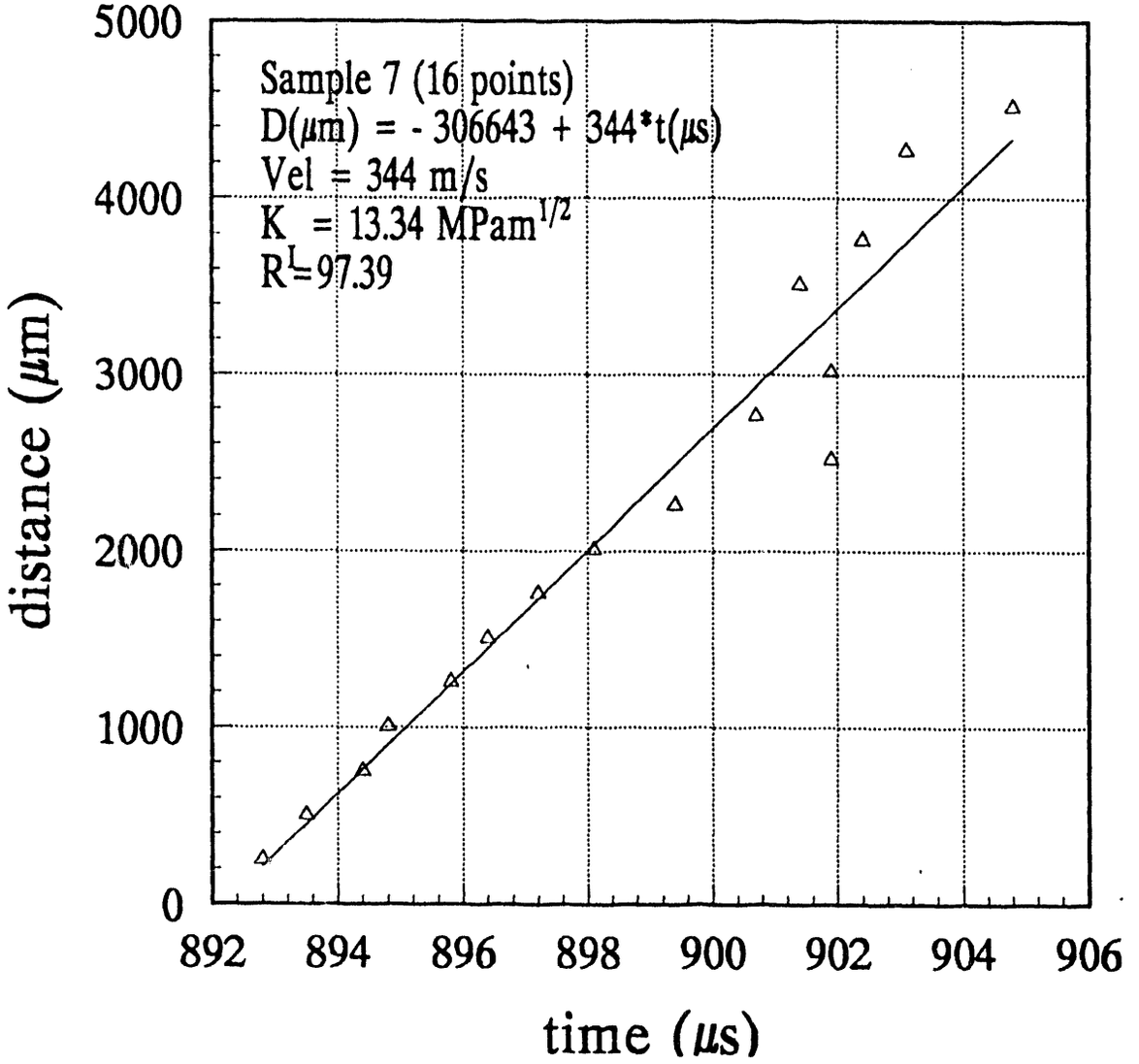
Sample 7 (16 points)
D(μm) = - 306643 + 344*t(μs)
Vel = 344 m/s
K = 13.34 MPam^1/2
R^2=97.39
distance (μm)
time (μs)
0
1000
2000
3000
4000
5000
892
894
896
898
900
902
904
906

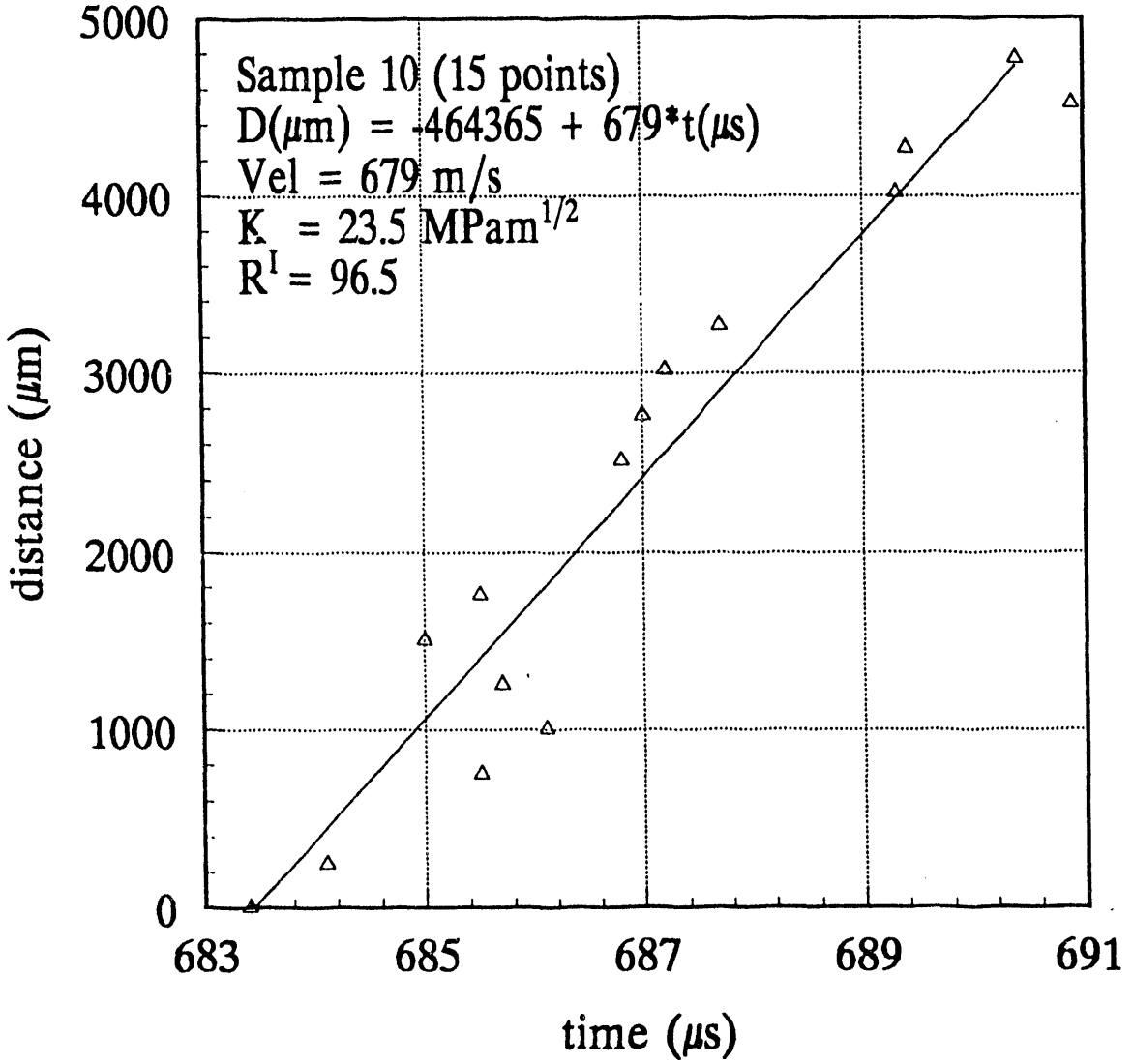
Sample 10 (15 points)
D(μm) = -464365 + 679*t(μs)
Vel = 679 m/s
K = 23.5 MPam^1/2
R^I = 96.5
5000
4000
3000
2000
1000
0
distance (μm)
683
685
687
689
691
time (μs)

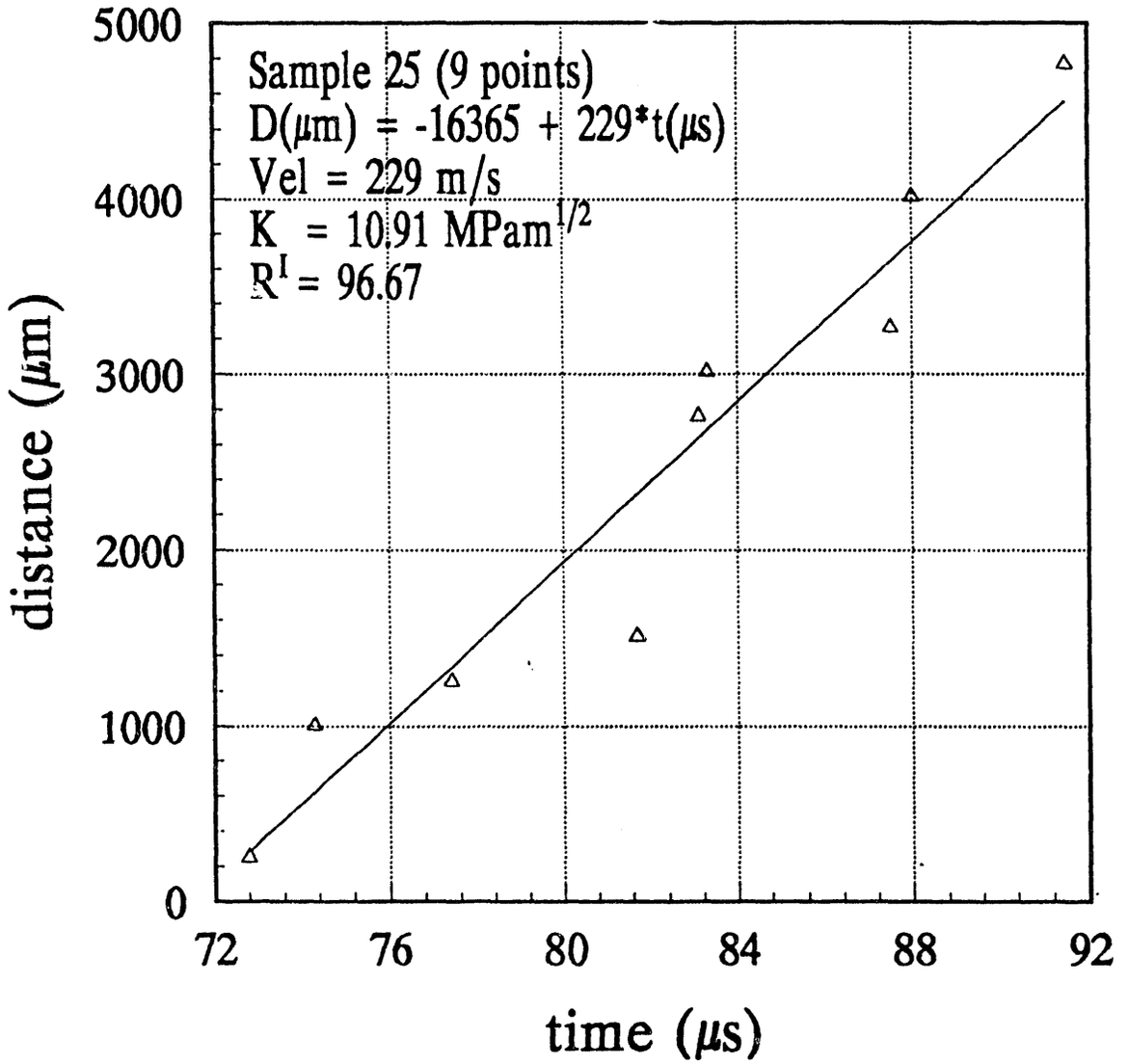
Sample 25 (9 points)
D(μm) = -16365 + 229*t(μs)
Vel = 229 m/s
K = 10.91 MPam^1/2
R^I = 96.67
5000
4000
3000
2000
1000
0
distance (μm)
72
76
80
84
88
92
time (μs)

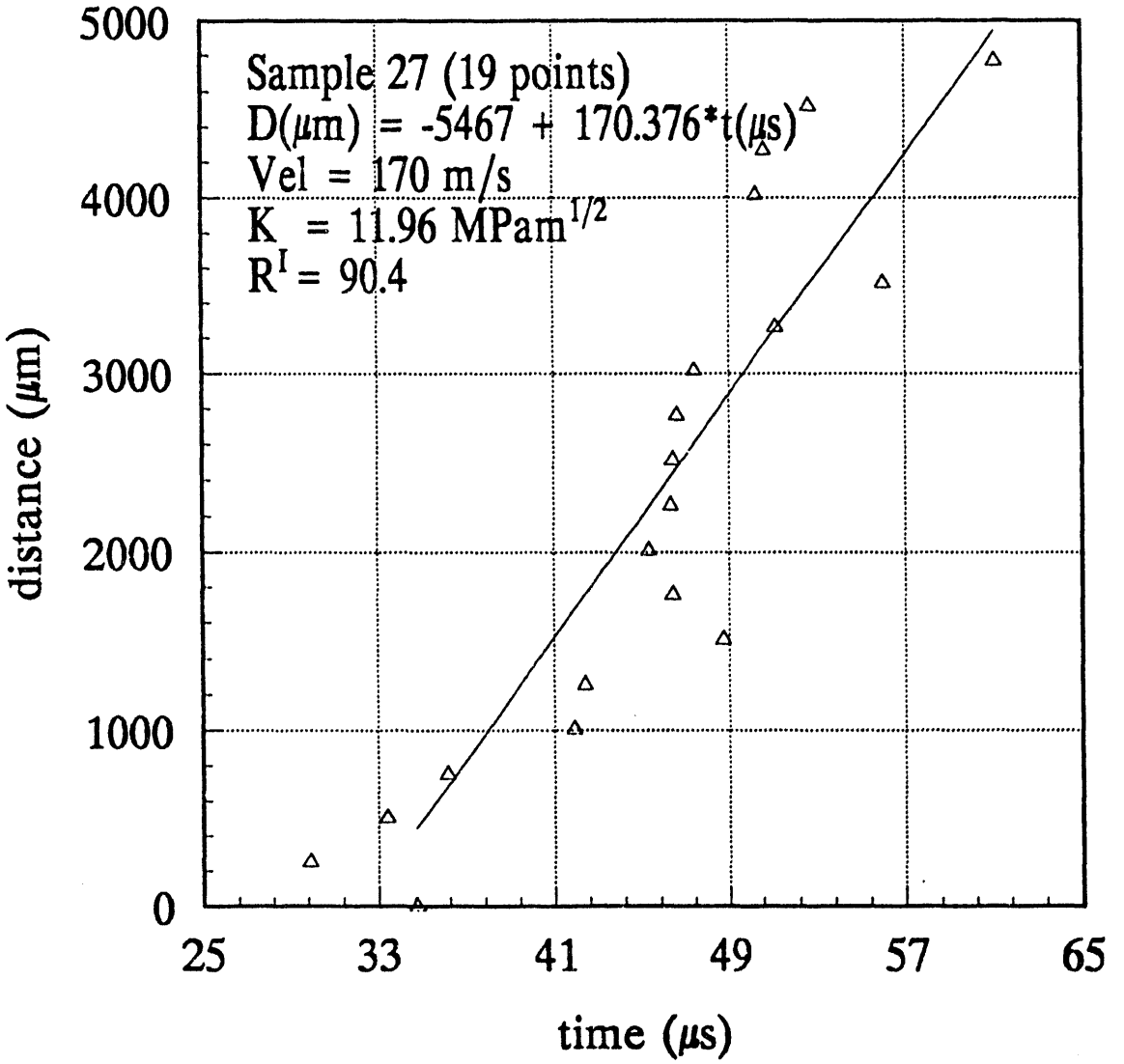
Sample 27 (19 points)
D(μm) = -5467 + 170.376*t(μs)^Δ
Vel = 170 m/s
K = 11.96 MPam^1/2
R^I = 90.4
5000
4000
3000
2000
1000
0
distance (μm)
25
33
41
49
57
65
time (μs)

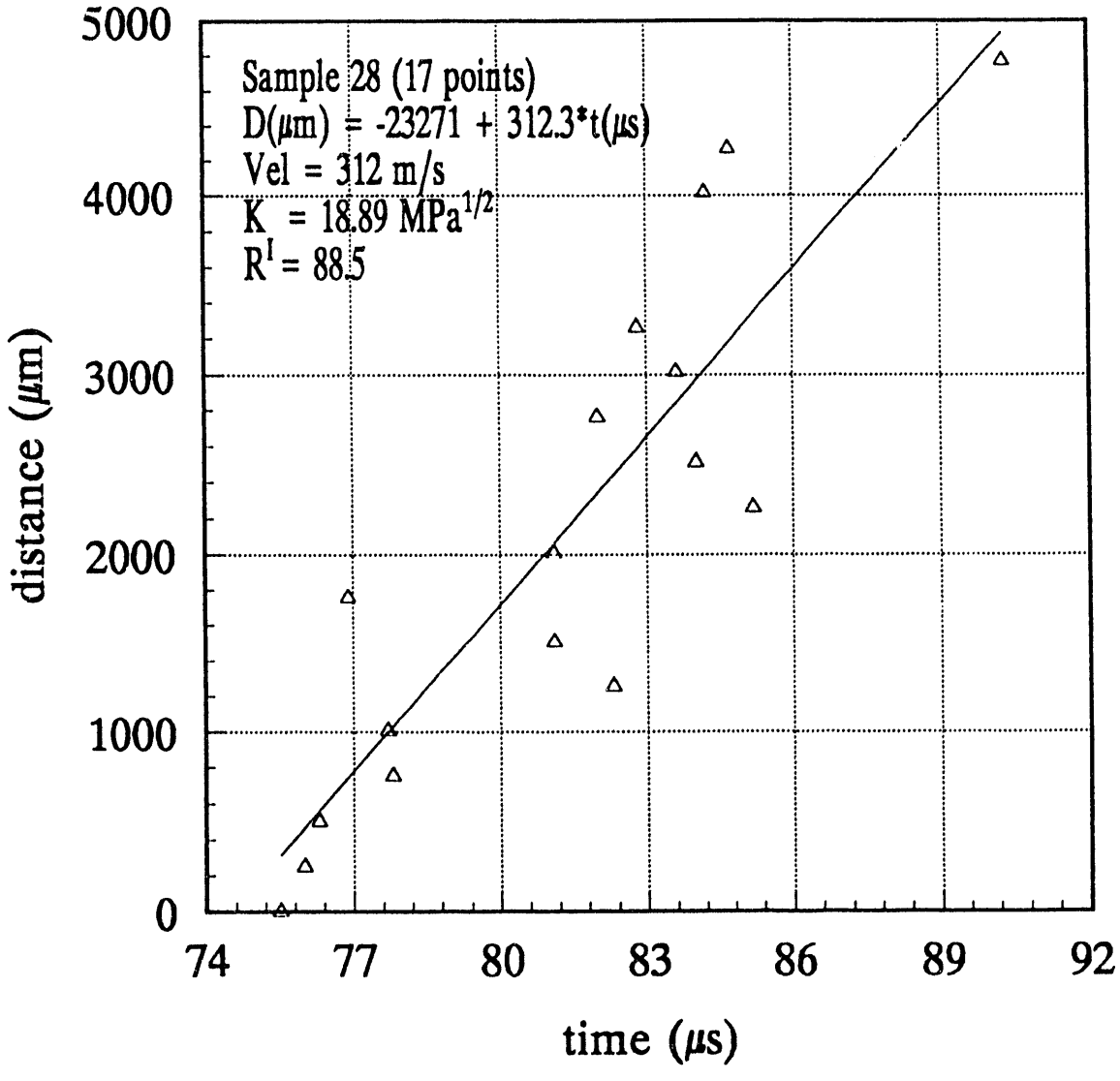
Sample 28 (17 points)
D(μm) = -23271 + 312.3*t(μs)
Vel = 312 m/s
K = 18.89 MPa^1/2
R^I = 88.5
5000
4000
3000
2000
1000
0
distance (μm)
74
77
80
83
86
89
92
time (μs)

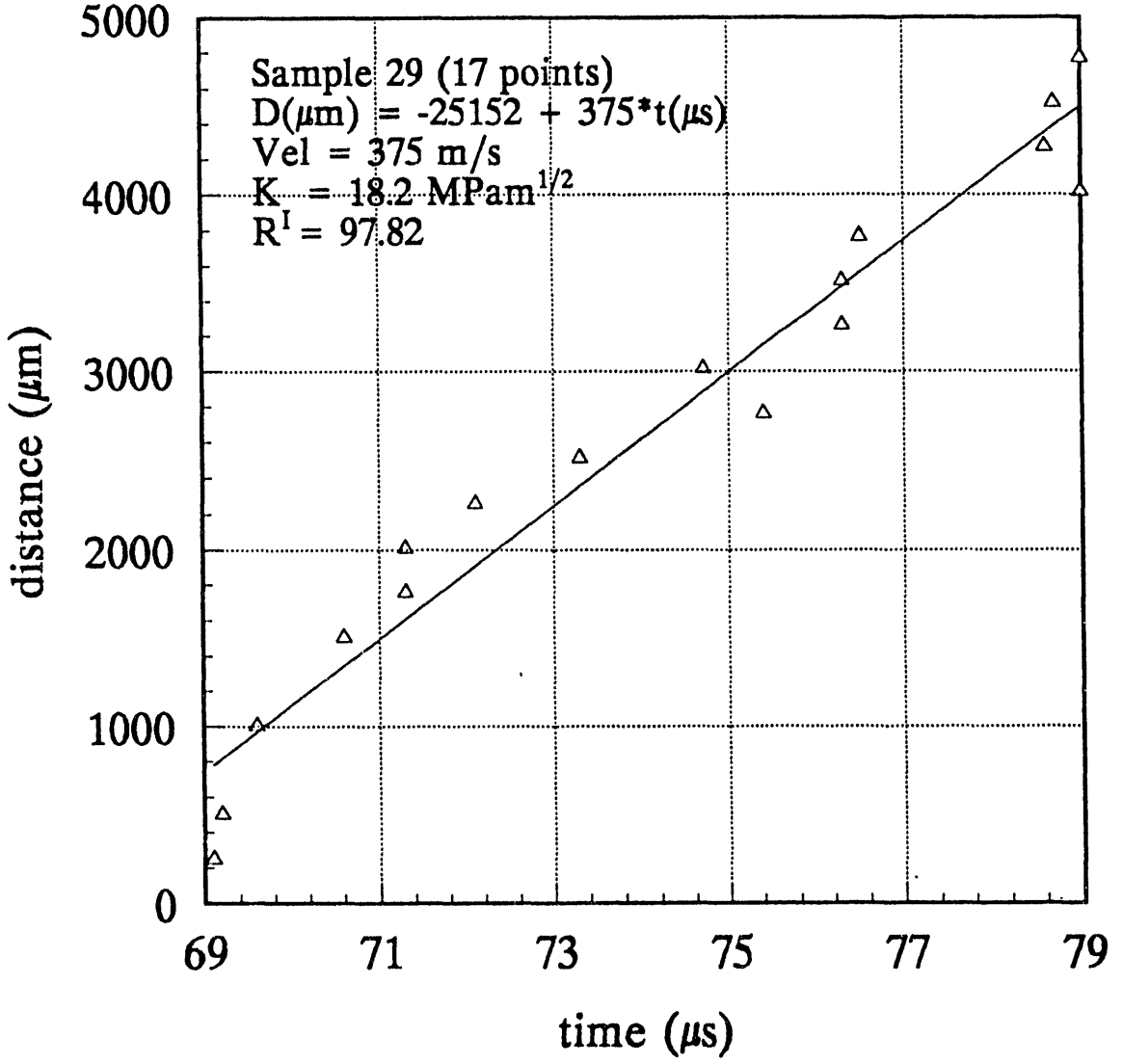
Sample 29 (17 points)
D(μm) = -25152 + 375*t(μs)
Vel = 375 m/s
K = 18.2 MPam^1/2
R^I = 97.82
5000
4000
3000
2000
1000
0
distance (μm)
69
71
73
75
77
79
time (μs)

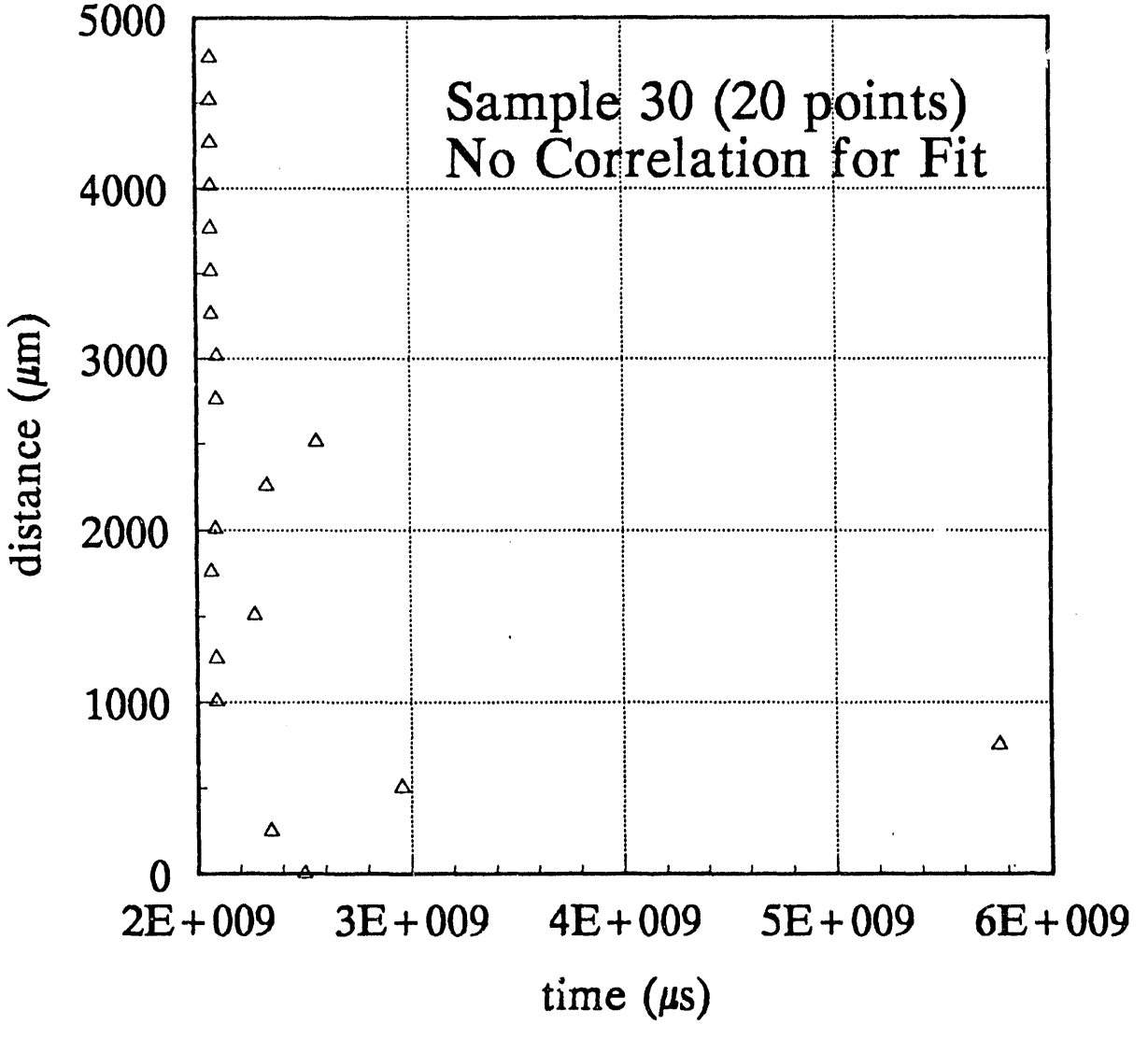
Sample 30 (20 points)
No Correlation for Fit
5000
4000
3000
2000
1000
0
distance (μm)
2E+009
3E+009
4E+009
5E+009
6E+009
time (μs)

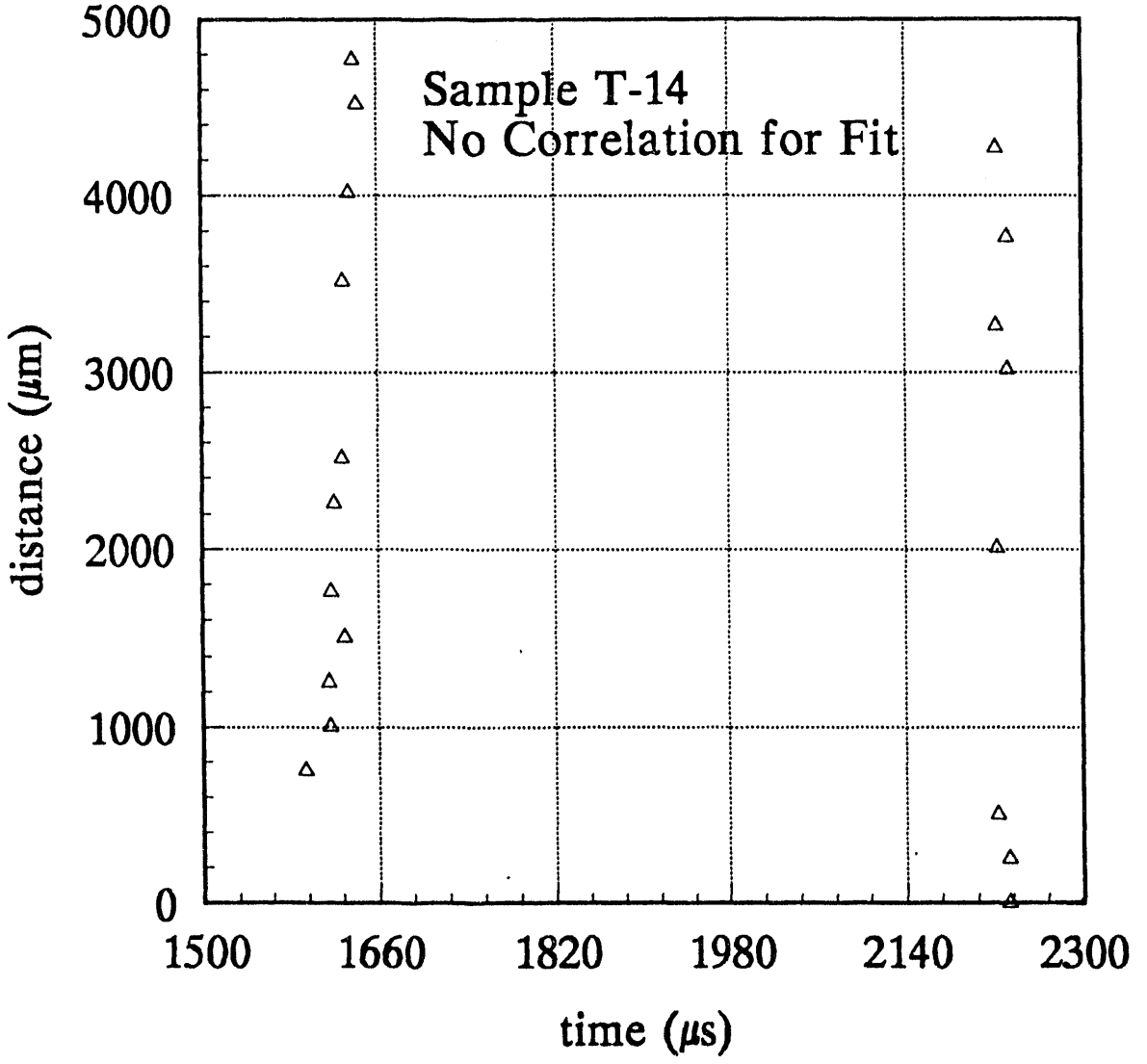
Sample T-14
No Correlation for Fit
5000
4000
3000
2000
1000
0
distance (μm)
1500
1660
1820
1980
2140
2300
time (μs)

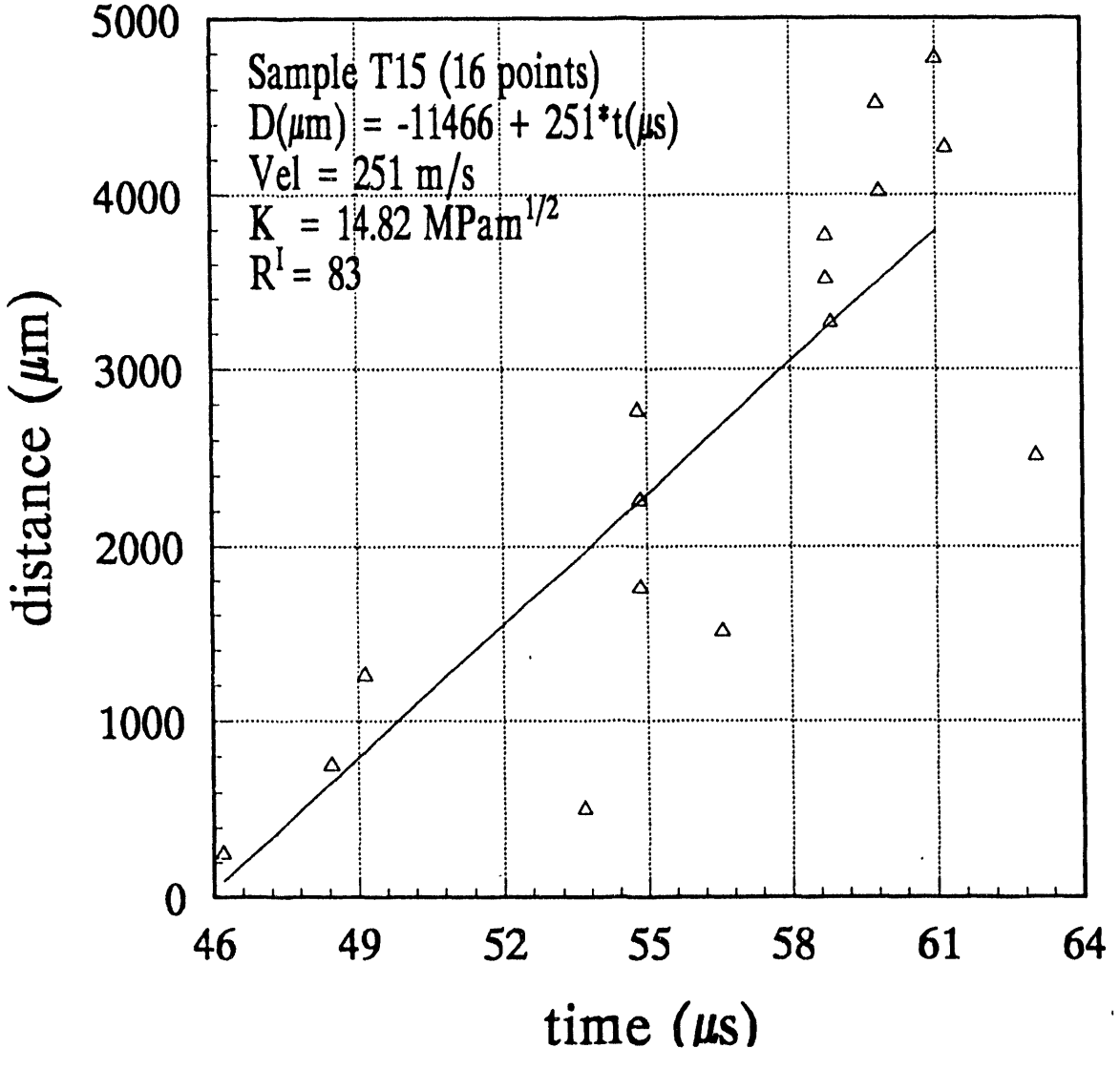
Sample T15 (16 points)
D(μm) = -11466 + 251*t(μs)
Vel = 251 m/s
K = 14.82 MPam^1/2
R^I = 83
5000
4000
3000
2000
1000
0
distance (μm)
46
49
52
55
58
61
64
time (μs)

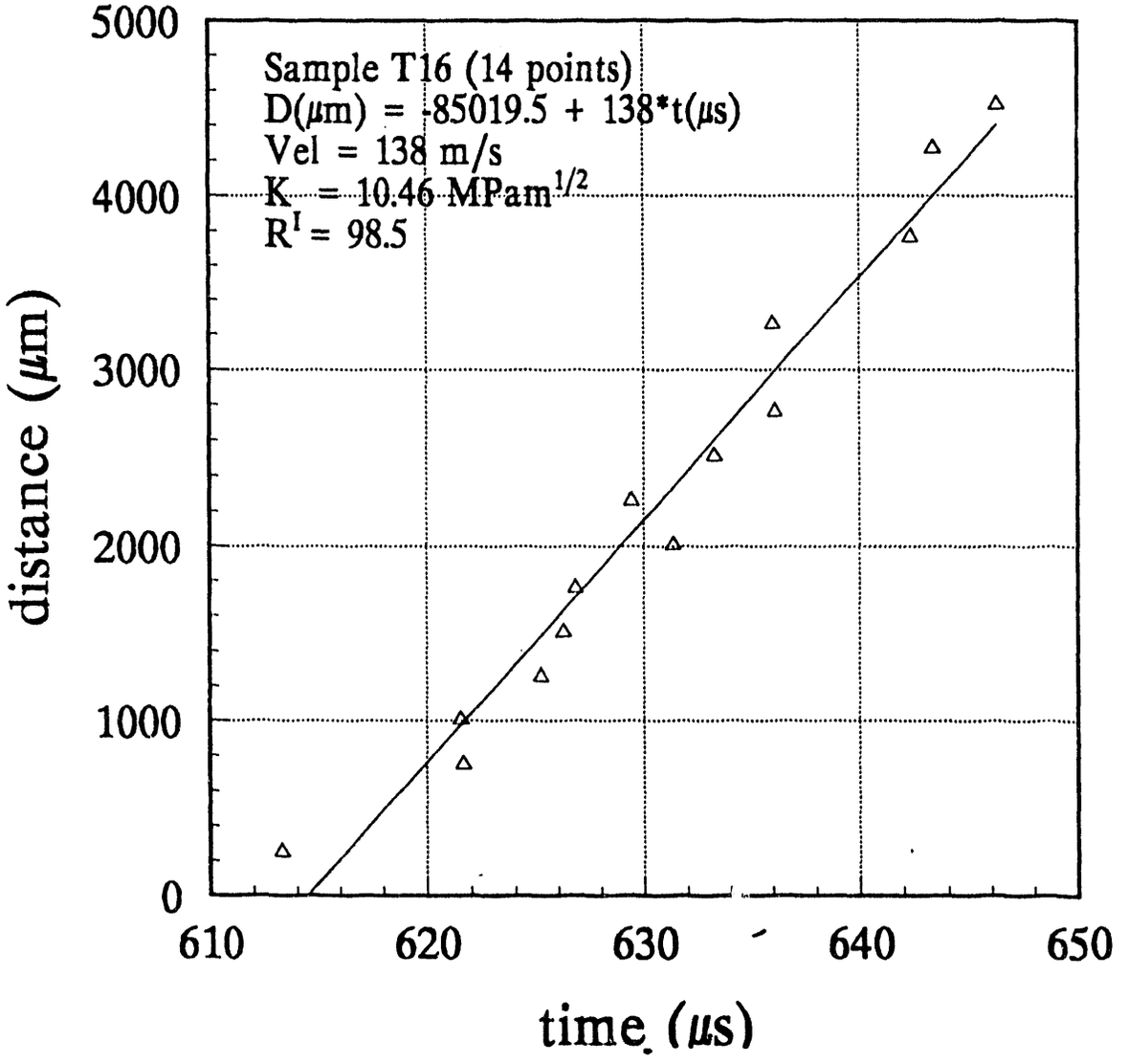
Sample T16 (14 points)
D(μm) = -85019.5 + 138*t(μs)
Vel = 138 m/s
K = 10.46 MPam^1/2
R^I = 98.5
distance (μm)
time (μs)
0
1000
2000
3000
4000
5000
610
620
630
640
650

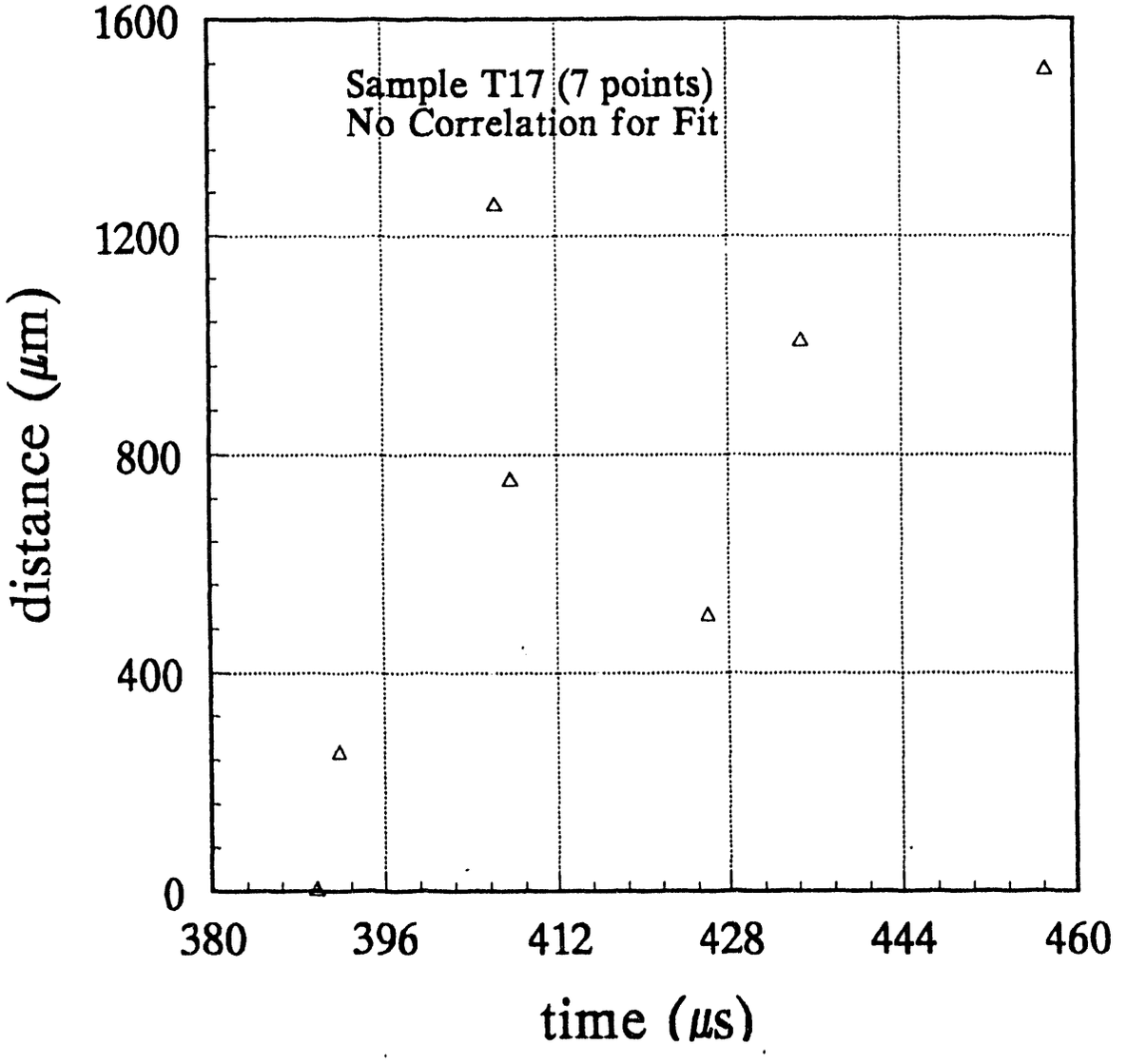
Sample T17 (7 points)
No Correlation for Fit
1600
1200
800
400
0
distance (μm)
380
396
412
428
444
460
time (μs)

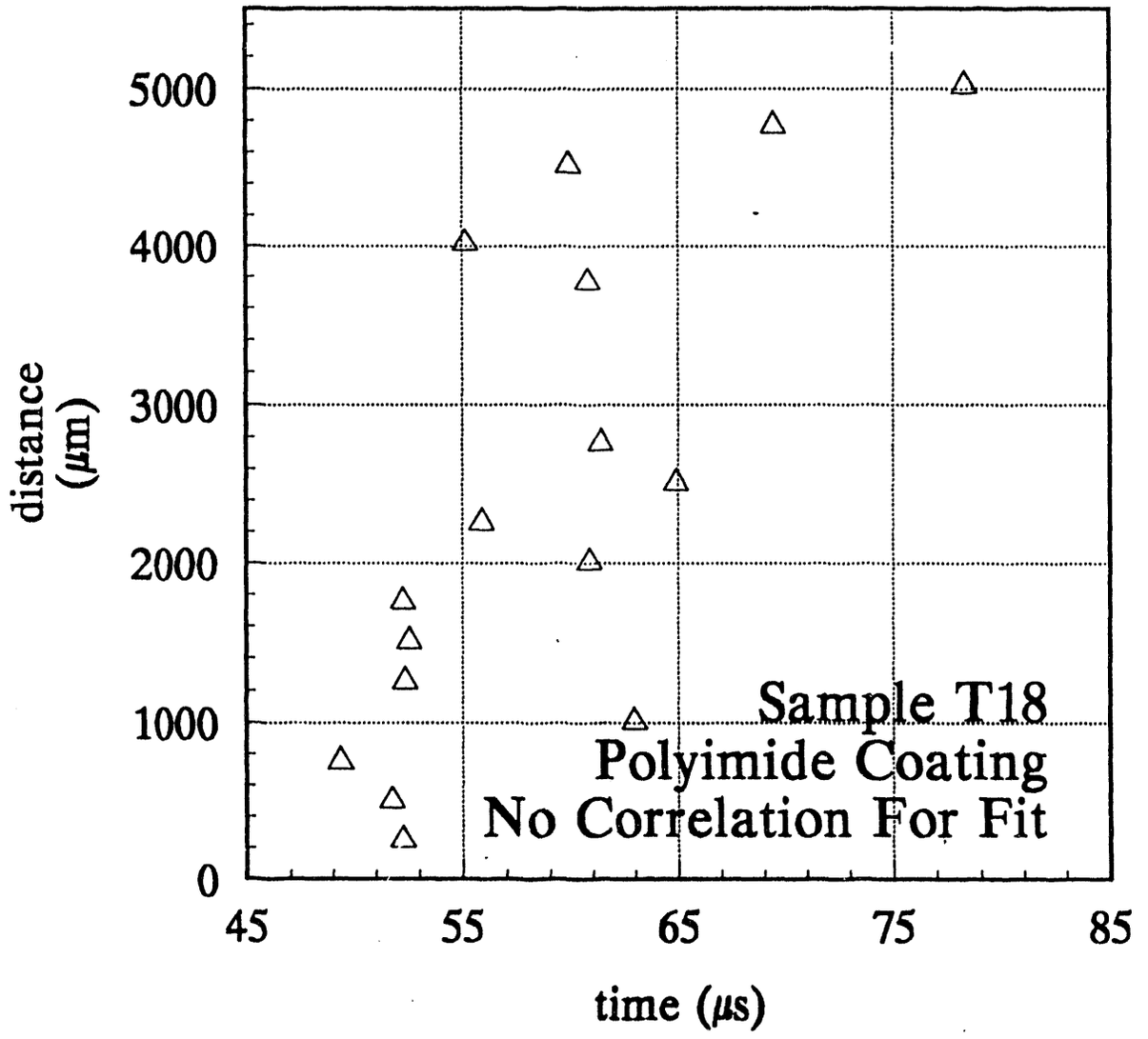
5000
4000
3000
2000
1000
0
distance (μm)
45
55
65
75
85
time (μs)
Sample T18
Polyimide Coating
No Correlation For Fit

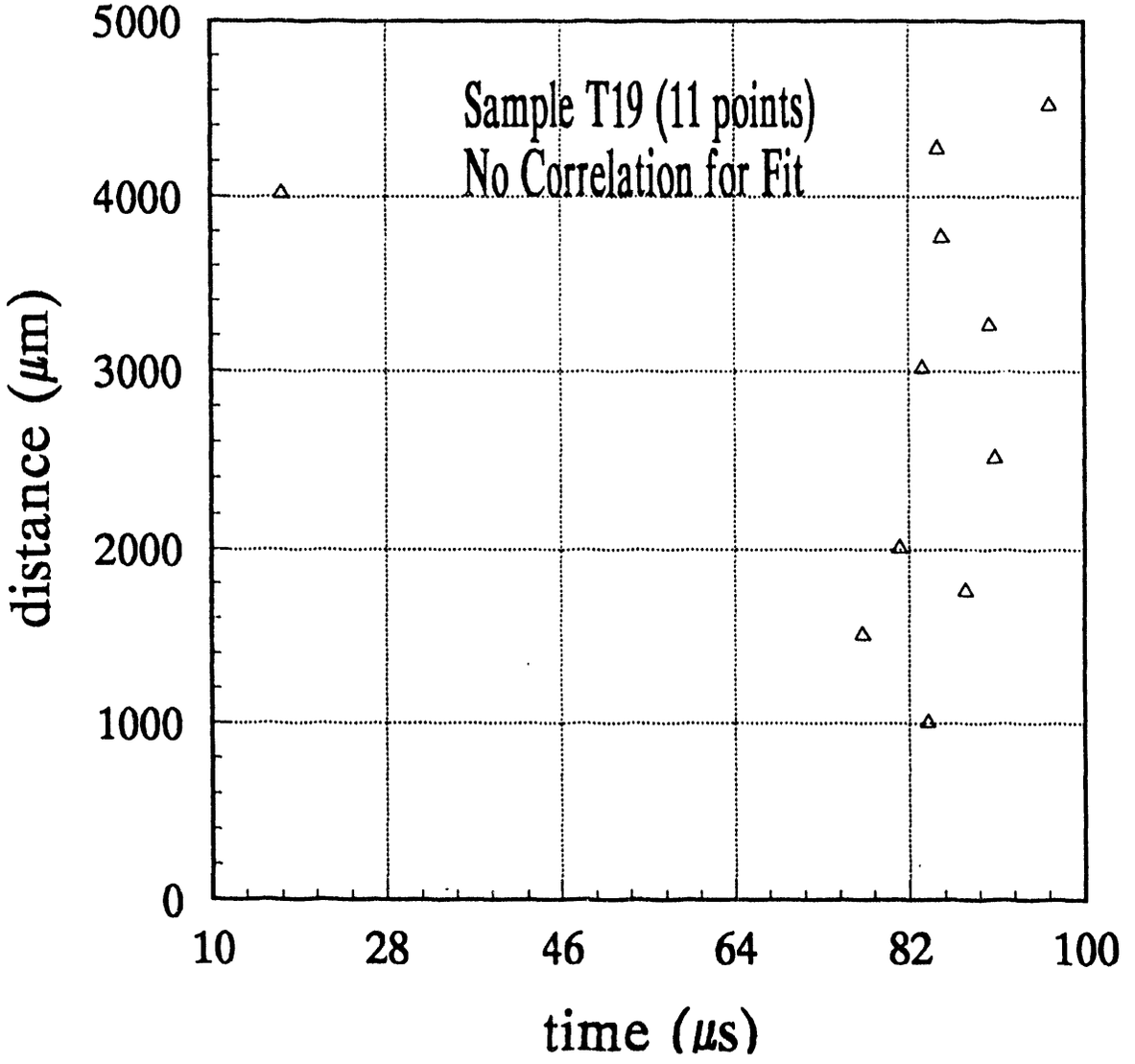
Sample T19 (11 points)
No Correlation for Fit
5000
4000
3000
2000
1000
0
distance (μm)
10
28
46
64
82
100
time (μs)

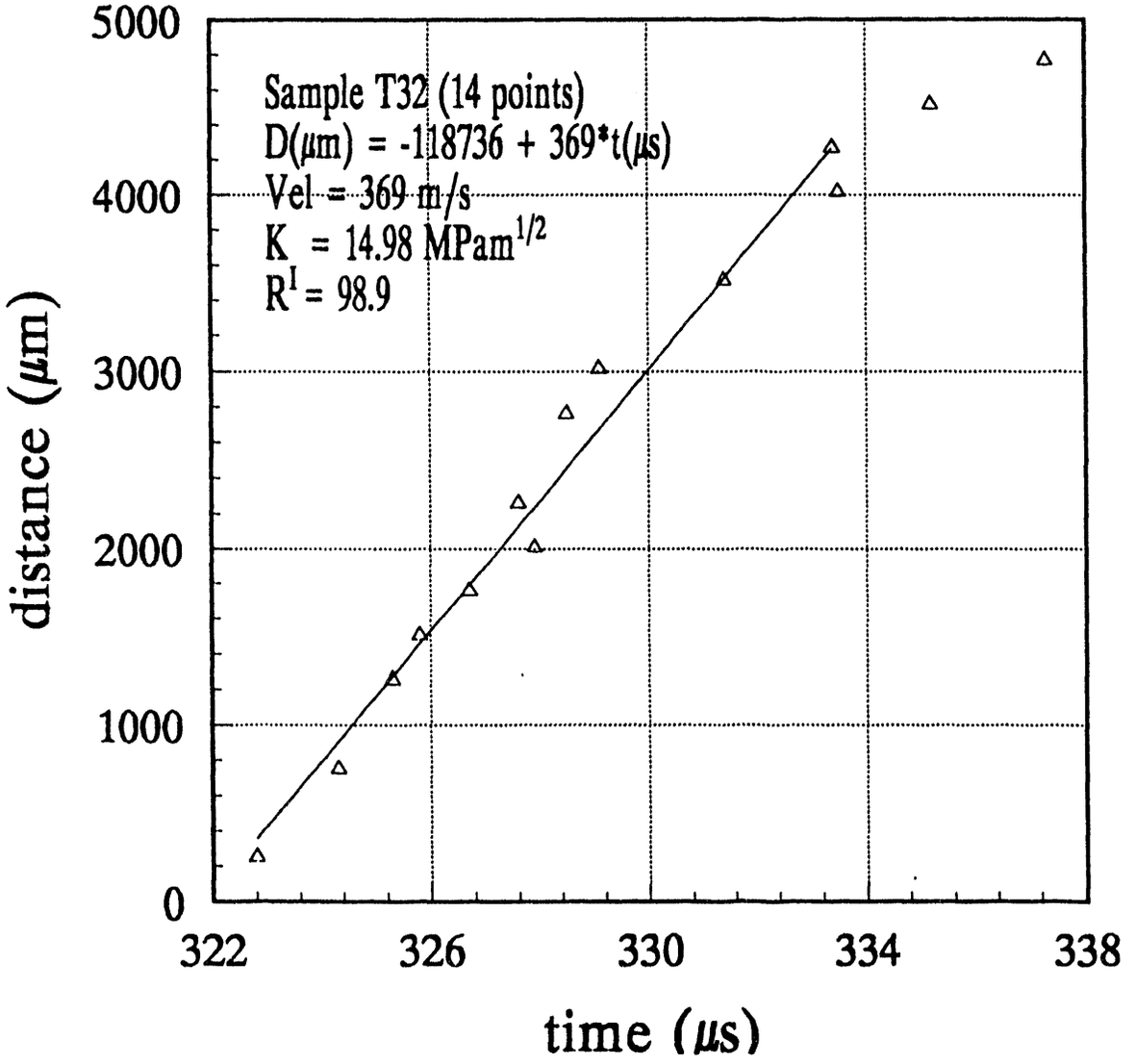
Sample T32 (14 points)
D(μm) = -118736 + 369*t(μs)
Vel = 369 m/s
K = 14.98 MPam^1/2
R^I = 98.9
5000
4000
3000
2000
1000
0
distance (μm)
322
326
330
334
338
time (μs)

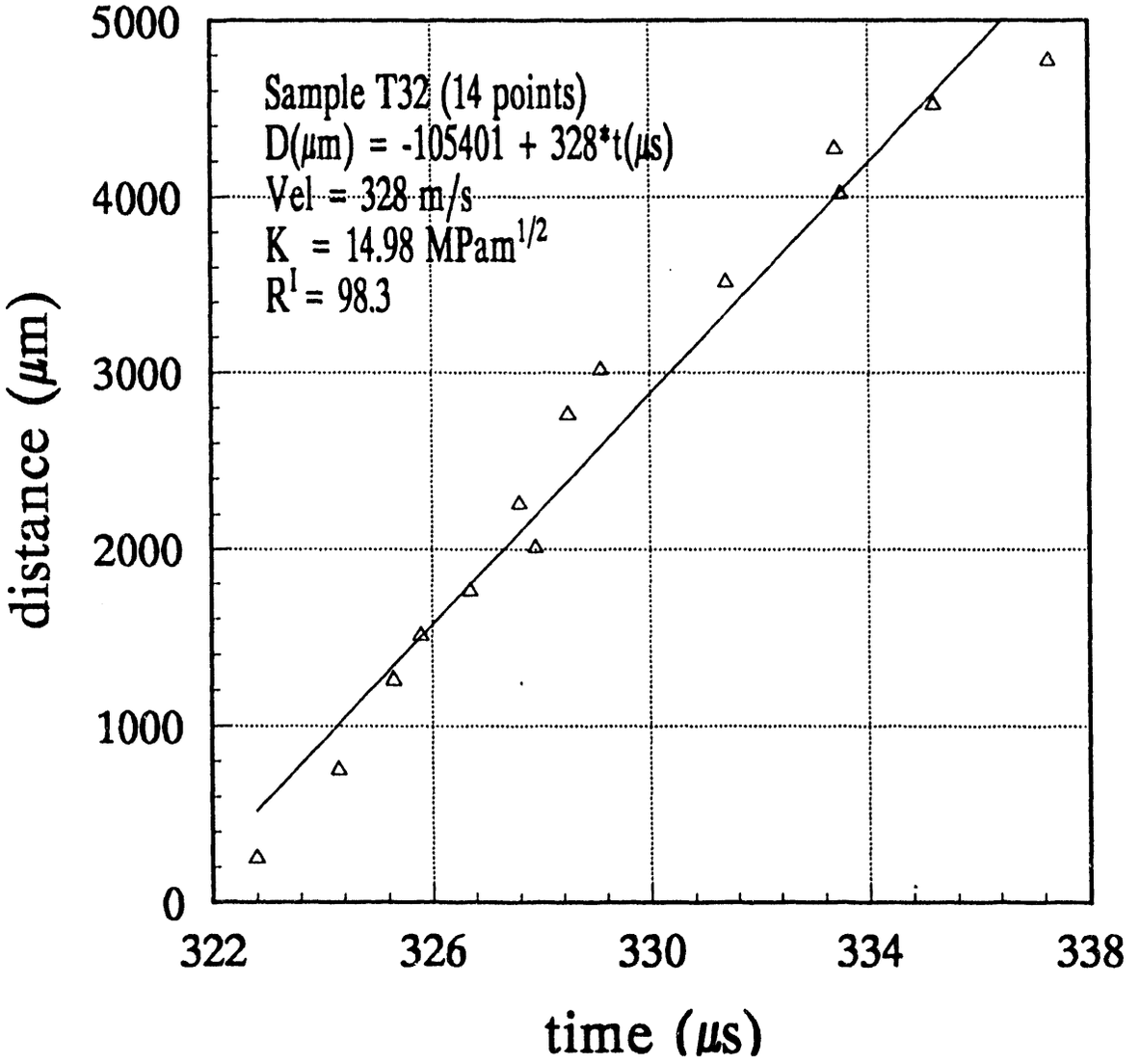
Sample T32 (14 points)
D(μm) = -105401 + 328*t(μs)
Vel = 328 m/s
K = 14.98 MPam^1/2
R^I = 98.3
5000
4000
3000
2000
1000
0
distance (μm)
322
326
330
334
338
time (μs)

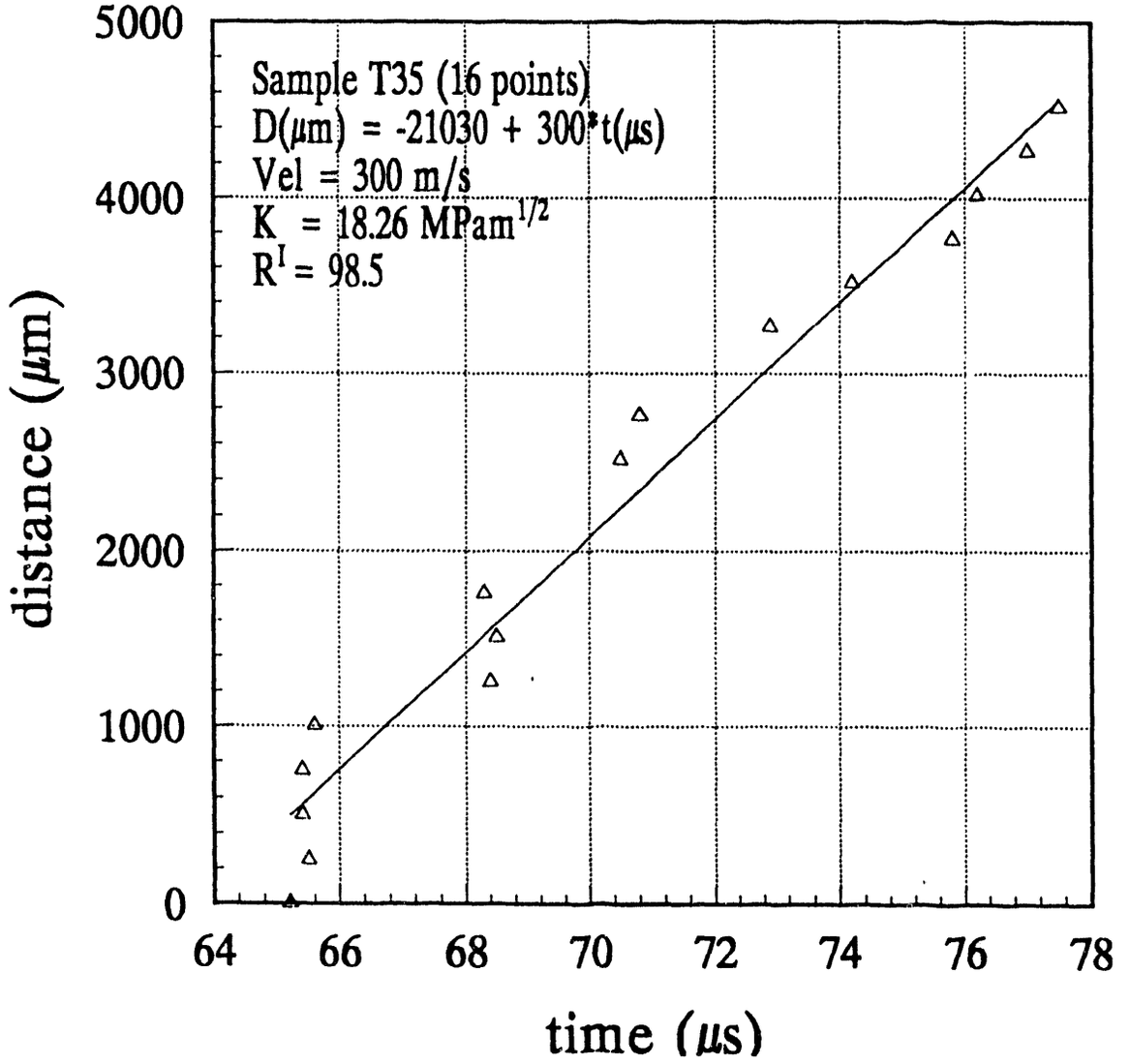
Sample T35 (16 points)
D(μm) = -21030 + 300*t(μs)
Vel = 300 m/s
K = 18.26 MPam^1/2
R^I = 98.5
distance (μm)
time (μs)
0
1000
2000
3000
4000
5000
64
66
68
70
72
74
76
78

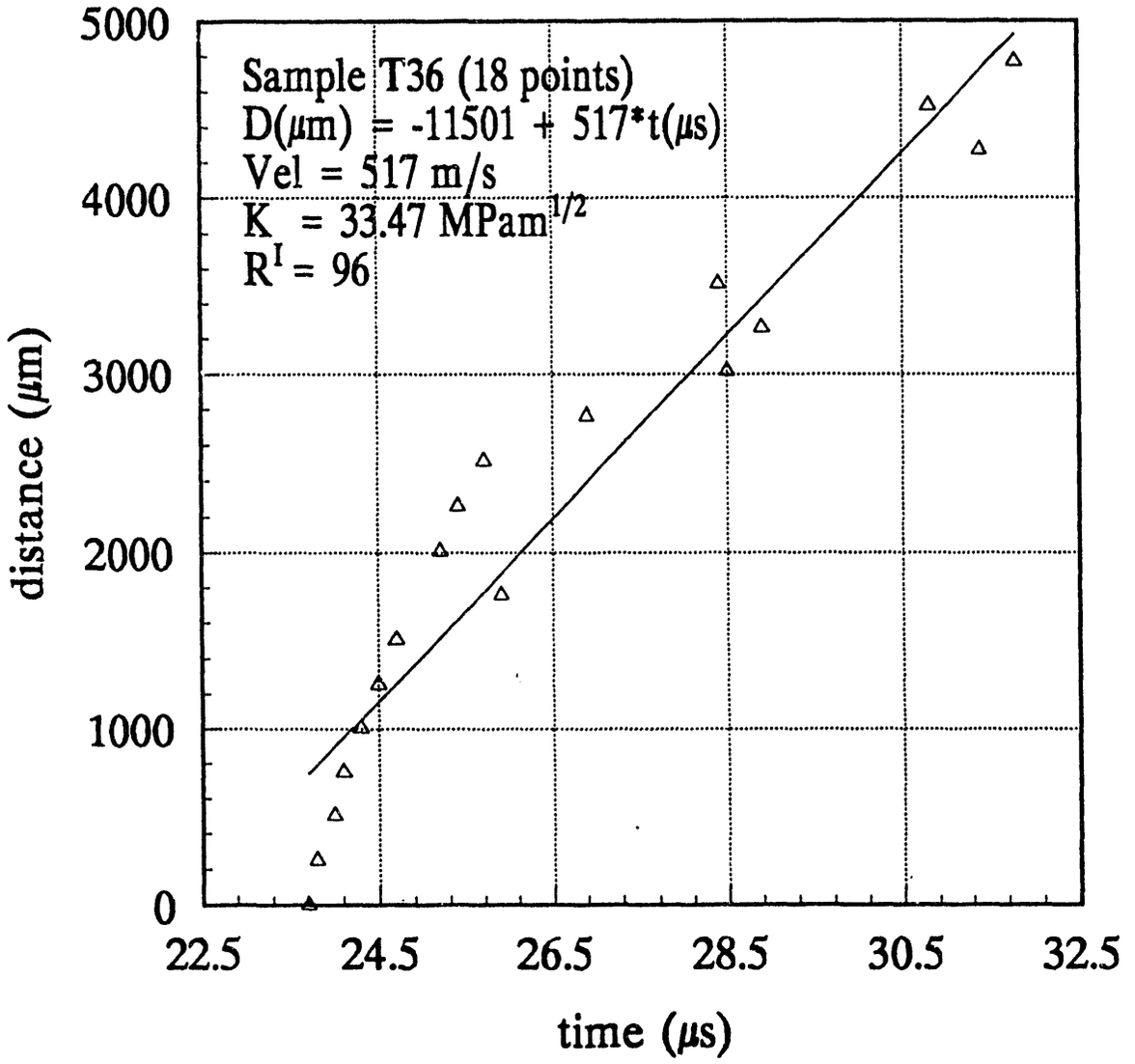
Sample T36 (18 points)
D(μm) = -11501 + 517*t(μs)
Vel = 517 m/s
K = 33.47 MPam^1/2
R^I = 96
5000
4000
3000
2000
1000
0
distance (μm)
22.5
24.5
26.5
28.5
30.5
32.5
time (μs)

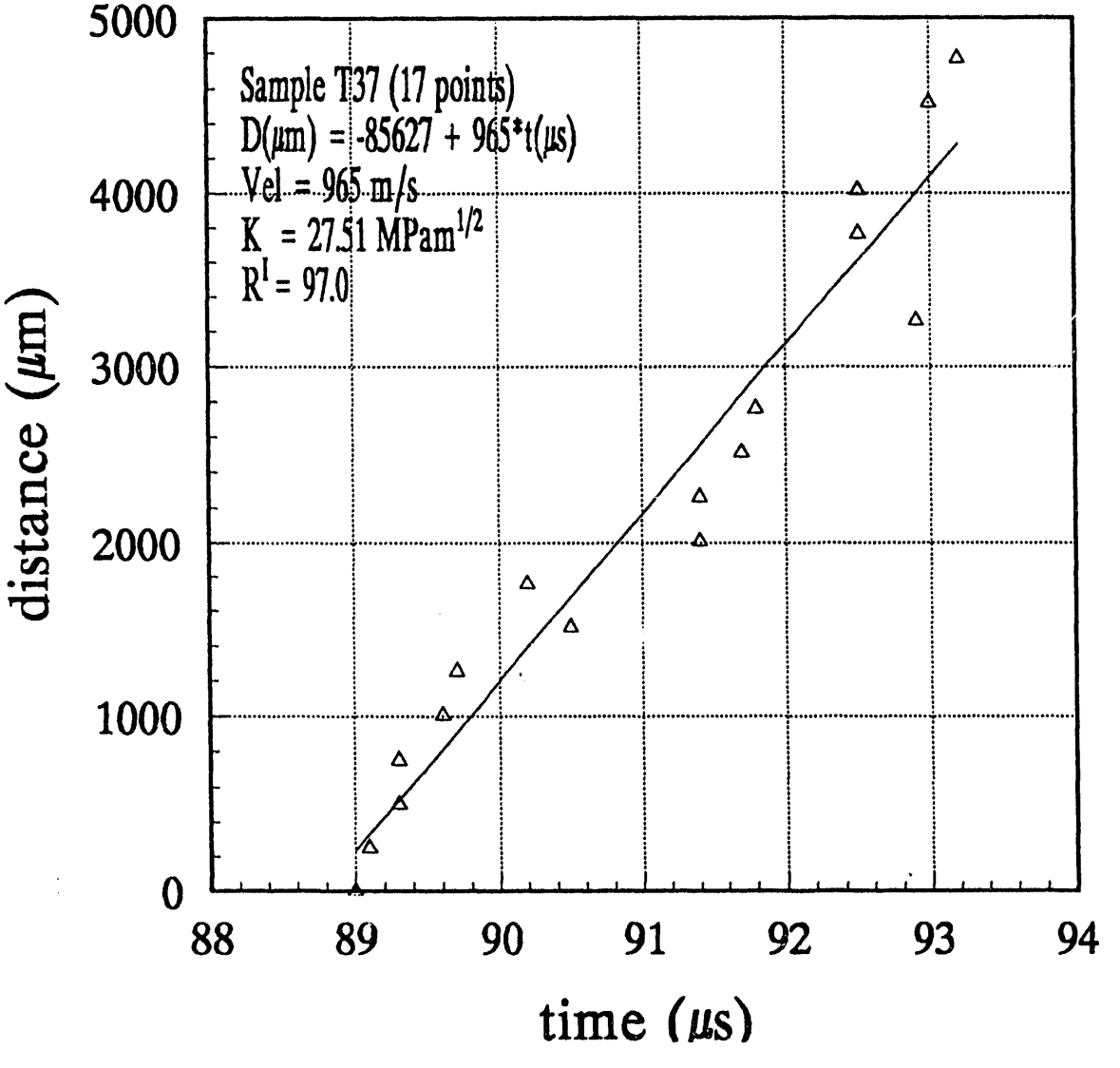
Sample T37 (17 points)
D(μm) = -85627 + 965*t(μs)
Vel = 965 m/s
K = 27.51 MPam^1/2
R^I = 97.0
distance (μm)
time (μs)
0
1000
2000
3000
4000
5000
88
89
90
91
92
93
94

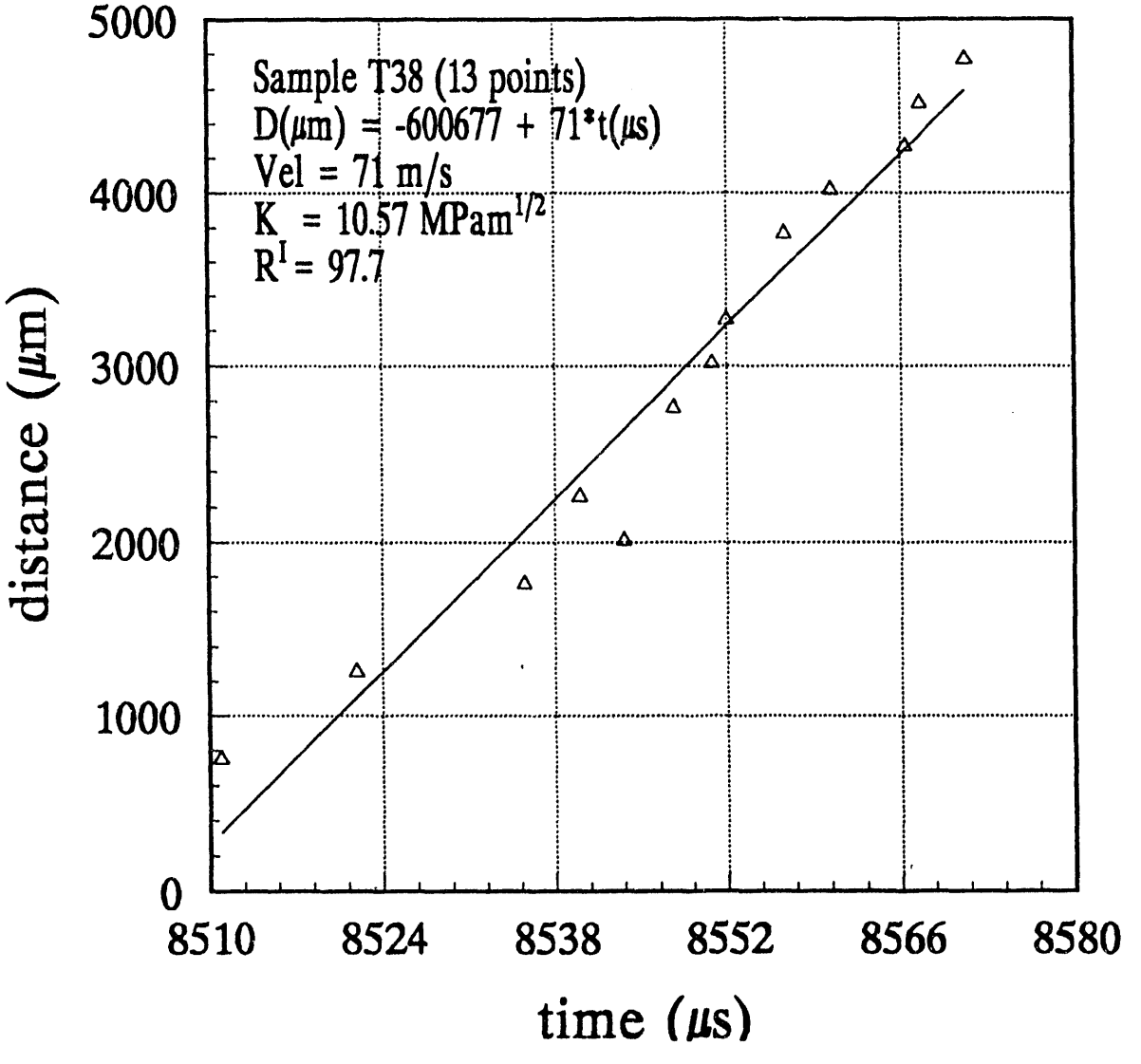
Sample T38 (13 points)
D(μm) = -600677 + 71*t(μs)
Vel = 71 m/s
K = 10.57 MPam^1/2
R^I = 97.7
5000
4000
3000
2000
1000
0
distance (μm)
8510
8524
8538
8552
8566
8580
time (μs)

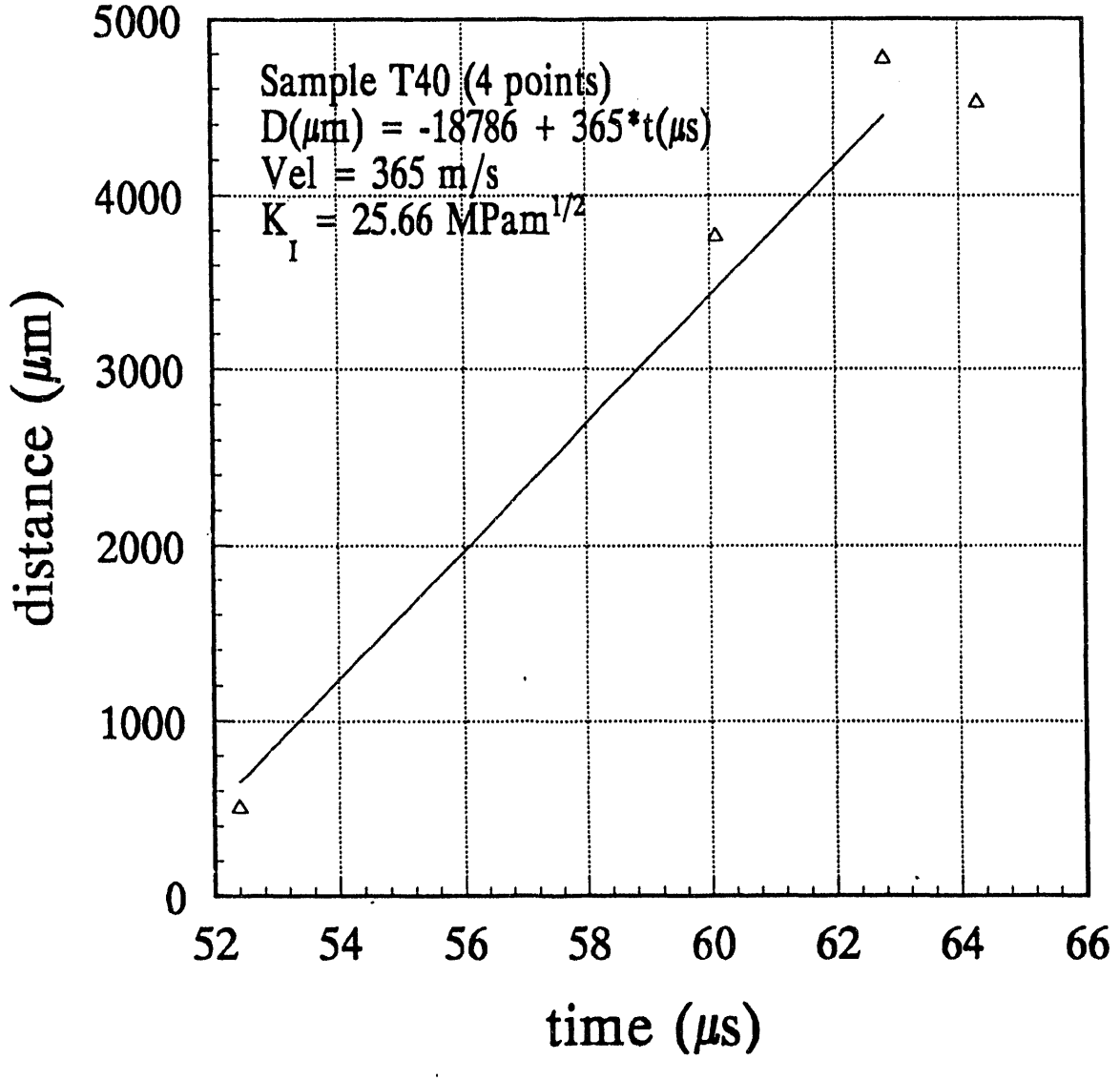
Sample T40 (4 points)
D(μm) = -18786 + 365*t(μs)
Vel = 365 m/s
K_I = 25.66 MPam^1/2
distance (μm)
time (μs)
0
1000
2000
3000
4000
5000
52
54
56
58
60
62
64
66

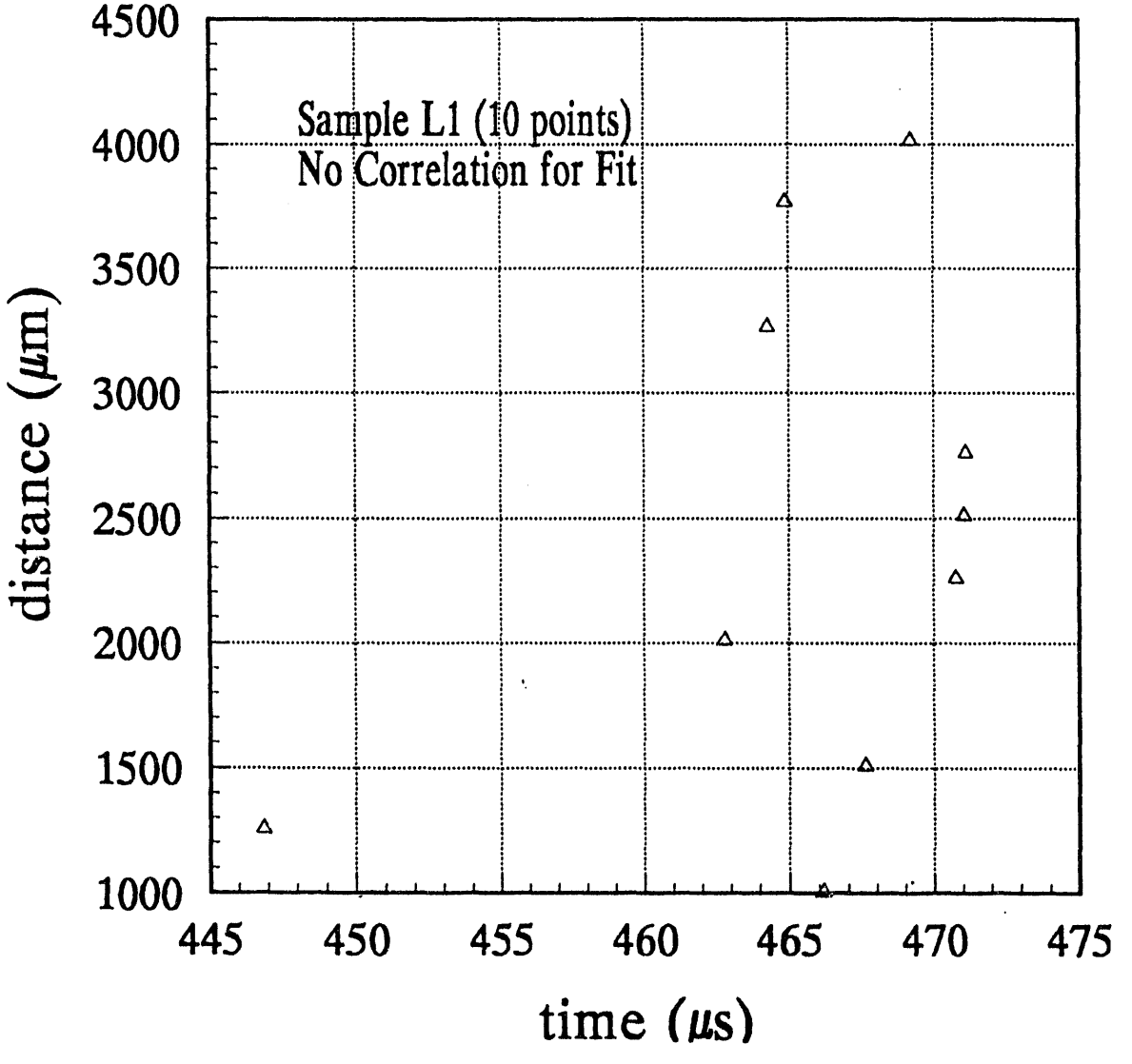
Sample L1 (10 points)
No Correlation for Fit
4500
4000
3500
3000
2500
2000
1500
1000
distance (μm)
445
450
455
460
465
470
475
time (μs)

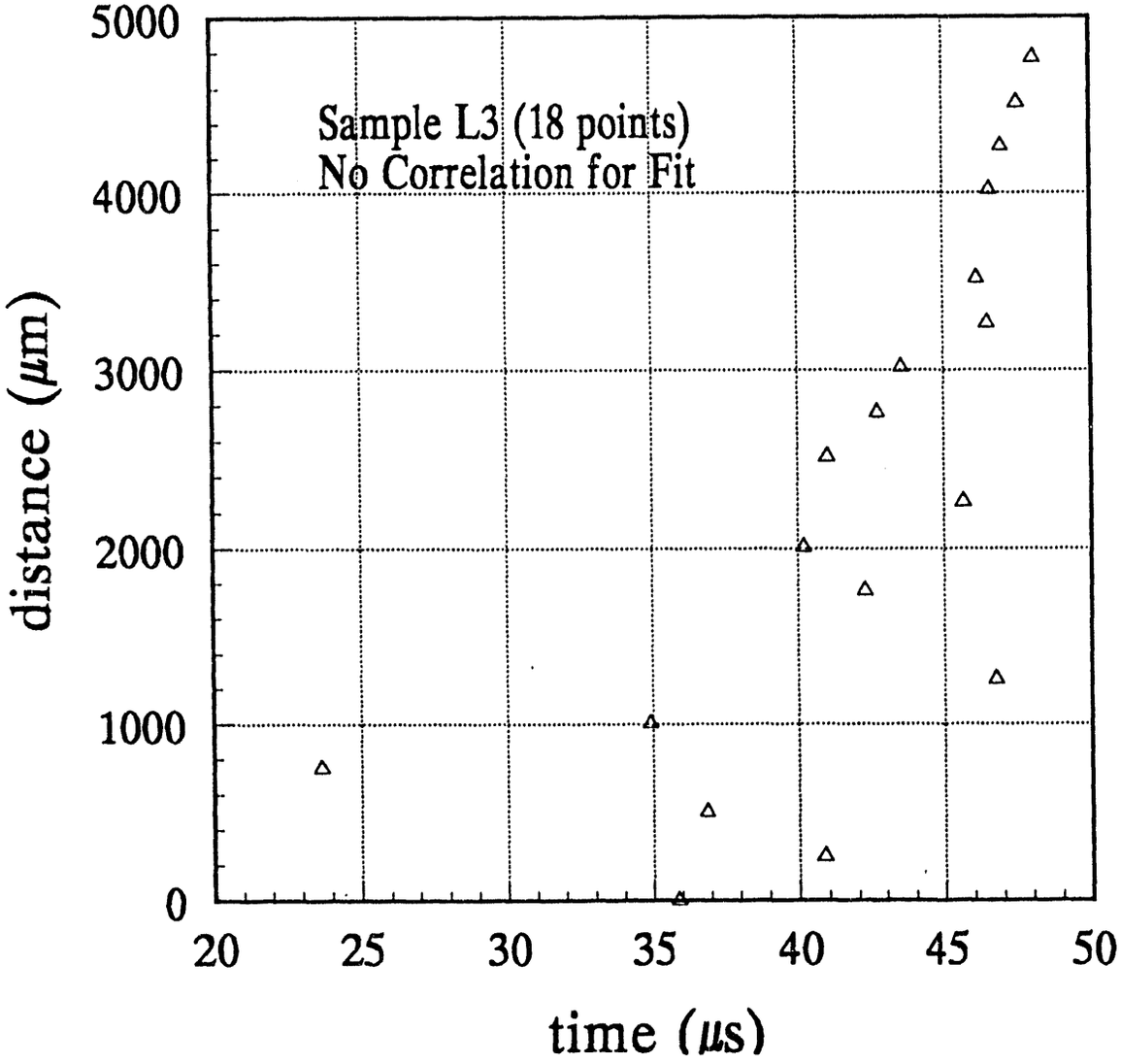
Sample L3 (18 points)
No Correlation for Fit
distance (μm)
5000
4000
3000
2000
1000
0
20
25
30
35
40
45
50
time (μs)

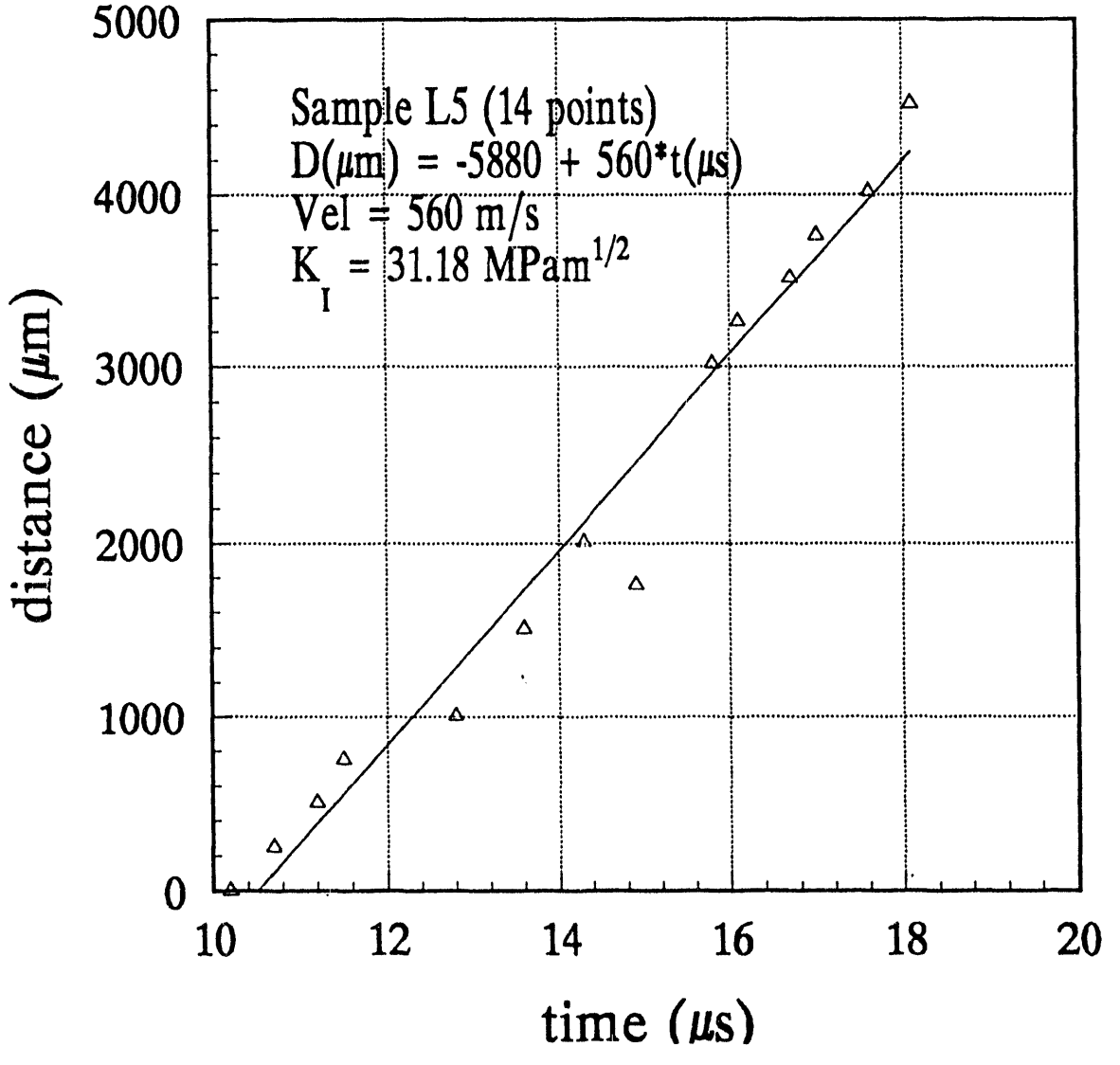
Sample L5 (14 points)
D(μm) = -5880 + 560*t(μs)
Vel = 560 m/s
K_I = 31.18 MPam^1/2
distance (μm)
time (μs)
5000
4000
3000
2000
1000
0
10
12
14
16
18
20

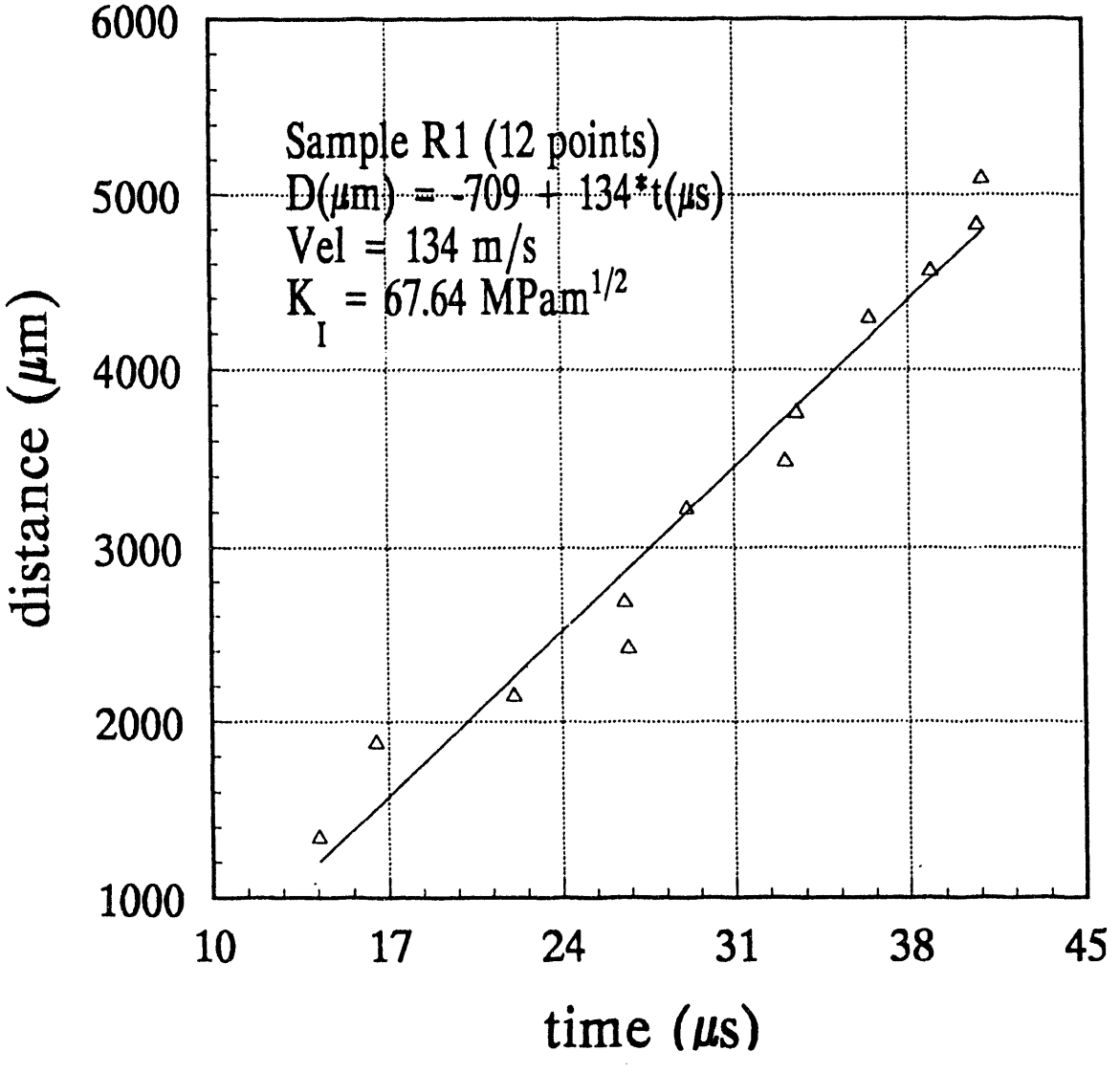
Sample R1 (12 points)
D(μm) = -709 + 134*t(μs)
Vel = 134 m/s
K_I = 67.64 MPam^1/2
distance (μm)
time (μs)
6000
5000
4000
3000
2000
1000
10
17
24
31
38
45

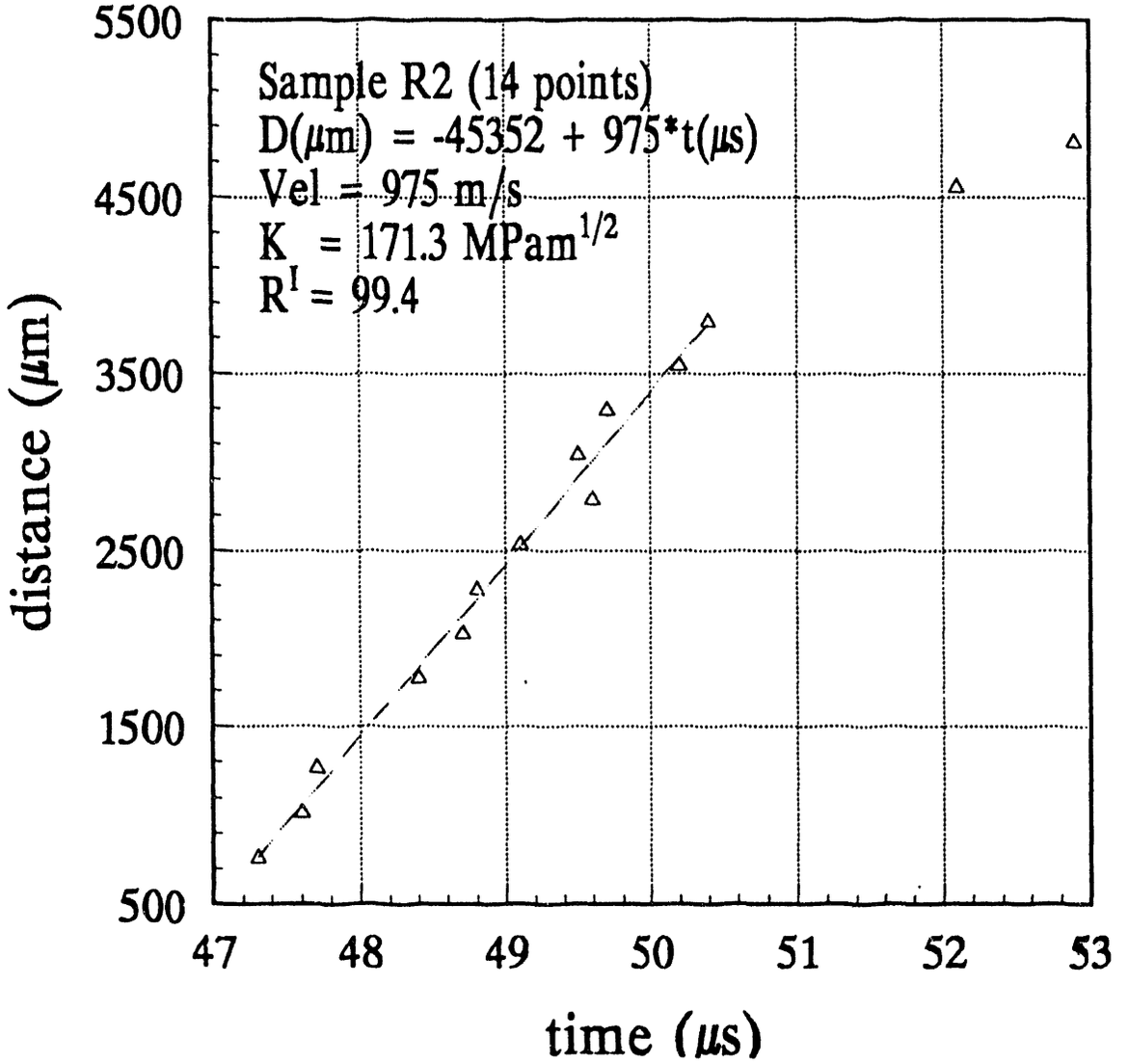
Sample R2 (14 points)
D(μm) = -45352 + 975*t(μs)
Vel = 975 m/s
K = 171.3 MPam^1/2
R^I = 99.4
5500
4500
3500
2500
1500
500
distance (μm)
47
48
49
50
51
52
53
time (μs)

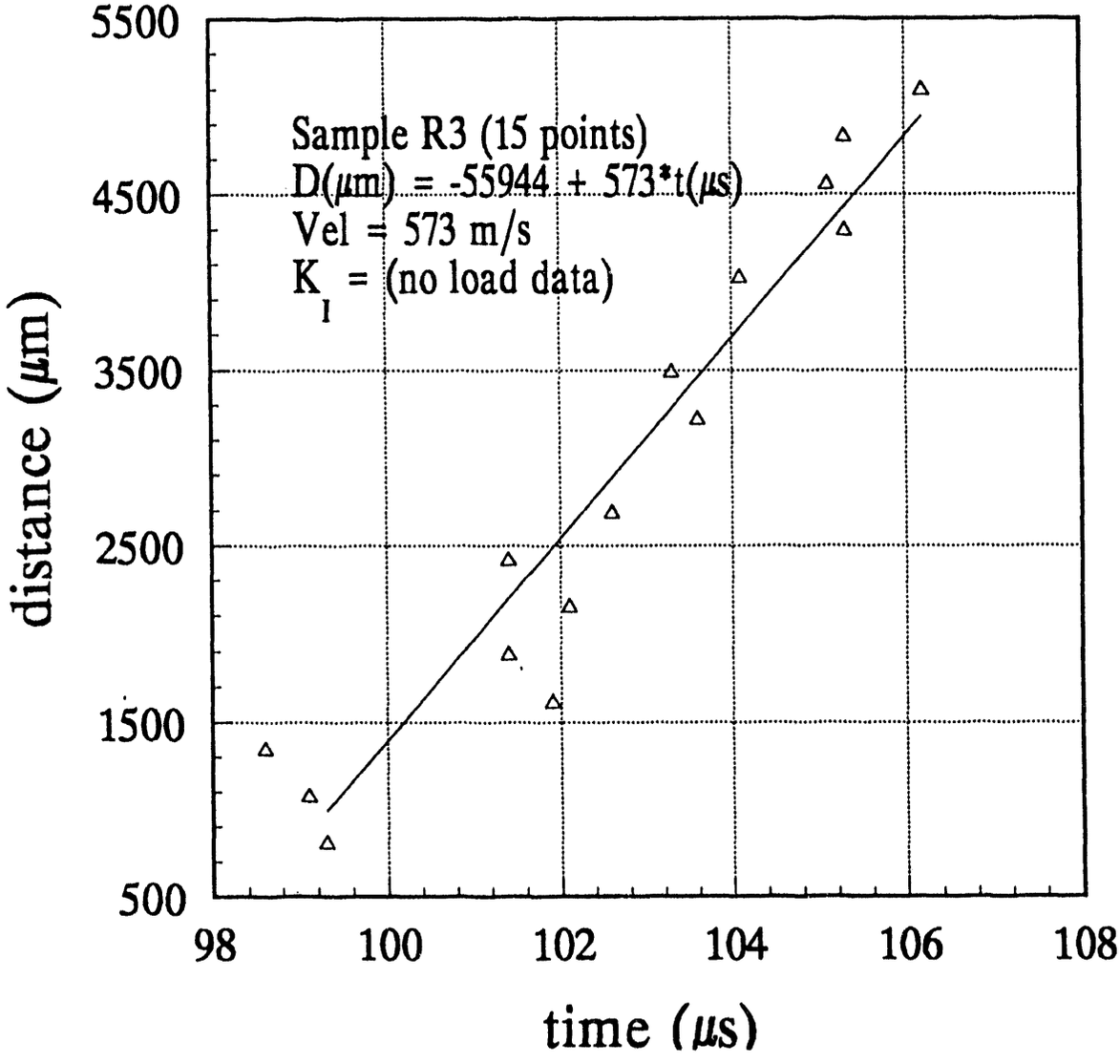
Sample R3 (15 points)
D(μm) = -55944 + 573*t(μs)
Vel = 573 m/s
K_I = (no load data)
distance (μm)
time (μs)
5500
4500
3500
2500
1500
500
98
100
102
104
106
108

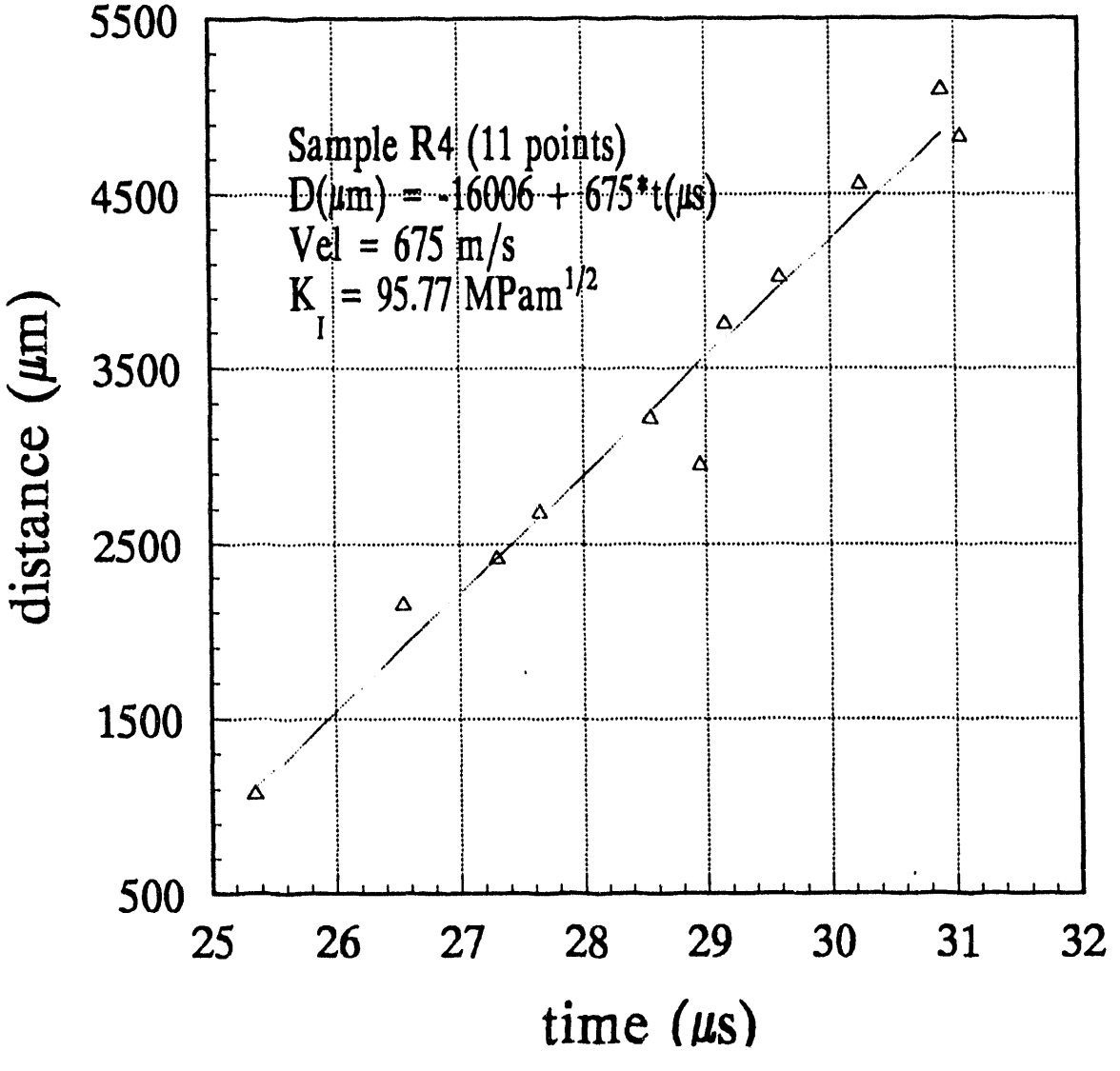
Sample R4 (11 points)
D(μm) = -16006 + 675*t(μs)
Vel = 675 m/s
K_I = 95.77 MPam^1/2
distance (μm)
time (μs)
5500
4500
3500
2500
1500
500
25
26
27
28
29
30
31
32

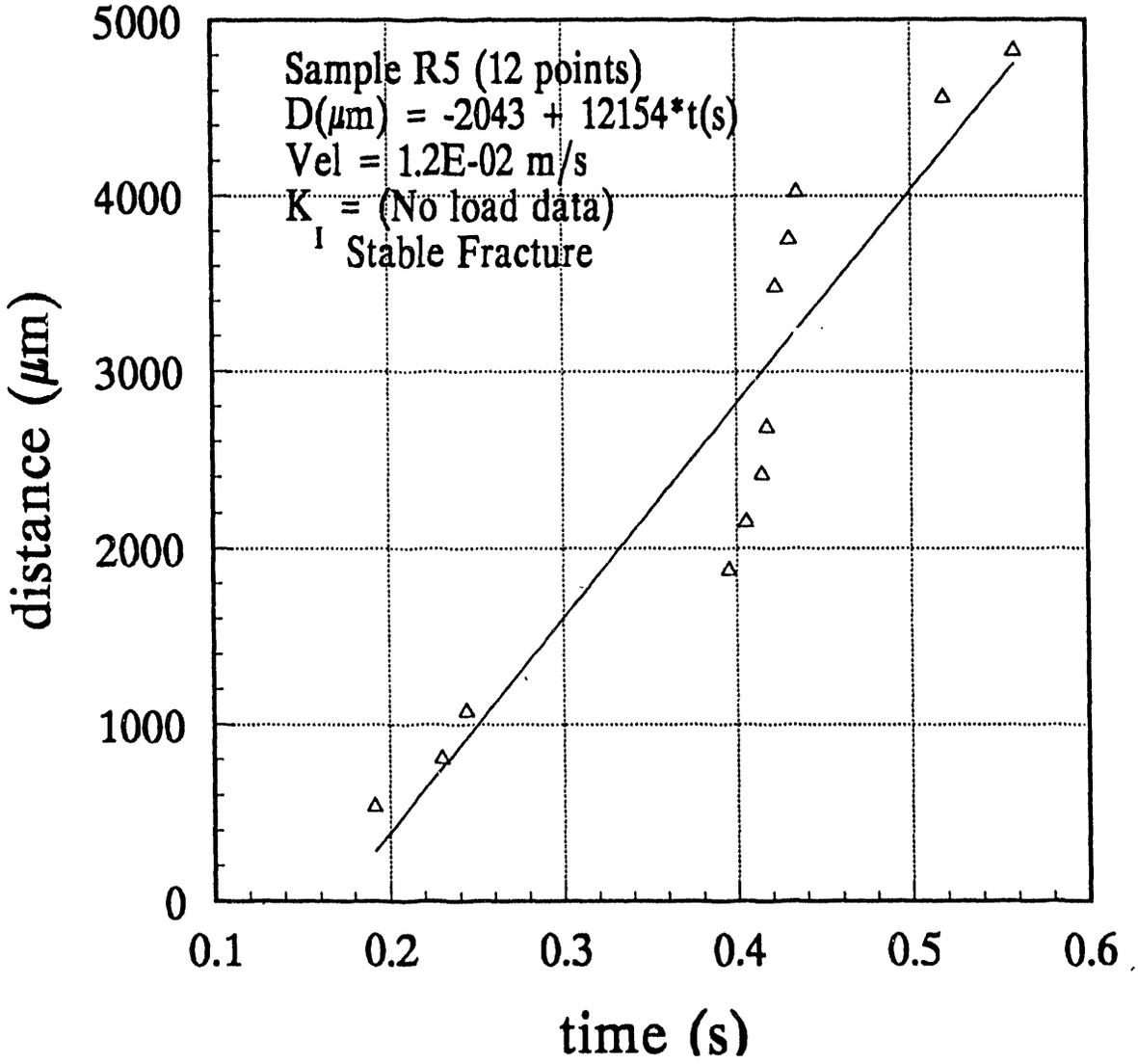
Sample R5 (12 points)
D(μm) = -2043 + 12154*t(s)
Vel = 1.2E-02 m/s
K_I = (No load data)
Stable Fracture
distance (μm)
time (s)
5000
4000
3000
2000
1000
0
0.1
0.2
0.3
0.4
0.5
0.6

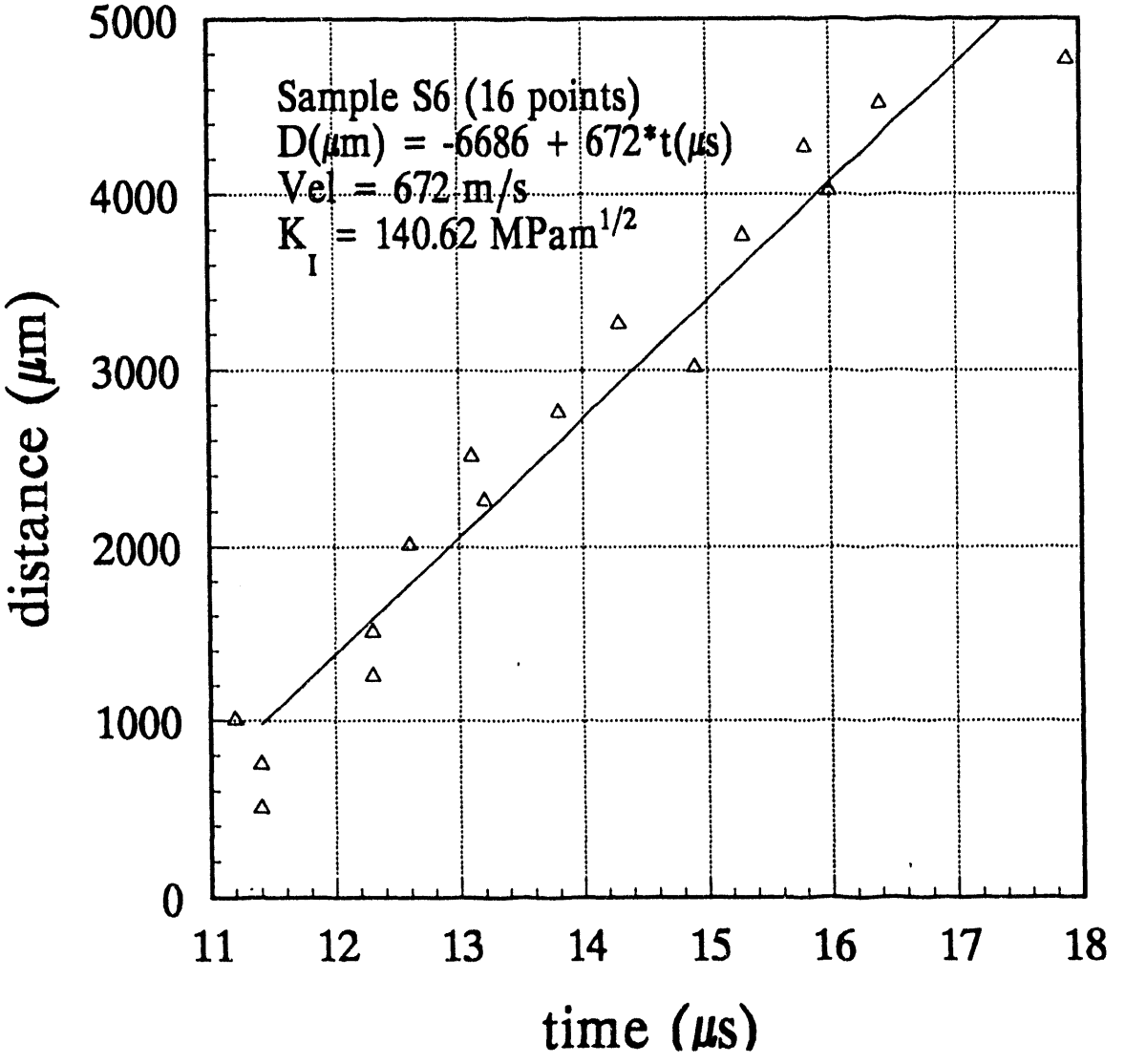
Sample S6 (16 points)
D(μm) = -6686 + 672*t(μs)
Vel = 672 m/s
K_I = 140.62 MPam^1/2
distance (μm)
time (μs)
0
1000
2000
3000
4000
5000
11
12
13
14
15
16
17
18

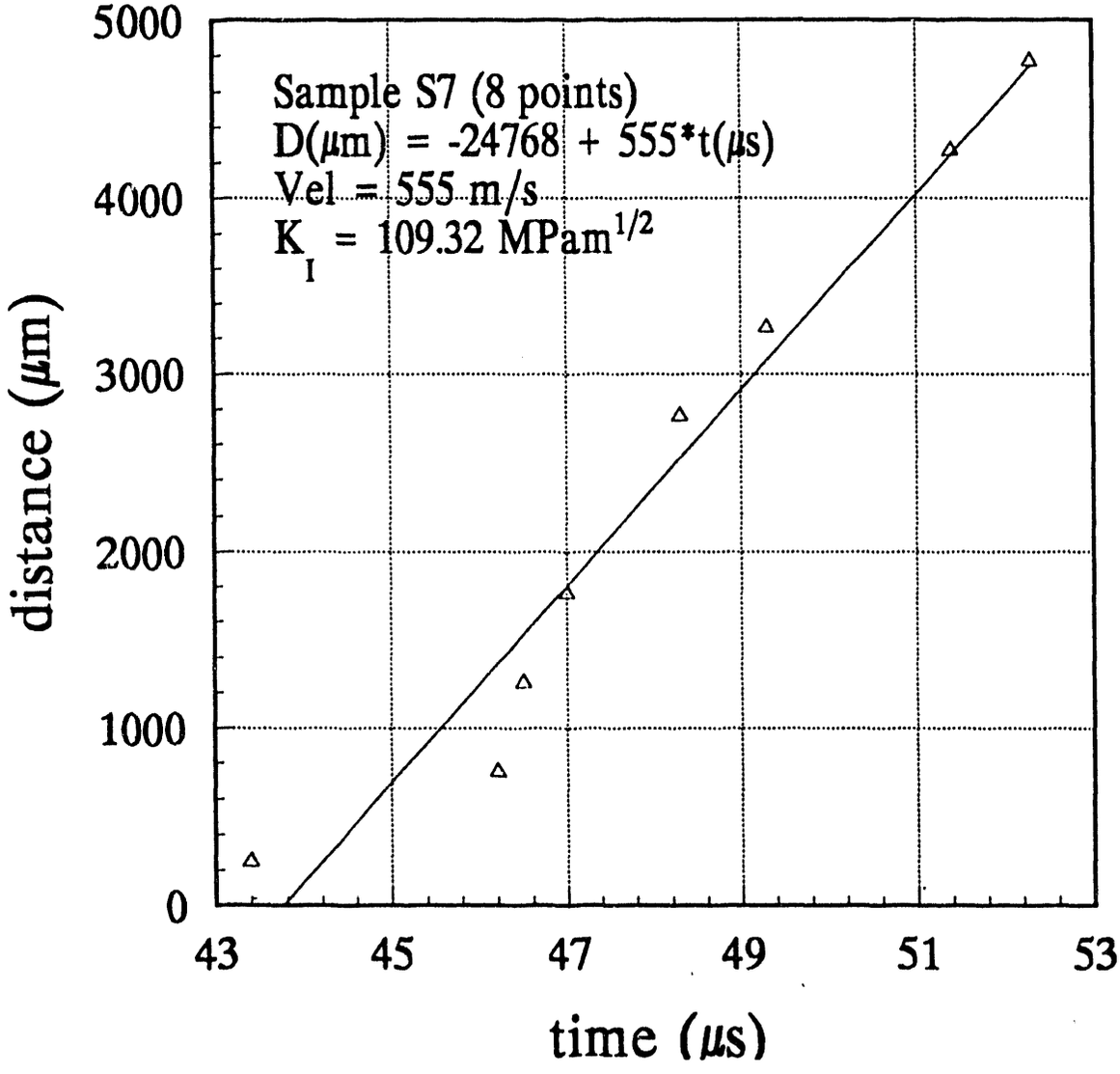
Sample S7 (8 points)
D(μm) = -24768 + 555*t(μs)
Vel = 555 m/s
K_I = 109.32 MPam^1/2
distance (μm)
time (μs)
5000
4000
3000
2000
1000
0
43
45
47
49
51
53

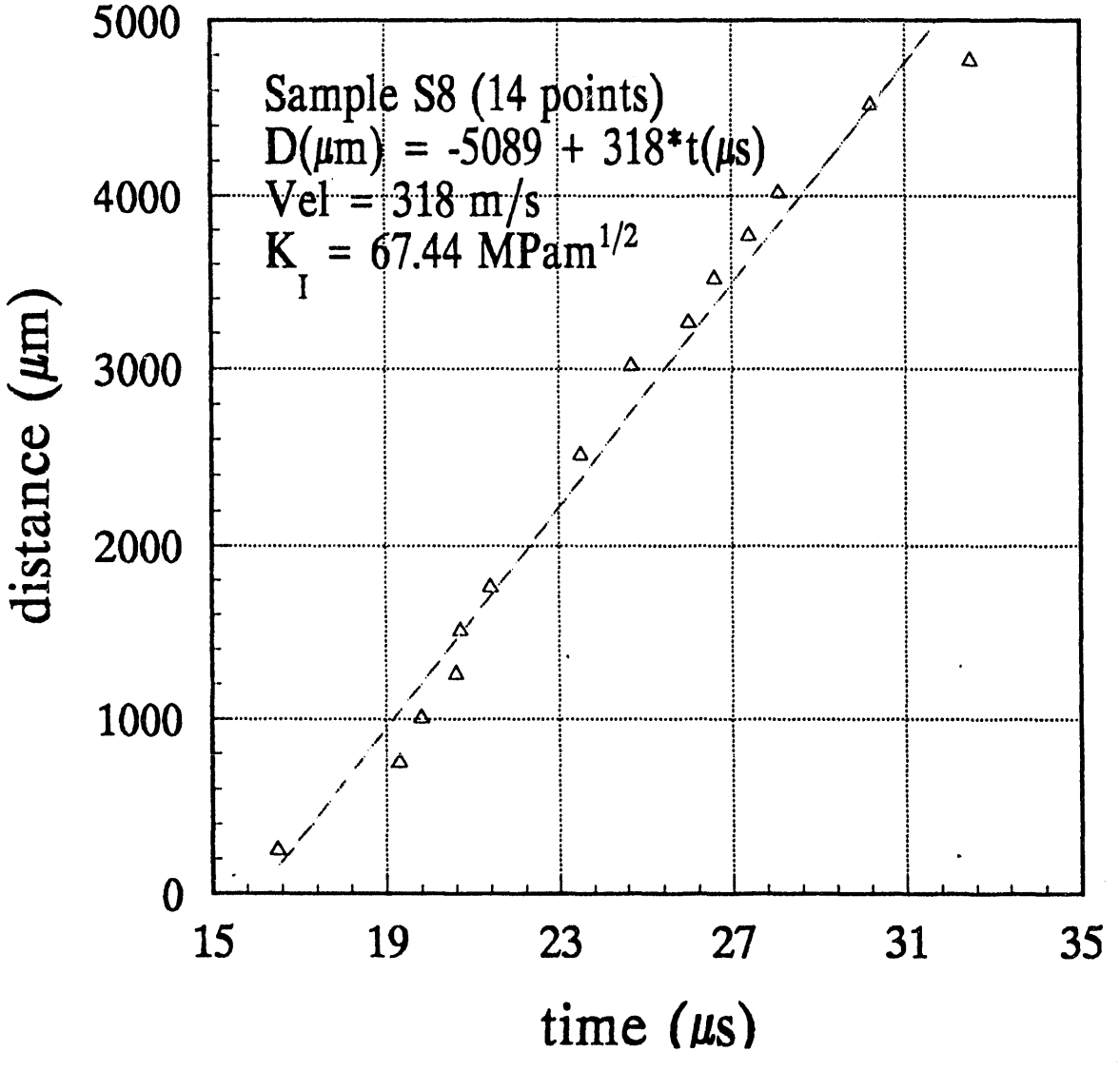
Sample S8 (14 points)
D(μm) = -5089 + 318*t(μs)
Vel = 318 m/s
K_I = 67.44 MPam^1/2
distance (μm)
time (μs)
5000
4000
3000
2000
1000
0
15
19
23
27
31
35

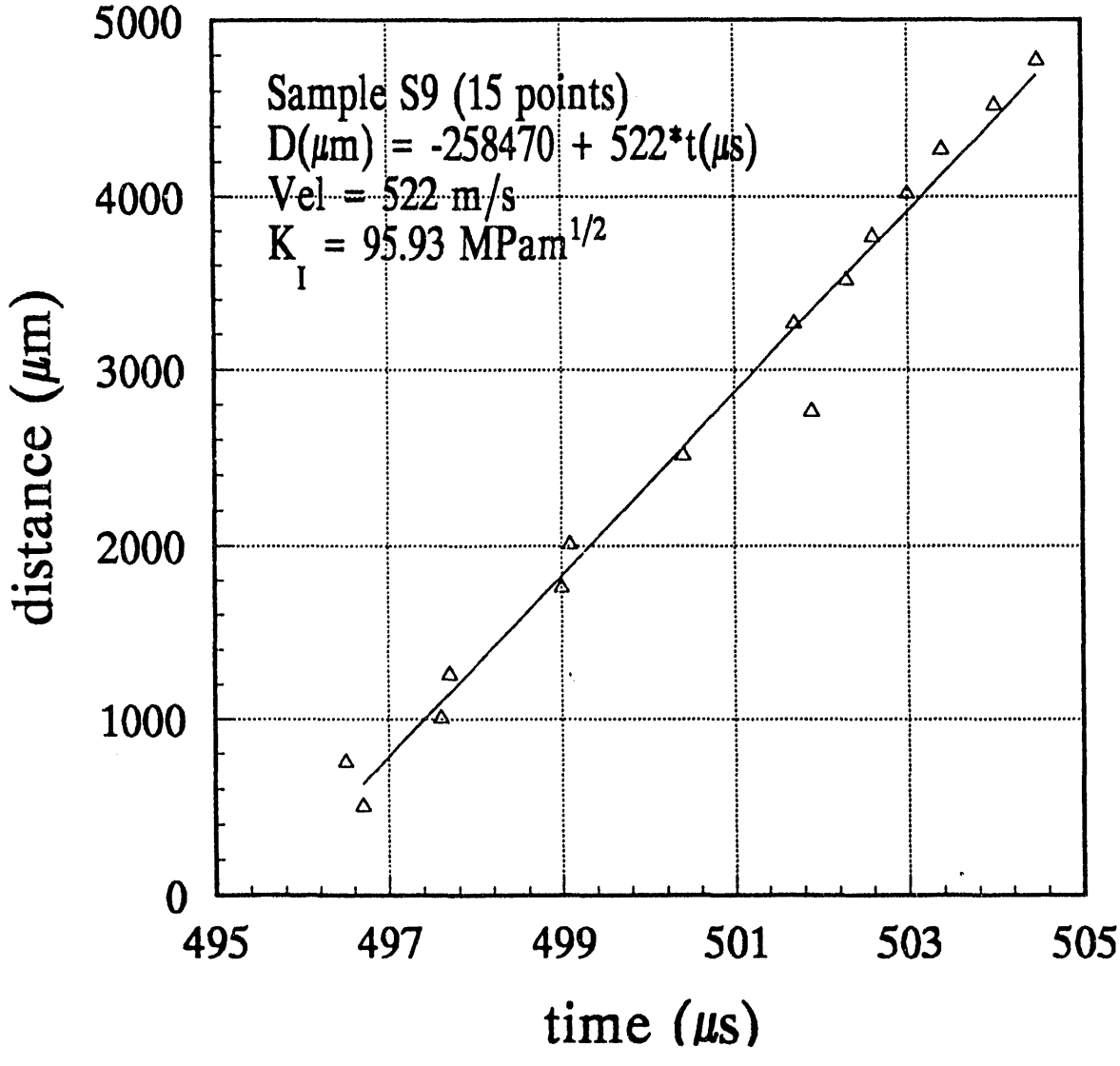
Sample S9 (15 points)
D(μm) = -258470 + 522*t(μs)
Vel = 522 m/s
K_I = 95.93 MPam^1/2
distance (μm)
time (μs)
0
1000
2000
3000
4000
5000
495
497
499
501
503
505

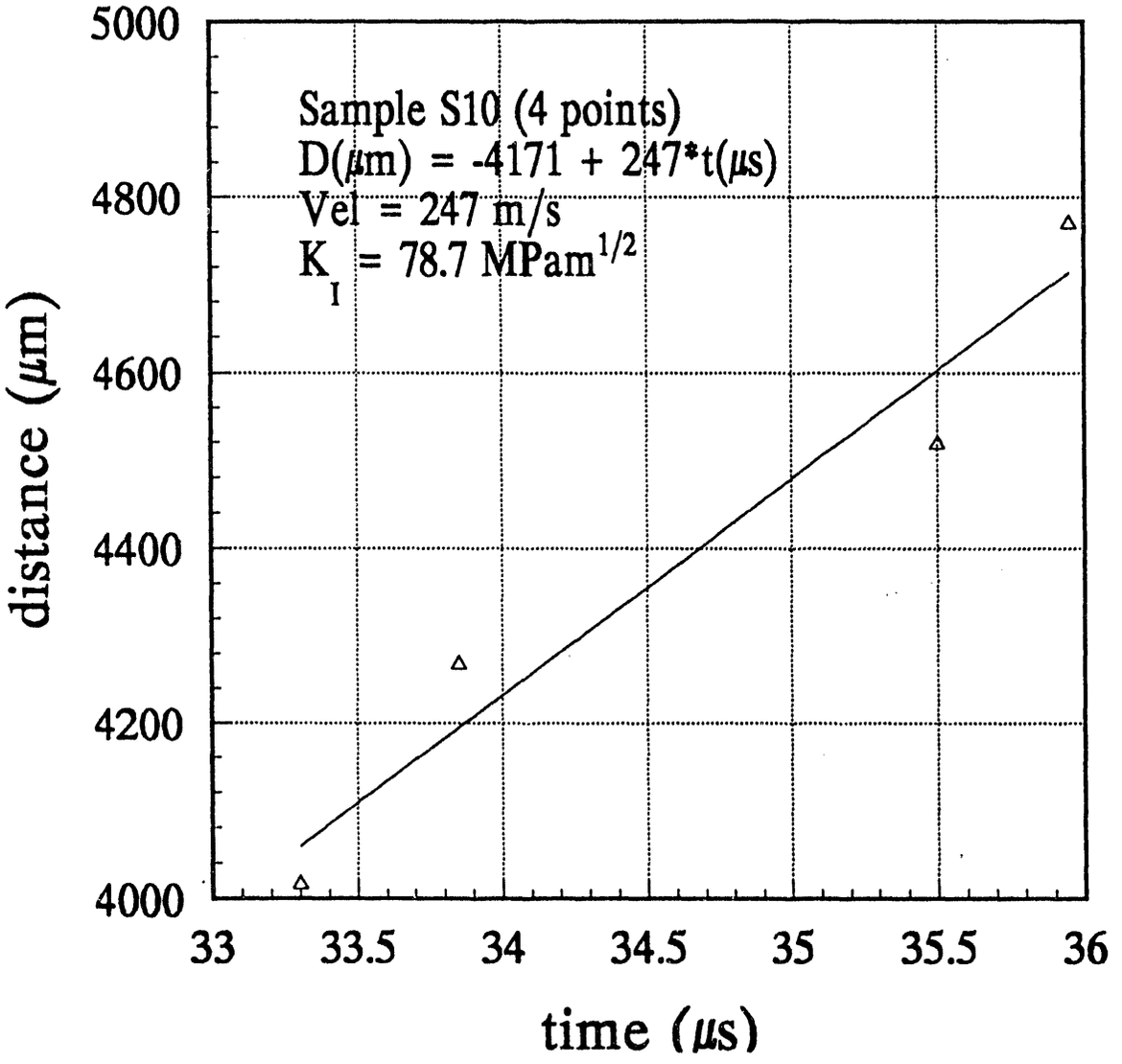
Sample S10 (4 points)
D(μm) = -4171 + 247*t(μs)
Vel = 247 m/s
K_I = 78.7 MPam^1/2
5000
4800
4600
4400
4200
4000
distance (μm)
33
33.5
34
34.5
35
35.5
36
time (μs)

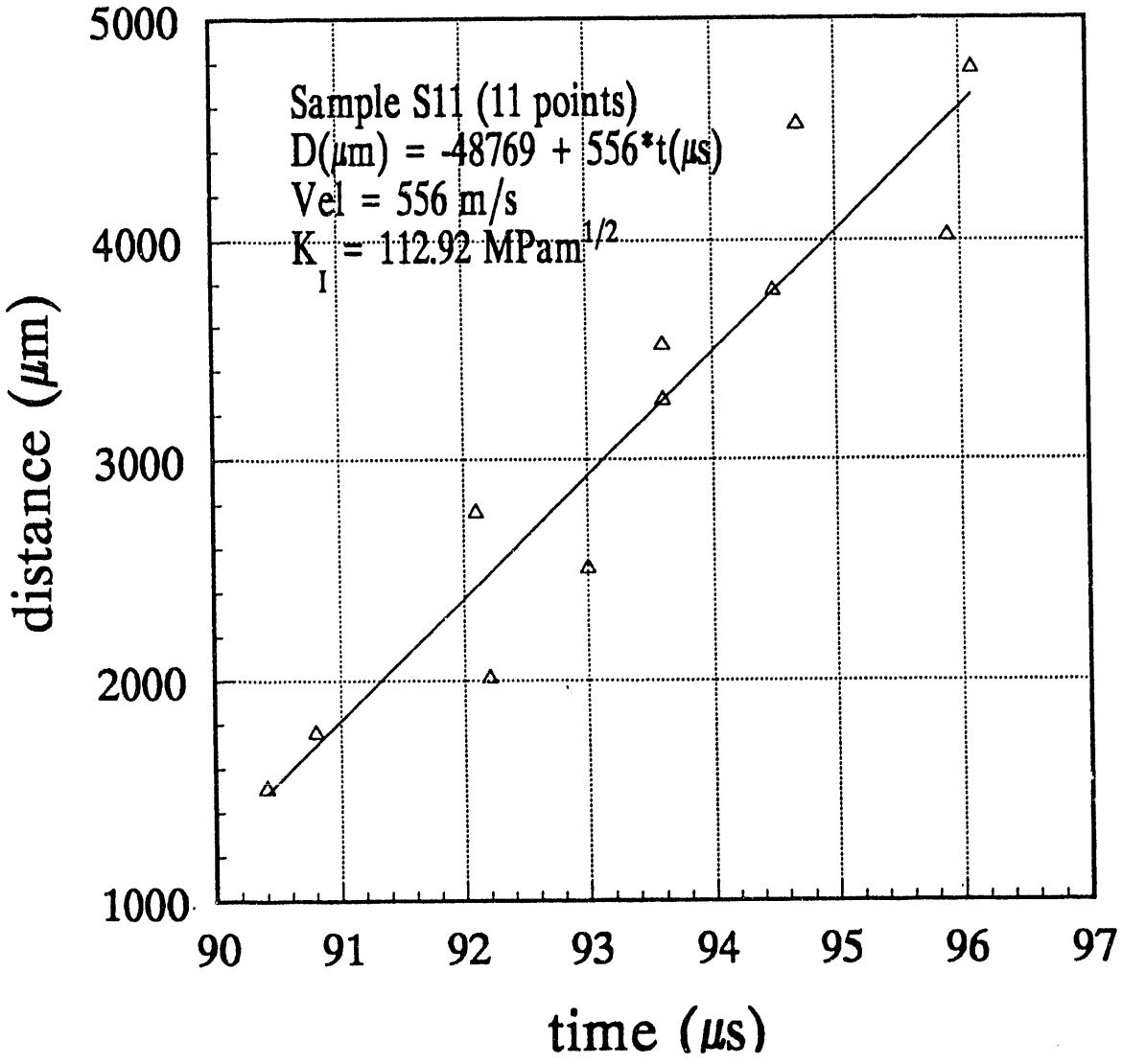
Sample S11 (11 points)
D(μm) = -48769 + 556*t(μs)
Vel = 556 m/s
K_I = 112.92 MPam^1/2
distance (μm)
time (μs)
5000
4000
3000
2000
1000
90
91
92
93
94
95
96
97

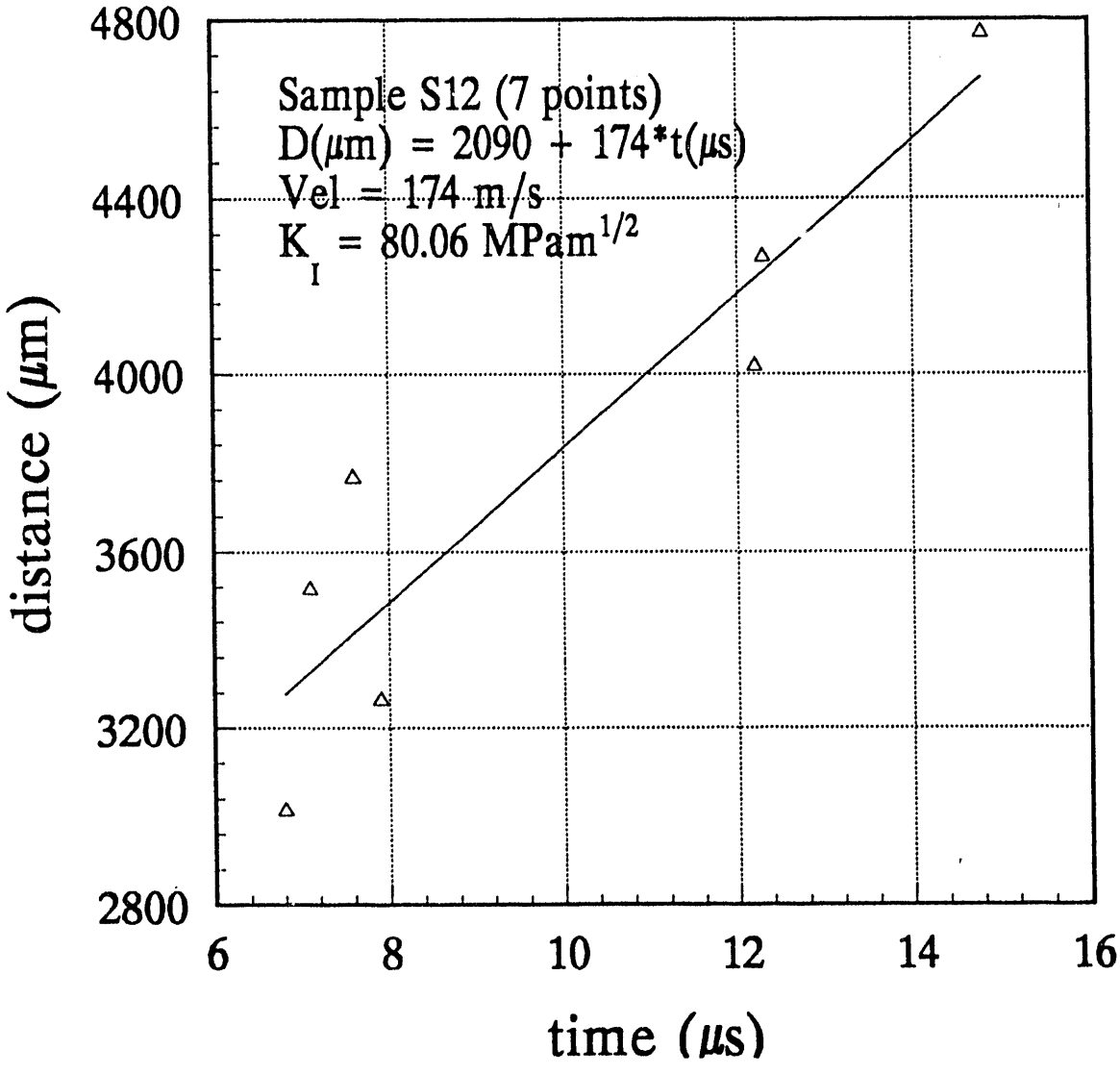
Sample S12 (7 points)
D(μm) = 2090 + 174*t(μs)
Vel = 174 m/s
K_I = 80.06 MPam^1/2
distance (μm)
time (μs)
4800
4400
4000
3600
3200
2800
6
8
10
12
14
16

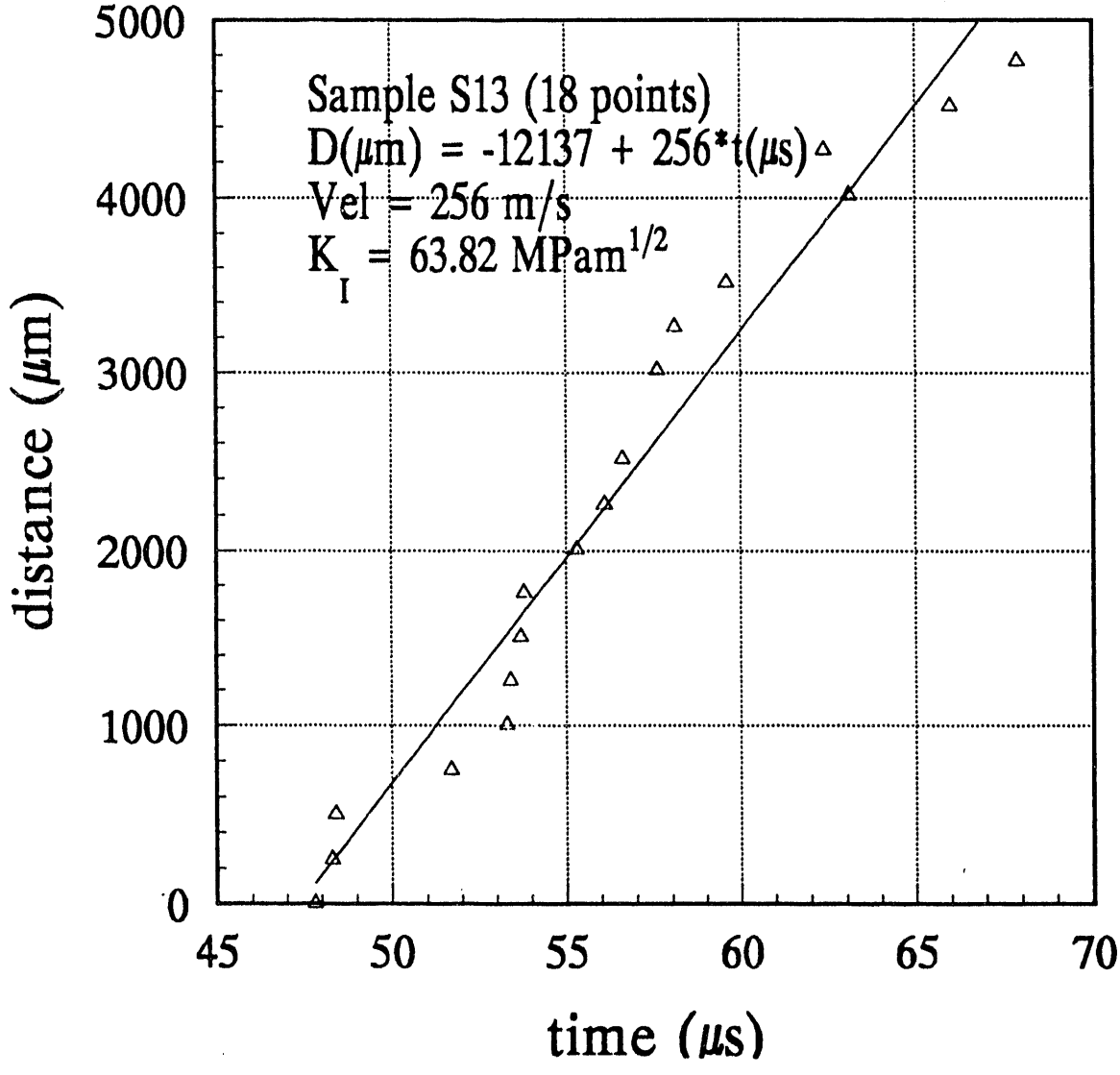
Sample S13 (18 points)
D(μm) = -12137 + 256*t(μs)
Vel = 256 m/s
K_I = 63.82 MPam^1/2
distance (μm)
time (μs)
5000
4000
3000
2000
1000
0
45
50
55
60
65
70

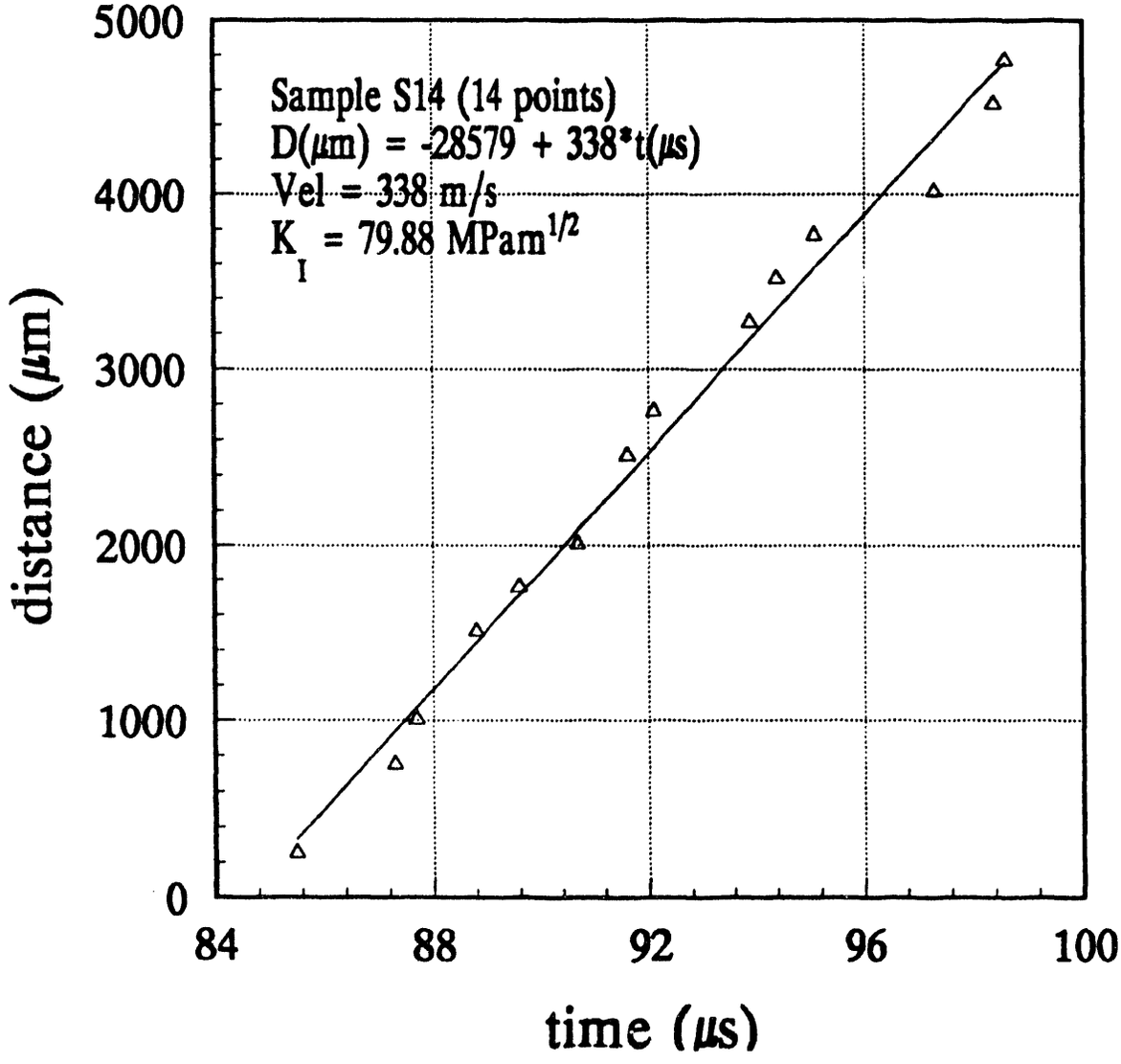
Sample S14 (14 points)
D(μm) = -28579 + 338*t(μs)
Vel = 338 m/s
K_I = 79.88 MPam^1/2
distance (μm)
time (μs)
0
1000
2000
3000
4000
5000
84
88
92
96
100

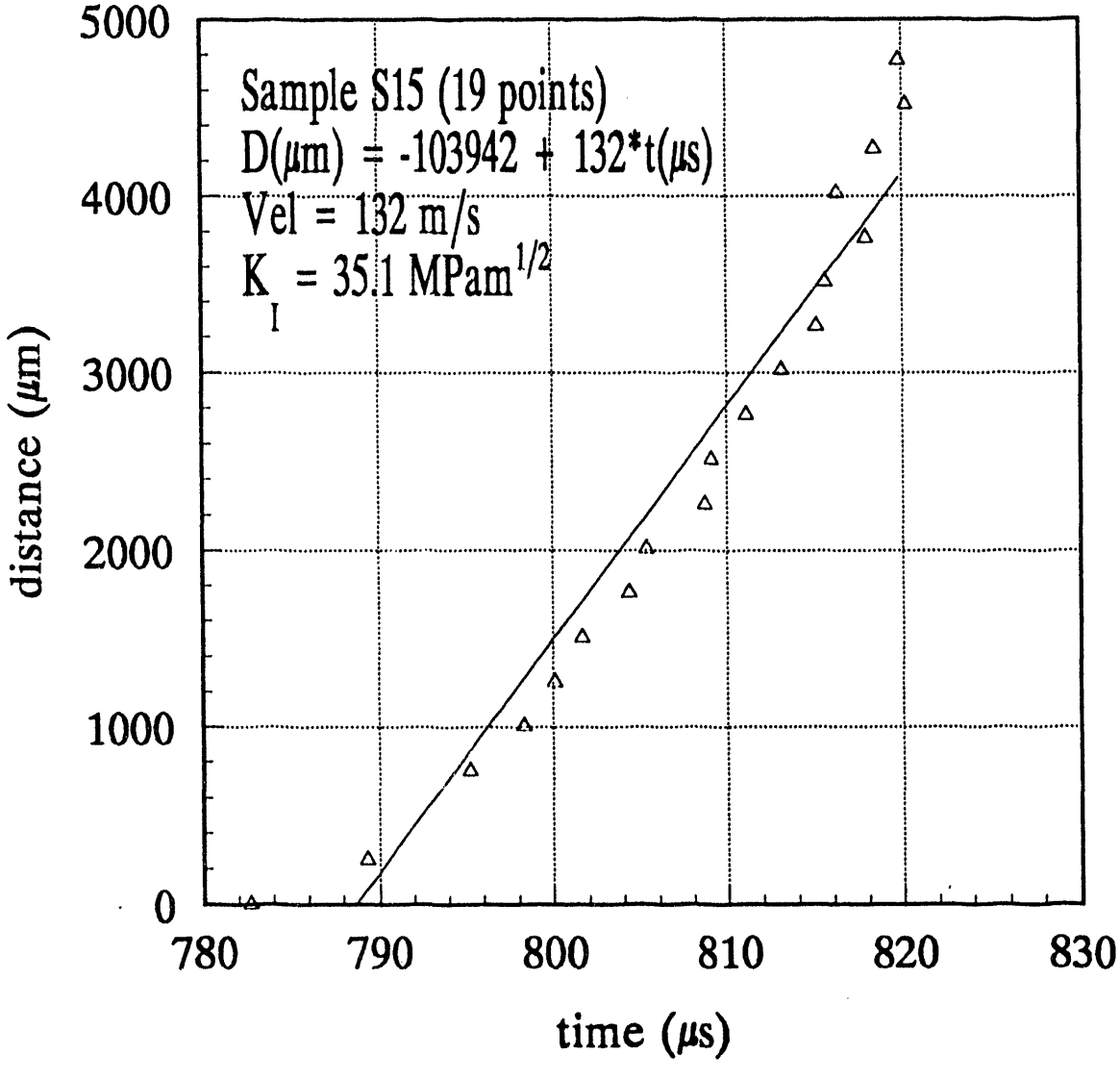
Sample S15 (19 points)
D(μm) = -103942 + 132*t(μs)
Vel = 132 m/s
K_I = 35.1 MPam^1/2
distance (μm)
time (μs)
0
1000
2000
3000
4000
5000
780
790
800
810
820
830

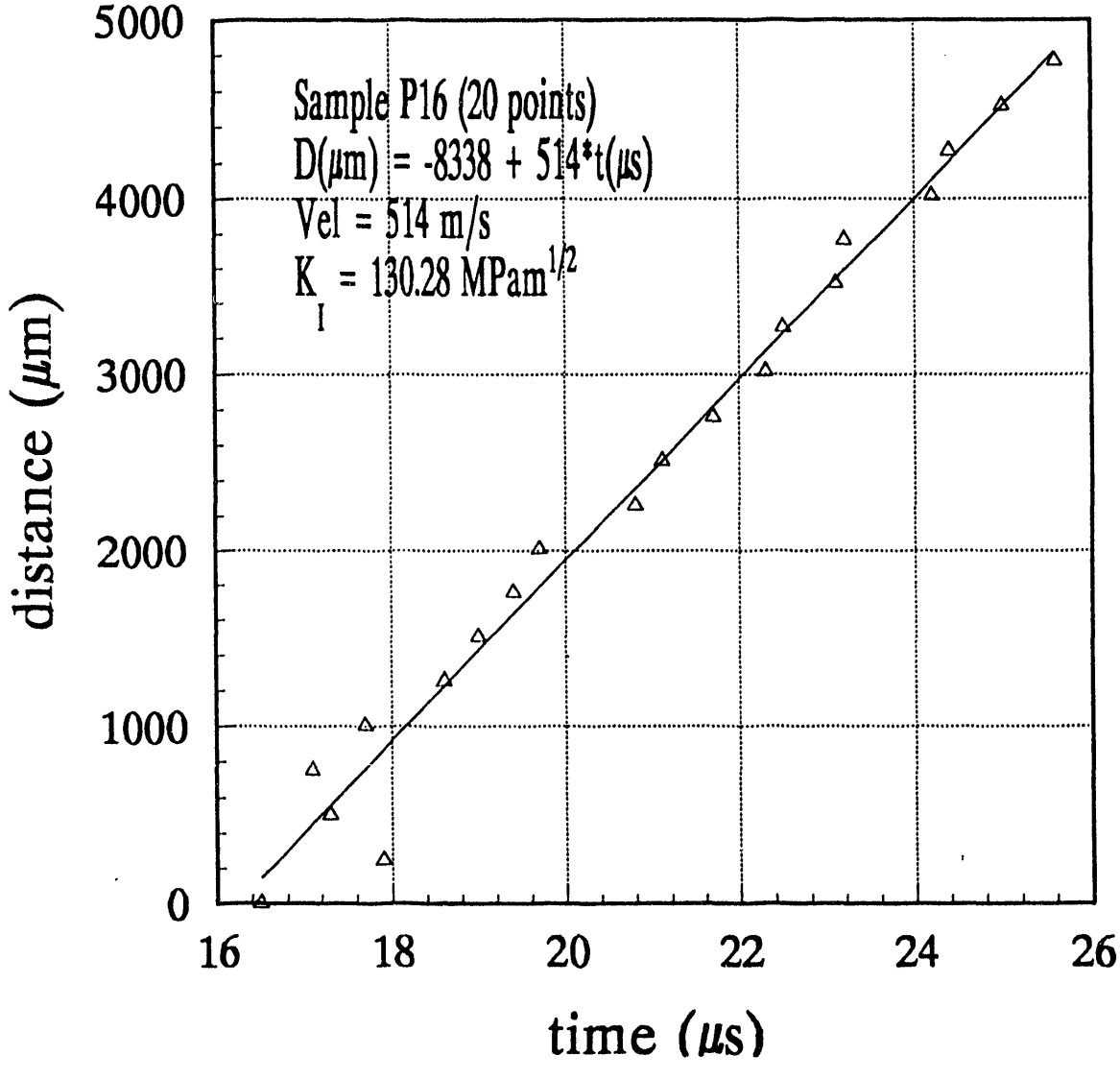
Sample P16 (20 points)
D(μm) = -8338 + 514*t(μs)
Vel = 514 m/s
K_I = 130.28 MPam^1/2
distance (μm)
time (μs)
0
1000
2000
3000
4000
5000
16
18
20
22
24
26

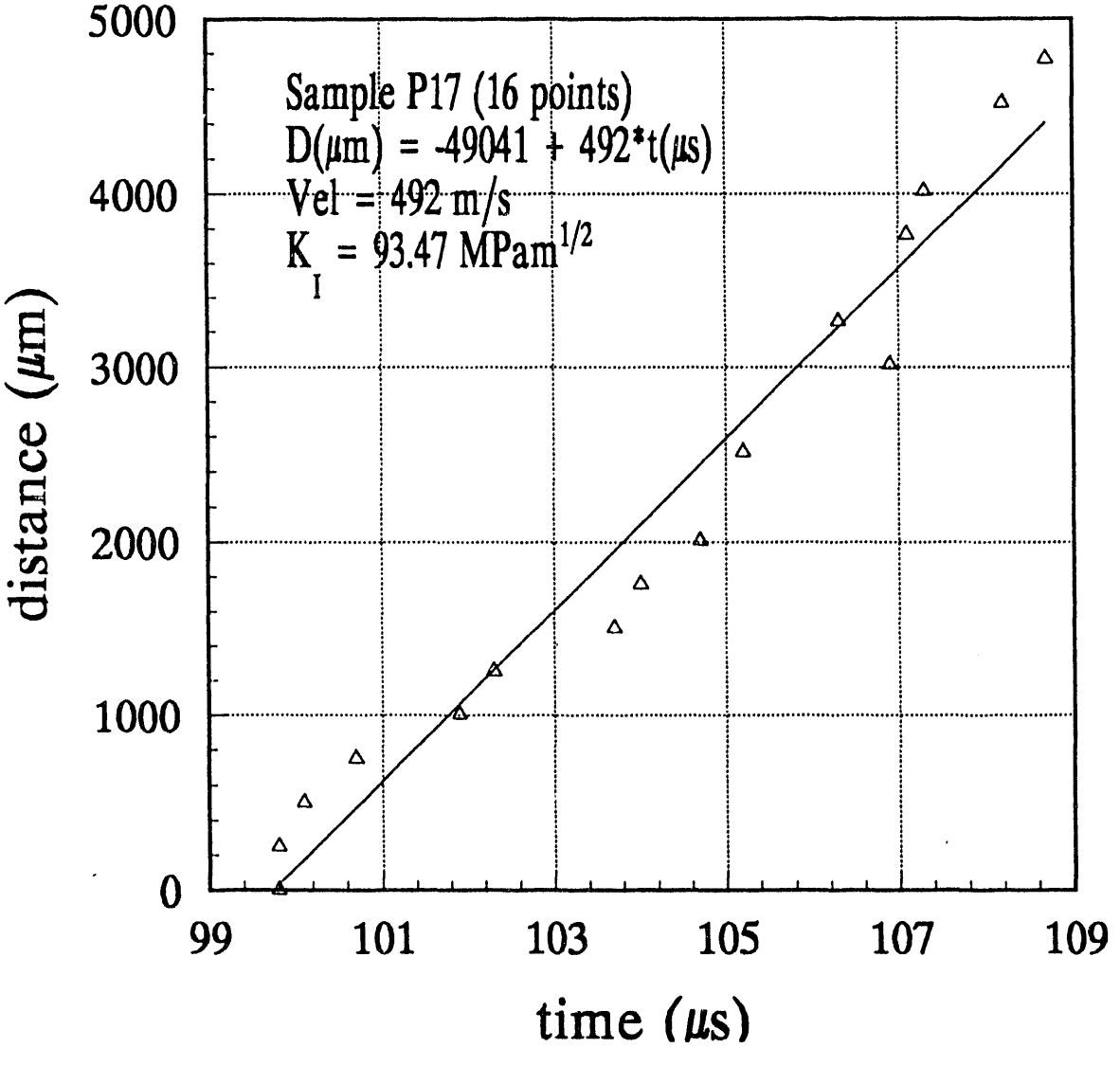
Sample P17 (16 points)
D(μm) = -49041 + 492*t(μs)
Vel = 492 m/s
K_I = 93.47 MPam^1/2
distance (μm)
time (μs)
5000
4000
3000
2000
1000
0
99
101
103
105
107
109

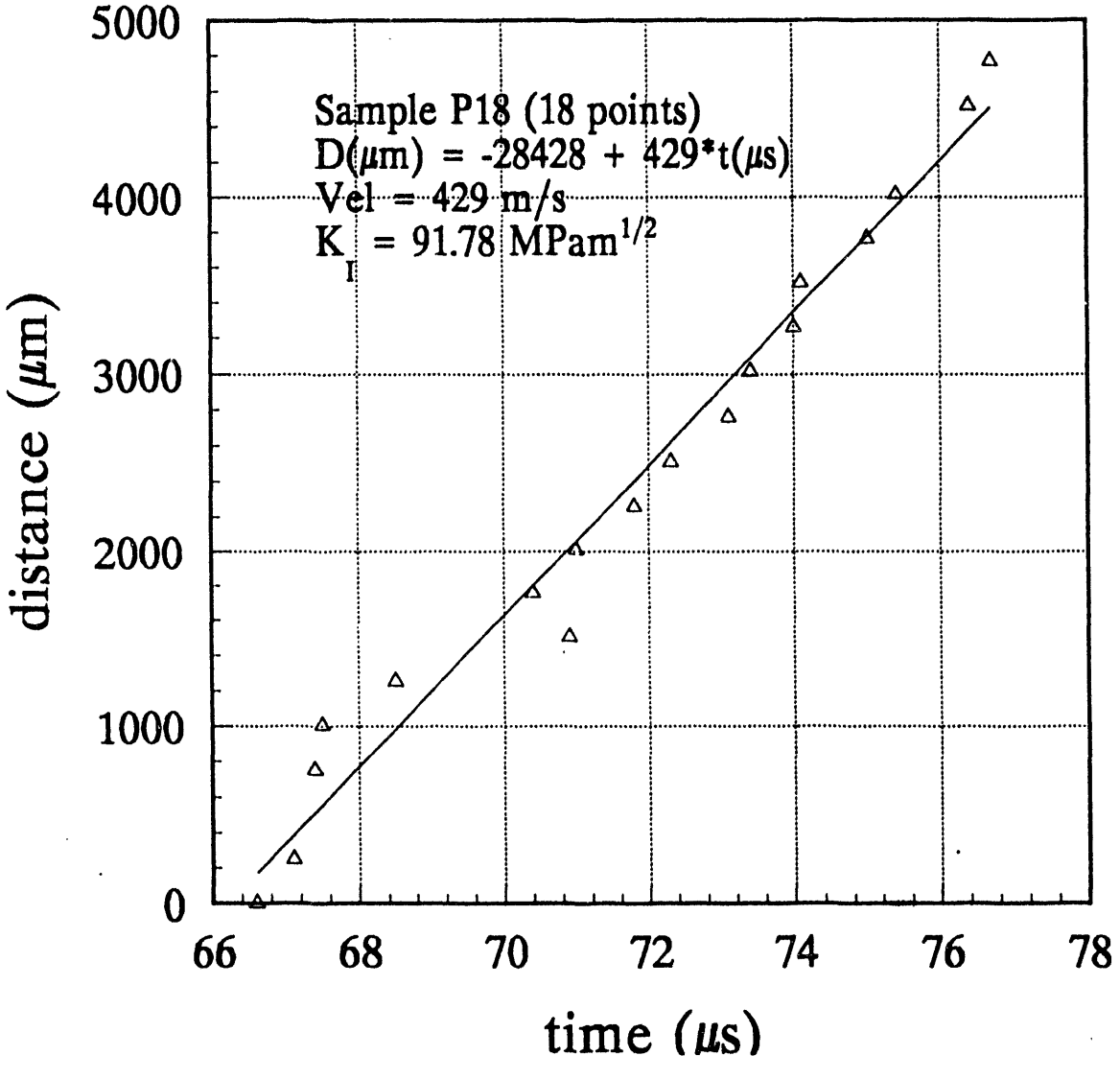
Sample P18 (18 points)
D(μm) = -28428 + 429*t(μs)
Vel = 429 m/s
K_I = 91.78 MPam^1/2
distance (μm)
time (μs)
0
1000
2000
3000
4000
5000
66
68
70
72
74
76
78

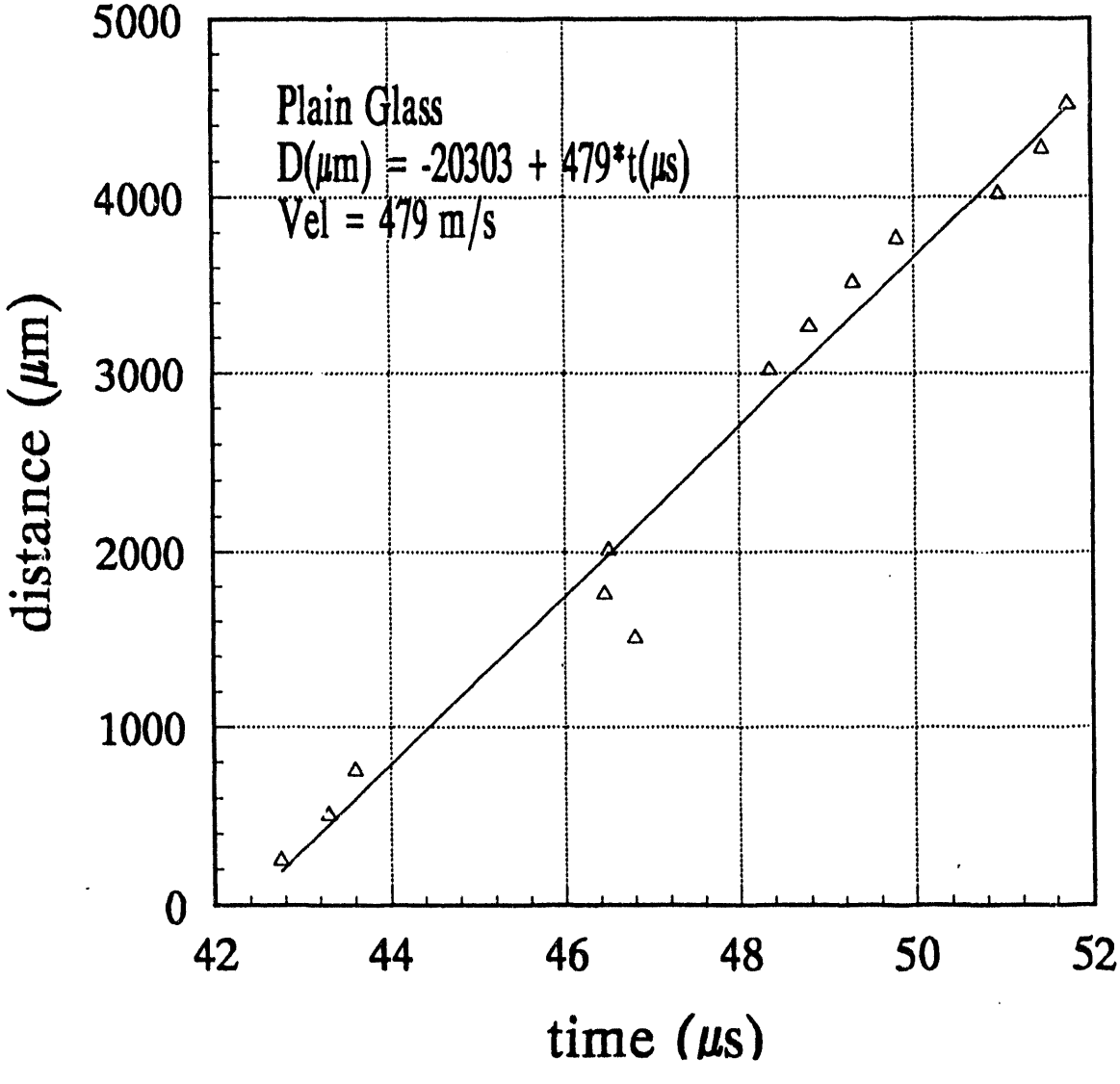
Plain Glass
D(μm) = -20303 + 479*t(μs)
Vel = 479 m/s
distance (μm)
time (μs)
0
1000
2000
3000
4000
5000
42
44
46
48
50
52

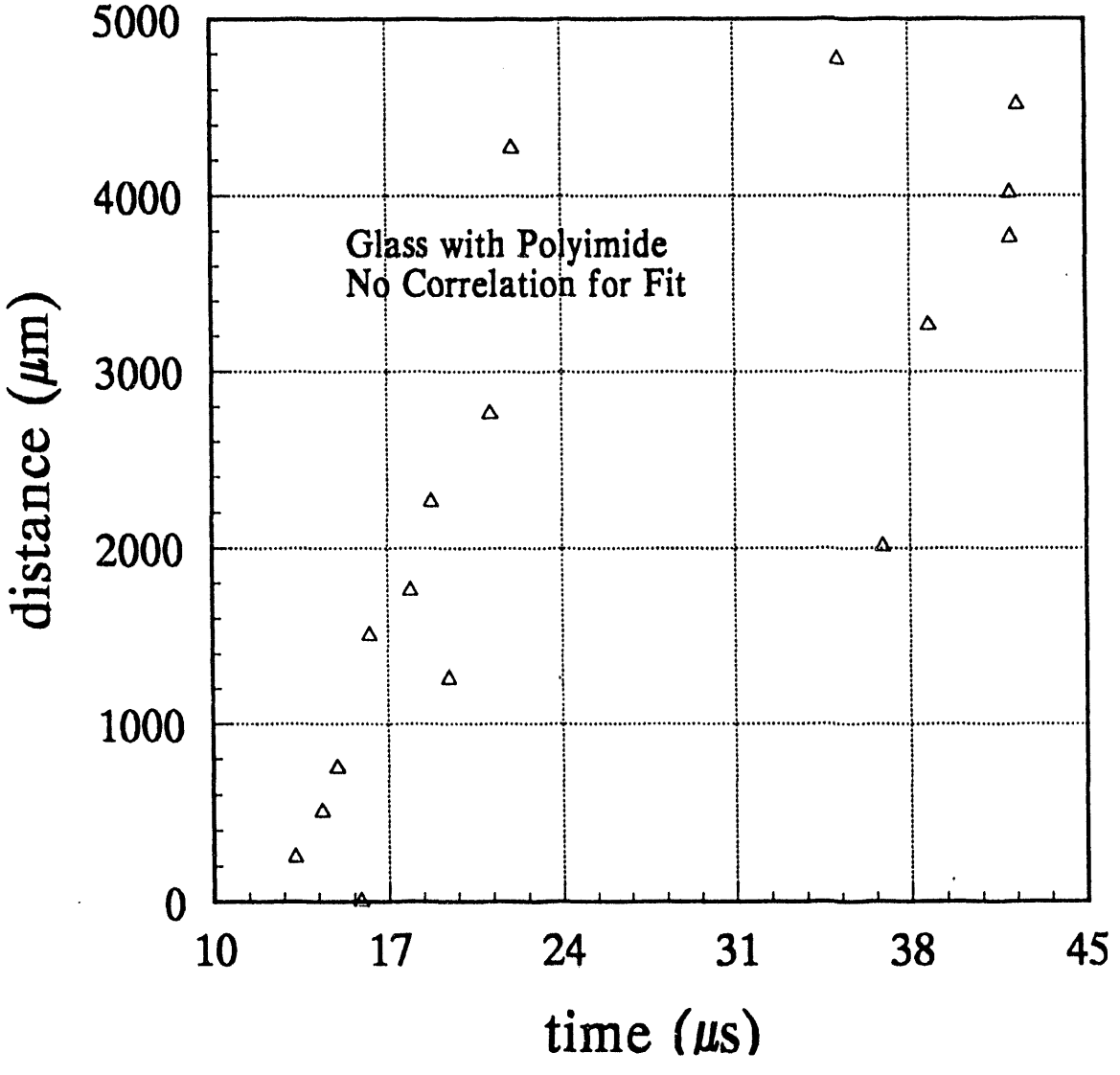
Glass with Polyimide
No Correlation for Fit
distance (μm)
time (μs)
5000
4000
3000
2000
1000
0
10
17
24
31
38
45

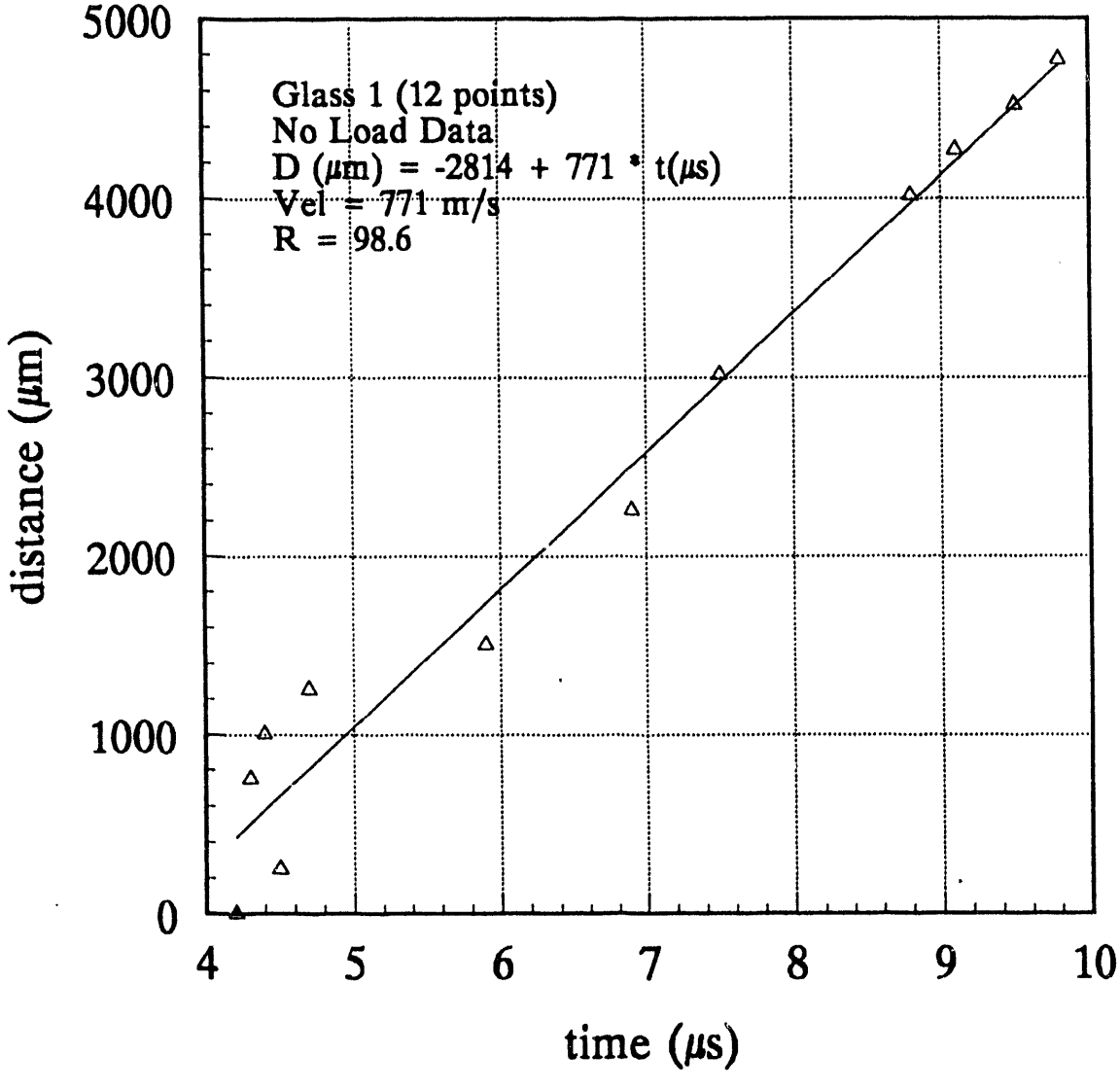
Glass 1 (12 points)
No Load Data
D (μm) = -2814 + 771 * t(μs)
Vel = 771 m/s
R = 98.6
5000
4000
3000
2000
1000
0
distance (μm)
4
5
6
7
8
9
10
time (μs)

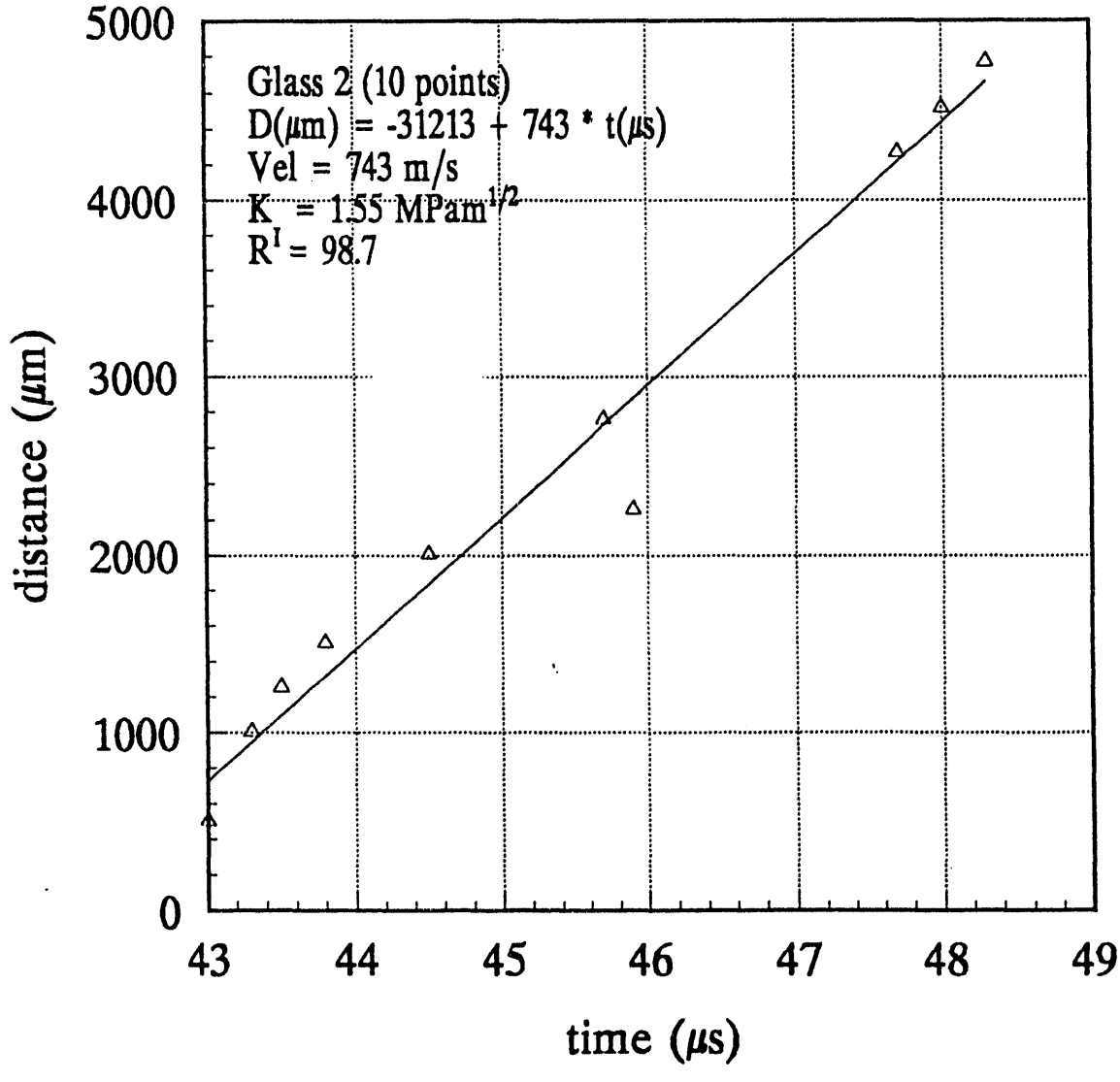
Glass 2 (10 points)
D(μm) = -31213 + 743 * t(μs)
Vel = 743 m/s
K = 1.55 MPam^1/2
R^I = 98.7
distance (μm)
time (μs)
0
1000
2000
3000
4000
5000
43
44
45
46
47
48
49

DATE
FILMED
5/18/94

END